VRIJE UNIVERSITEIT BRUSSEL

FACULTEIT VAN DE WETENSCHAPPEN

Contribution to the study of the Triple Gauge Boson Couplings in fully hadronic WW final states at LEP2

Ann Van Lysebetten

Januari 2001

Contribution to the study of the Triple Gauge Boson Couplings in fully hadronic WW final states at LEP2

PROEFSCHRIFT

ter verkrijging van de wettelijke graad
van doctor in de wetenschappen
aan de Vrije Universiteit Brussel,
in het openbaar te verdedigen op
vrijdag 19 januari 2001 te 16:00 uur

door

Ann Van Lysebetten

Promotiecommissie:

Promotor:	Dr. C. De Clercq, Vrije Universiteit Brussel
Voorzitter:	Prof. Dr. J. Van Craen, Vrije Universiteit Brussel
Secretaris:	Prof. Dr. R. Roosen, Vrije Universiteit Brussel
Overige leden:	Prof. Dr. J-M. Frere, Universite Libre de Bruxelles
	Prof. Dr. J. Lemonne, Vrije Universiteit Brussel
	Dr. R. Sekulin, Rutherford Appleton Laboratory
	Prof. Dr. A. Sevrin, Vrije Universiteit Brussel
	Prof. Dr. S. Tavernier, Vrije Universiteit Brussel
	Dr. J. Timmermans, Nikhef Amsterdam

Cover: The discovery of the W particle in the UA1 detector from the October - December 1982 run of the proton anti-proton collider, producing a high transverse energy electron (arrowed). This particle is produced back-to-back with “missing energy”, indicative of the emission of an invisible neutrino. (Photo CERN 69576)

“Wer nicht von dreitausend Jahren
sich weiss Rechenschaft zu geben,
bleib im Dunkeln unerfahren,
mag von Tag zu Tage leben”

Goethe - Westöstlicher Divan

Contents

List of Figures

List of Tables

Introduction

What is matter made of? What are the principles in nature which govern the universe we live in? Elementary particle physics investigates the microcosm and searches the fundamental constituents of matter and the manner in which these building blocks interact.
The Standard Model, based on gauge theories, gives a description of the unification of the strong, weak and electromagnetic interactions. This model still forms a solid basis of today's theoretical predictions. The electroweak part of this model was developed in the 1960's by Glashow, Salam and Weinberg and has been tested extensively in numerous experiments, but still no significant deviations have been found.
Powerful colliders at constantly higher energies need to be built in order to investigate matter on smaller and smaller scales. One of these colliders is the Large Electron Positron (LEP) collider, installed in a circular tunnel of 27 km circumference at CERN (Geneva). The collider became operational in 1989 and the four experiments (ALEPH, DELPHI, L3 and OPAL) installed on it studied the properties of the Z boson extensively for seven years. In a second phase, which started in 1996, the LEP collider was upgraded and beam energies from 80 to 104 GeV were attained. This LEP-2 project is dedicated to precision measurements of the W bosons, as well as to searches for new physics phenomena, to gain a deeper understanding of why the Standard Model works and what is the mechanism of electroweak symmetry breaking, and what might lie beyond it. At the beginning of this millennium LEP is running at its limit and many questions have been answered but even more stay unanswered.
The subject of this thesis is the study the Triple Gauge Boson Couplings (TGC) in W pair production with data taken with the DELPHI detector at centre-of-mass energies of 183 GeV and 189 GeV in 1997 and 1998. At these energies one is well above threshold for W pair production in e^+e^- annihilation and accurate limits can be set on the size of the couplings in the trilinear vertices $WW\gamma$ and WWZ. The existence of the trilinear vertices is a direct consequence of the Standard Model being non-Abelian. The mathematical meaning of a group not being Abelian is that its elements do not commute. In the electroweak model the practical consequence of this abstraction is that the W, Z and γ boson fields couple to themselves whereas the photon field in pure electromagnetic interactions does not. The observation of W pair production serves as a direct confirmation of the non-Abelian structure of electroweak interactions.
Each vertex has a set of corresponding parameters specifying the strength of the couplings. The parameters describing the vertices $WW\gamma$ and WWZ have given values in the Standard Model. The anomalous couplings, Δg_Z^1, $\alpha_{W\phi}$, α_W and $\alpha_{B\phi}$, studied in this thesis describe the deviation of the TGC parameters from their Standard Model values. The measurement of these couplings at LEP is important for two reasons. Firstly, it is the first time that these $WW\gamma$ and WWZ vertices are directly produced in e^+e^- reactions hence allowing to set direct limits on their values. Secondly, the measurement of these couplings provides a unique window on new physics as a

non-zero value for any of the TGC parameters gives an indication of physics beyond the Standard Model.

The aim of the present analysis is to determine the anomalous TGC parameters Δg_Z^1, $\alpha_{W\phi}$, α_W and $\alpha_{B\phi}$, and thereby the underlying structure of the $WW\gamma$ and WWZ vertices. We will use the fully hadronic WW events, as this represents a large data sample with its branching fraction of about 46%. The method used exploits the dependence of the couplings on the production angle of the W^- boson and on the total production cross section. The underlying statistical framework is based on the principle of the Extended Maximum Likelihood technique.

The lay-out of this thesis is as follows. Chapter 1 provides an introduction to the Standard Model with emphasis on the electroweak sector most directly relevant to this thesis. The Lagrangian describing the TGC vertices is presented and the TGC parameters which will be measured are defined. Finally the production of W^+W^- bosons in e^+e^- annihilation and the WW decay mechanisms are discussed in detail.

Chapter 2 provides the reader with the relevant background knowledge of the LEP accelerator and an overview of the DELPHI detector required for the analysis chapters that follow. The different sub-detectors, their composition and properties will be explained. The chapter concludes with a general guide to the trigger and data read-out system as well as the offline processing software.

In Chapter 3 we summarise the role of event simulation and give a short overview of the Monte Carlo generators used. We discuss the particle selection and data quality criteria which are used in this analysis. The LEP collider beam energy and the integrated luminosity collected for the data sets at 183 GeV and 189 GeV are then recalled. In a following section the jet clusterisation algorithm is explained and next we discuss the kinematic fitting algorithm. Finally, after having presented all ingredients, the hadronic WW event selection procedure is explained. The selection criteria are developed according to the specific topology of the fully hadronic WW events. To verify the selection procedure, all distributions obtained in data are compared with those expected from simulated events.

In Chapter 4 the analysis method for both centre-of-mass energies is presented and the likelihood method used is tested on statistical properties and accuracy. Every selected hadronic event has a four jet topology as we force all events into four jets. In the first sections of Chapter 4 we describe how the particular "difficulties" in the hadronic channel are overcome. These are the ignorance of which pair of jets belongs to which W, and the ambiguity on the charge of the W. Next the production angle of the W^- boson is reconstructed and its distribution studied for simulated signal and background events. The distributions obtained for simulated events are compared to the distribution for data events. In a following phase we make a full Monte Carlo study of the analysis method. The Extended Maximum Likelihood technique is tested at different levels of data reconstruction. At each level the fitted parameters and the errors obtained from the fit are studied using a large number of Monte Carlo experiments each equivalent to the data size. These verifications are made at both centre-of-mass energies separately. Only single parameter fits are done, varying one TGC parameter and leaving the others at their Standard Model values.

In the last chapter the analysis is performed to both data sets consisting of the hadronic WW events selected from the samples taken by DELPHI at $\sqrt{s}$ = 183 GeV and $\sqrt{s}$ = 189 GeV. Four single TGC parameter fits are made to Δg_Z^1, $\alpha_{W\phi}$, α_W and $\alpha_{B\phi}$. In each fit the three other parameters will be fixed at their Standard Model value. The systematic errors on the measurement of the TGC parameters are also evaluated in Chapter 5. Next we combine the results of the two data sets taking into account all uncertainties and provide a discussion of the obtained limits on the TGC parameters. In the last section we make a comparison with other TGC measurements and give a brief outlook of the future TGC measurements.

Introduction

Chapter 1

Theoretical introduction
The W boson in the Standard Model

1.1 Introduction

This chapter does not cover all details of the contemporary world of particle physics, but just gives an introduction to the theoretical principles which are underlying the work presented in this thesis. In the first few sections the most relevant components of the Standard Model are reviewed based on references [1, 2, 3, 4] and the reader is referred to these for further details. Afterwards the physics of the W boson is presented and a theoretical description of the triple gauge boson couplings is given with emphasis on the parts relevant for this thesis. In the last part this chapter concentrates on the reaction $e^+e^- \rightarrow W^+W^-$ and various aspects related to this process are described.

1.2 The Standard Model

Current understanding of the interactions between the fundamental building blocks of matter is based on the Standard Model [5] (SM). The electroweak part of this model, developed in the 1960's by Glashow [6], Salam [7] and Weinberg [8] (GSW model), explains the bulk of all experimental measurements on electromagnetic and weak phenomena. The theory, describing the unification of strong, weak and electromagnetic interactions, is a non-Abelian gauge theory. The juxtaposition of 3 symmetry groups $SU(3)_C \times SU(2)_I \times U(1)_Y$ builds up the symmetry group of the SM Lagrangian. The group $SU(3)_C$, couples to the "colour" quantum number C, describes the strong force or Quantum Chromo Dynamics (QCD). This subject is not discussed further in this thesis as it is not important to the W pair production process.
The group $SU(2)_I \times U(1)_Y$ describes the electroweak part of the theory, which will be presented in detail in the following sections. The group structure of the GSW model implies as a direct consequence the existence of weak neutral current (NC) interactions in addition to the electromagnetic ones and related to the already observed weak charged current (CC) interactions. These NC interactions were observed in 1972 by the Gargamelle bubble chamber experiment of neutrino scattering on nucleons [9] and hence gave the first validation of the Model. The Standard Model has the property that calculations of physically observable quantities can be made finite order by

Fermions			I_3	Y	Q
$\begin{pmatrix} \nu_\mathrm{e} \\ \mathrm{e} \end{pmatrix}_L$	$\begin{pmatrix} \nu_\mu \\ \mu \end{pmatrix}_L$	$\begin{pmatrix} \nu_\tau \\ \tau \end{pmatrix}_L$	$+1/2$ $-1/2$	-1	0 -1
e_R	μ_R	τ_R	0	-2	-1
$\begin{pmatrix} u \\ d \end{pmatrix}_L$	$\begin{pmatrix} c \\ s \end{pmatrix}_L$	$\begin{pmatrix} t \\ b \end{pmatrix}_L$	$+1/2$ $-1/2$	+1/3	$+2/3$ $-1/3$
u_R d_R	c_R s_R	t_R b_R	0 0	+4/3 -2/3	+2/3 -1/3

Table 1.1: *The fermions of the Standard Model.*

order (at the cost of reabsorbing potential infinities in the fundamental couplings and masses). Such a theory is said to be renormalisable. It can be shown that gauge theories are automatically renormalisable [10, 11, 12].
The group $SU(2)_I$ is analogous to the group of rotations for spin $\frac{1}{2}$ particles, familiar from quantum mechanics. Instead of angular momentum, the quantum numbers associated with it are called weak isospin $\vec{I}$ in the SM.
When acting with an element of the $U(1)_Y$ group on a state, it gets multiplied with a phase factor. The corresponding charges are conventionally noted $g'Y$, with Y the hypercharge. The usual choice of the symmetry breaking direction leads to the relation between the electric charge Q, known from experiment, the hypercharge and the third generator of the SU(2) group, I_3:

$$Q = I_3 + Y/2. \tag{1.1}$$

The fundamental constituents of matter are the three generations of spin $\frac{1}{2}$ fermions (quarks and leptons) and the integer spin bosons. Quarks and leptons participate in electroweak interactions, and quarks also interact strongly. One has to choose a representation of the symmetry group for fermions in order to define their transformations under the group. Left- and right-handed fermions occur in different representations in the SM. The left-handed electron (e), muon (μ) and tau (τ) leptons are grouped in a doublet representation of SU(2) together with their associated left-handed neutrinos (ν_e, ν_μ, ν_τ). Their right-handed parts are in singlets of SU(2). Introducing the right-handed neutrinos is optional in the Standard Model. The quarks occur in an analogous representation. Table 1.1 gives an overview of these fermion representations. All fundamental fermions of the Standard Model have been discovered. In 1989 the LEP experiments established that the number of generations of fundamental leptons is limited to three [13]. The last one to be discovered was the top quark found in 1995 by the D0 and CDF collaborations at the Tevatron [14, 15] with a mass as predicted by the LEP experiments on the basis of the Standard Model [16].
The interactions between fermions take place via the exchange of the gauge bosons. An overview

Vector Boson	Interaction	Spin	Mass
W^+	Electroweak	1	80.385 ± 0.022 GeV
Z^0		1	91.1871 ± 0.0021 GeV
W^-		1	80.385 ± 0.022 GeV
γ	Electroweak	1	0
g	QCD	1	0
graviton	Gravity	2	0

Table 1.2: *The intermediate vector bosons of the Standard Model. The mass values are extracted from reference [21].*

of these can be found in Table 1.2. The $W^\pm$ and Z bosons have been discovered in 1983 in $\mathrm{p\overline{p}}$ collisions by the experiments UA1 [17, 18] and UA2 [19, 20].

1.2.1 The electroweak theory

The electroweak theory describes in a unified way the electromagnetic and weak interactions of fermions. Making the fermion Lagrangian density L, describing the creation and annihilation of fermions, gauge invariant under $SU(2)_I \times U(1)_Y$ implies the introduction of additional gauge fields. Three weak isospin currents (one neutral and two charged) are introduced and they couple, with strength g, to a weak isospin triplet of intermediate massless vector bosons $\mathbf{W}_\mu$. The weak hypercharge current couples, with strength g', to an isosinglet of an intermediate neutral massless vector boson B_μ.
The charged sector of the SM consists of the fields W^1_μ and W^2_μ. To find the physical fields describing the $W^\pm$ bosons one takes the following combination:

$$W^\pm_\mu = \frac{1}{\sqrt{(2)}}(W^1_\mu \mp iW^2_\mu). \tag{1.2}$$

In the neutral sector we have the fields B_μ and W^3_μ. These can be identified with the physical photon and the Z boson as orthogonal linear combinations of the aforementioned fields

$$\begin{aligned} A_\mu &= \sin\theta_W W^3_\mu + \cos\theta_W B_\mu; \\ Z_\mu &= \cos\theta_W W^3_\mu - \sin\theta_W B_\mu; \end{aligned}$$

where θ_W is known as the Weinberg mixing angle and indicates the strength of mixing of the weak and electromagnetic interactions. This angle has to be measured experimentally and the current value [21] is:

$$\sin^2\theta_W = 0.23151 \pm 0.00017. \tag{1.3}$$

Identifying A_μ with a photon field which couples via the electric charge e of the electron, e can be expressed as

$$g'\cos\theta_W = g\sin\theta_W = e. \tag{1.4}$$

The fermions and gauge bosons in the theory presented above are massless. We know from experiment that this, except for the photon, is not the case. When imposing local gauge invariance one cannot add an explicit mass term to the Lagrangian for the gauge bosons. The principle of spontaneous symmetry-breaking, known from solid state physics, has been incorporated in the SM giving masses to the vector bosons Z^0, W^+ and W^- . As a by-product it also provides the different masses of the fermions. This principle goes under the name Brout-Englert-Higgs mechanism [22, 23, 24, 25, 26]. Four real scalar fields ϕ_i are introduced associated with a doublet Φ of weak isospin of complex scalar fields:

$$\Phi = \begin{pmatrix} \phi_+ \\ \phi_0 \end{pmatrix} \quad \begin{matrix} \phi_+ = \frac{\phi_1 + i\phi_2}{\sqrt{2}} \\ \phi_0 = \frac{\phi_3 + i\phi_4}{\sqrt{2}} \end{matrix} \quad , \tag{1.5}$$

with a potential taken to be of the form

$$V(\Phi) = \mu^2 \Phi^\dagger \Phi + \lambda (\Phi^\dagger \Phi)^2 \quad \text{with } \lambda > 0. \tag{1.6}$$

The parameters of this potential are such that the Higgs field has non-zero solutions at the minimum. With $\mu^2 < 0$ and $\lambda > 0$ these conditions are fulfilled and the potential has an infinite number of non-zero solutions (ground states) given by the norm of the field

$$\Phi^\dagger \Phi = -\frac{\mu^2}{2\lambda} \equiv v^2/2, \tag{1.7}$$

where v is the vacuum expectation value, representing the energy scale where electroweak symmetry breaking takes place. The ground state or vacuum is only invariant under $U(1)$ transformations, unlike the Lagrangian which is invariant under SU(2)×U(1).
If we take a particular solution of the scalar field at the minimum, the Higgs field in the neighbourhood of this minimum can be chosen as follows:

$$\Phi(x) = e^{i\vec{\sigma}\cdot\xi(\vec{x})} \frac{1}{\sqrt{2}} \begin{pmatrix} 0 \\ v + h(x) \end{pmatrix}, \tag{1.8}$$

where $\vec{\sigma}$ represent the three Pauli matrices, generators of the group SU(2). $\vec{\xi}$ and $h(x)$ are the four degrees of freedom of the field Φ. The three fields $\vec{\xi}$ are the Goldstone bosons, of zero mass. By fixing a gauge, the three degrees of freedom of the three Goldstone bosons are used to give a mass to the three vector bosons. One massive scalar is left: the Higgs boson H. The masses of the bosons are then given by

$$M_W = gv/2, \tag{1.9}$$

$$M_Z = gv/2 \cos\theta_W, \tag{1.10}$$

$$M_H = \sqrt{2\lambda v^2}; \tag{1.11}$$

and the Weinberg mixing angle θ_W is defined as

$$c_W \equiv \cos\theta_W = \frac{M_W}{M_Z}, \tag{1.12}$$

$$s_W^2 \equiv \sin^2\theta_W = 1 - \frac{M_W^2}{M_Z^2}. \tag{1.13}$$

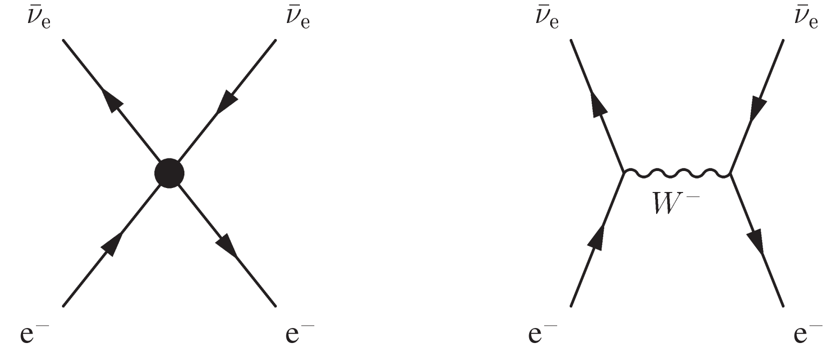

Figure 1.1: *Electron neutrino interactions as a contact interaction (a, left), with the addition of an intermediate vector boson (b, right).*

The fermions couple with the scalar Higgs field Φ by a Yukawa coupling [27]. If g_f is the Yukawa coupling constant, the fermion mass is given by

$$m_f = \frac{g_f v}{\sqrt{2}}. \tag{1.14}$$

1.3 The *W* boson

The first attempt at a theory describing weak interactions was made by Fermi in 1934 [28]. The beta-decay process was treated as a contact interaction (see Figure 1.1(a)) and the cross-section for neutrino electron scattering was predicted:

$$\sigma_{tot}(\mathrm{e}\overline{\nu}_\mathrm{e} \to \mathrm{e}\overline{\nu}_\mathrm{e}) = \frac{G_F^2 s}{\pi}, \tag{1.15}$$

with G_F the Fermi coupling constant. This Fermi theory, incorporating the V-A coupling form, is not renormalisable. Furthermore the cross-section is clearly divergent and as there is no propagator in the matrix element one can clearly see that the Fermi coupling constant G_F is not dimensionless. So it was soon realised that the Fermi model was a low energy effective theory, and one needed an intermediate weakly interacting boson to overcome these shortcomings, as proposed by Yukawa [27]. With the Standard Model the firm prediction of the massive W boson appeared. For $s \ll M_W^2$ the relation between the coupling constants of the two theories is

$$\frac{G_F}{\sqrt{2}} = \frac{g_W^2}{8M_W^2}. \tag{1.16}$$

Indeed the W boson needed to be massive in order to explain the short-range nature of the interaction and appear in two charge states to reproduce the observed properties of the V-A Lagrangian. The W coupling is a combination of Vector and Axial-vector form (V-A) which has as a consequence that this boson only couples to the left-handed chirality states of the fermions. From the SM one can obtain the Feynman rules [1], the rules for the three point vertex in Figure 1.2 are given in Table 1.3. The CKM or Cabibbo-Kobayashi-Maskawa matrix used in this table is a 3×3 - matrix descibing the unitary transformation of the quark mass eigenstates mixing. The matrix γ_5 used in the vertexfactors can be defined as

$$\gamma_5 \equiv i\gamma_0\gamma_1\gamma_2\gamma_3,$$

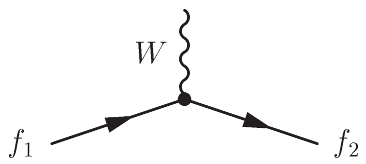

Figure 1.2: *The Feynman graph for the coupling of the W boson to a fermion pair.*

f_1	f_2	Vertexfactor
ν_l	l^-	$-\frac{ig_W}{\sqrt{2}}\gamma_\mu\frac{1-\gamma_5}{2}$
q_1	q_2	$-\frac{ig_W}{\sqrt{2}}V_{q_1q_2}\gamma_\mu\frac{1-\gamma_5}{2}$

Table 1.3: *The Feynman rules for fermion couplings to the W boson (see Figure 1.2), where g_W is the weak coupling constant, and V is the CKM matrix.*

with γ_i the Dirac γ-matrices.
The W boson is a short lived particle as its width is about 2 GeV. The branching ratios of the W boson are given in Table 1.4. The existence of the W boson was confirmed in 1983 by the UA1 [17] and UA2 [19] collaborations. The W boson properties have been and still are studied by CDF [29, 30, 31] and D0 [32, 33, 34] in $\mathrm{p\overline{p}}$ interactions at the Tevatron and more recently by the 4 LEP experiments, ALEPH [35, 36, 37], DELPHI [38, 39, 40], L3 [41, 42, 43] and OPAL [44, 45, 46].

Process	BR(%)
$W \to \mathrm{e}\nu_\mathrm{e}$	10.83
$W \to \mu\nu_\mu$	10.83
$W \to \tau\nu_\tau$	10.82
$W \to$ lep.	32.49

Process	BR(%)
$W \to$ ud	32.11
$W \to$ us	1.65
$W \to$ ub	10^{-4}
$W \to$ cd	1.65
$W \to$ cs	32.05
$W \to$ cb	0.05
$W \to$ had.	67.51

Table 1.4: *The Standard Model branching ratios [1] of the possible decays of the W boson at LEP-2. The notation in the table is generic, e.g. $W \to ud$ means $W^+ \to u\bar{d}$ and $W^- \to \bar{u}d$.*

1.4 Triple Gauge Boson Couplings (TGC)

The electroweak theory being non-Abelian has as the crucial consequence that triple and quartic[1] gauge boson couplings [48] exist. The self-couplings of the W, Z and γ, present in the Standard

[1] These couplings will not be discussed in this thesis and contributions to TGCs will be ignored as they are tested with low sensitivity at LEP-2 [47].

Model, are written in the following way in the electroweak Lagrangian:

$$\begin{aligned}\mathcal{L}_{SM} &= -ig_{WW\gamma}[g_\gamma^1 A_\mu(W^-_{\mu\nu}W^{+\nu} - W^+_{\mu\nu}W^{-\nu}) + \kappa_\gamma F^{\mu\nu}W^+_\mu W^-_\nu] \\ &\quad -ig_{WWZ}[g_Z^1 Z_\mu(W^-_{\mu\nu}W^{+\nu} - W^+_{\mu\nu}W^{-\nu}) + \kappa_Z Z^{\mu\nu}W^+_\mu W^-_\nu], \end{aligned} \tag{1.17}$$

where the field-strength tensors $F_{\mu\nu}$, $Z_{\mu\nu}$ and $W^\pm_{\mu\nu}$ are defined from the corresponding vector fields $V_\mu(\equiv A_\mu, Z_\mu, W^\pm_\mu$ respectively) as $(\partial_\mu V_\nu - \partial_\nu V_\mu)$. The overall couplings are defined as $g_{WW\gamma} = e$ and $g_{WWZ} = e\cot\theta_W$. Within the SM, at tree level, these couplings called Triple Gauge Boson Couplings (TGCs), are given by

$$g_Z^1 = g_\gamma^1 = \kappa_Z = \kappa_\gamma = 1.$$

The form of the gauge bosons interaction is entirely predicted by the SM, but the question is if there still is some room for new physics beyond the SM? If we ask ourselves how two W bosons and a photon or Z boson may interact, we can write down all possible interaction terms which describe the process WWV ($V \equiv \gamma$ or Z) in an effective Lagrangian, obeying certain rules such as Lorentz invariance, as an extension to the SM:

$$\begin{aligned} i\mathcal{L}^{WWV}_{eff} &= g_{WWV}[g_V^1 V^\mu(W^-_{\mu\nu}W^{+\nu} - W^+_{\mu\nu}W^{-\nu}) + \kappa_V W^+_\mu W^-_\nu V^{\mu\nu} + \\ &\quad \frac{\lambda_V}{M_W^2}V^{\mu\nu}W^{+\rho}_\nu W^-_{\rho\mu} \\ &\quad +ig_5^V\epsilon_{\mu\nu\rho\sigma}((\partial^\rho W^{-\mu})W^{+\nu} - W^{-\mu}(\partial^\rho W^{+\nu}))V^\sigma \\ &\quad +ig_4^V W^-_\mu W^+_\nu(\partial^\mu V^\nu + \partial^\nu V^\mu) - \frac{\tilde{\kappa}_V}{2}W^-_\mu W^+_\nu \epsilon^{\mu\nu\rho\sigma}V_{\rho\sigma} \\ &\quad -\frac{\tilde{\lambda}_V}{2M_W^2}W^-_{\rho\mu}W^{+\mu}_\nu \epsilon^{\nu\rho\alpha\beta}V_{\alpha\beta}]. \end{aligned} \tag{1.18}$$

The antisymmetric tensor $\epsilon_{\mu\nu\rho\sigma}$ has the value $+1$ (-1) if the indices are an even (odd) number of permutations of 0,1,2,3 and is zero if two or more indices are equal. Within the SM, at tree level, the couplings $g_Z^1 = g_\gamma^1 = \kappa_Z = \kappa_\gamma = 1$, with all other couplings in Equation 1.18 vanishing. In this way the Lagrangian $\mathcal{L}_{SM}$ from Equation 1.17 is recovered.

From a phenomenological point of view the couplings related to the $WW\gamma$ vertex correspond to the lowest terms of a multi-pole expansion of the $W\gamma$ interaction with

$$\begin{aligned} Q_W &= eg_\gamma^1, \\ \mu_W &= \frac{e}{2M_W}(g_\gamma^1 + \kappa_\gamma + \lambda_\gamma), \\ q_W &= -\frac{e}{M_W^2}(\kappa_\gamma - \lambda_\gamma), \end{aligned}$$

where Q_W is the the electric charge, μ_W the magnetic dipole momentum and q_W the electric quadrupole momentum of the W^+ boson.

The parametrisation in the Lagrangian (Equation 1.18) involves 14 TGC parameters; ie. 7 independent operators for each vertex. Three parameters (g_V^1, κ_V and λ_V) conserve C and P individually[2], one (g_5^V) violates C and P but conserves CP, and the remaining (g_4^V, $\tilde{\kappa}_V$ and $\tilde{\lambda}_V$) couplings

[2] C and P represent transformations of charge conjugation and spatial inversion or parity respectively.

parametrise a possible CP-violation in the bosonic sector.
On rather general grounds [49] C, P and CP-violating couplings can be ignored since they are not likely to produce observable effects at LEP-2; as a consequence only C and P conserving couplings will be considered in this thesis. Furthermore no deviations of the coupling strength Δg_γ^1, given by the electric charge, are expected[3]. This leaves us with five coupling parameters. We would like to study deviations from the SM, so the set used is the following:

$$\begin{aligned} \Delta g_Z^1 \equiv & \quad g_Z^1 - 1, \\ \Delta \kappa_\gamma \equiv & \quad \kappa_\gamma - 1, \\ \Delta \kappa_Z \equiv & \quad \kappa_Z - 1, \\ \lambda_\gamma, \lambda_Z . & \end{aligned}$$

In the SM all these parameters take a value of zero. The statistical precision at LEP-2 is limited and it is not possible to perform a multidimensional fit to retrieve the parameter information with a reasonable accuracy. Hence it is desirable to reduce even further the number of parameters on the basis of theoretical arguments.
Where do we have to look for new physics? Let there be some new physics scale at high energy called Λ. The terms contributing to this new physics enter in the Lagrangian of Equation 1.18 suppressed by factors like $1/\Lambda^{N-4}$, with $N \geq 4$ the dimension of the operators. Since lower dimension operators are more likely to produce observable effects, we only include dimension four and six operators. Furthermore the SM has been extensively tested and $SU(2) \times U(1)$ must be a good symmetry at the weak scale - hence a classification of extra terms in terms of $SU(2) \times U(1)$ invariance is useful. So if we imply this invariance and we consider only couplings which are not excluded by LEP-1 measurements ("blind directions" [49, 50]), we further reduce the parameter set. The three remaining operators which do not affect the gauge boson coupling at tree level but give rise to deviations in the C and P conserving TGC parameters are denoted as $\alpha_{W\phi}$, $\alpha_{B\phi}$ and α_W, for which results obtained earlier by the four LEP collaborations were quoted. The effective Lagrangian of Equation 1.18 becomes

$$\mathcal{L}_{d=6}^{TGC} = ig' \frac{\alpha_{B\phi}}{M_W^2} (D_\mu \Phi)^\dagger B^{\mu\nu} (D_\nu \Phi) + ig \frac{\alpha_{W\phi}}{M_W^2} (D_\mu \Phi)^\dagger \vec{\tau} . \hat{\vec{W}}^{\mu\nu} (D_\nu \Phi) + g \frac{\alpha_W}{6M_W^2} \hat{\vec{W}}^{\mu}{}_{\nu} . (\hat{\vec{W}}^{\nu}{}_{\rho} \times \hat{\vec{W}}^{\rho}{}_{\mu}),$$

where $D_\mu \Phi$ are the covariant derivatives of the Higgs field, $\hat{W}_{\mu\nu} = W_{\mu\nu} - gW_\mu \times W_\nu$ and $B_{\mu\nu}$ are the non-Abelian field strength tensors of the $SU(2)$ and $U(1)$ gauge fields respectively and g and g' the $SU(2)$ and $U(1)$ couplings respectively. The usual choice for the Higgs breaking direction yields non vanishing anomalous TGCs in Equation 1.18; (Δg_Z^1, $\Delta\kappa_\gamma$, λ_γ) the parameter set in which the obtained results will be quoted, with the following constraints coming from SU(2) $\times$ U(1):

$$\begin{aligned} \Delta \kappa_Z = & \quad \Delta g_Z^1 - \Delta \kappa_\gamma \tan^2 \theta_W ; \\ \lambda_Z = & \quad \lambda_\gamma . \end{aligned}$$

[3]Note however that, without affecting the electric charge of the W (which is forbidden by charge conservation) the presence of a heavy Z' could be reinterpreted at low energy as modifications of the effective Z and γ couplings. In this case both the effective g_γ and g_Z can depart from their value.

The relationship between the α parameter set and the set used in this thesis is the following:

$$\begin{aligned} \Delta g_Z^1 &= \alpha_{W\Phi}/c_W^2, \\ \Delta\kappa_\gamma &= \alpha_{W\Phi} + \alpha_{B\Phi}, \\ \lambda_\gamma &= \alpha_W. \end{aligned} \tag{1.19}$$

For completeness, an alternative naming convention, used in [51, 52, 53], has been introduced here:

$$\begin{aligned} \delta_Z &\equiv \cot\theta_W \Delta g_Z^1, \\ x_\gamma &\equiv \Delta\kappa_\gamma, \\ x_Z &\equiv \Delta\kappa_Z(\cot\theta_W + \cot\theta_W \Delta g_Z^1), \\ y_\gamma &\equiv \lambda_\gamma, \\ y_Z &\equiv \lambda_Z \cot\theta_W. \end{aligned}$$

1.4.1 Limits of the Standard Model

The Standard Model, as we have seen it in Section 1.2, has been extensively verified in a wide range of experiments, but so far no significant deviations from its predictions have been observed. Even though this is a tremendous success, it does not prove that this Model is the final and complete one [54]. On the contrary, the Standard Model still leaves some important issues unexplained:

- Why the considerable number of free parameters?
- What does it take to include gravity?
- Why are the particle masses not closer to the Planck mass ($\cong 10^{19}$ GeV, mass hierarchy problem)?
- Why are there three generations of particles?

So one can consider that the Standard Model, like in its time the Fermi theory, is an effective theory with a strong predictive power at currently accessible energies and that at higher energies this predictive power is lost. To accommodate some of these questions, numerous theories "beyond the Standard Model" exist. Amongst them there is supersymmetry, a symmetry linking bosons to fermions, at one end and technicolour or compositeness, assuming the Higgs to be an effective massive composite scalar, at the other end. The theory of compositeness explains the number of generations of fermions. But as the technicolour model predictions show large discrepancies with data, this model seems to be excluded. Supersymmetry brings a cure for the hierarchy problem, unifies the weak, strong and electromagnetic forces at $\sim 10^{16}$ GeV and preserves the predictive power of the Standard Model at present energies. It is partly for these reasons that supersymmetry is very popular in theoretical and experimental circles although so far no experimental proof has been found.

These new theories could lead to effects which are directly observable such as production of new particles, or to virtual effects. The latter induce deviations of measured physical quantities from

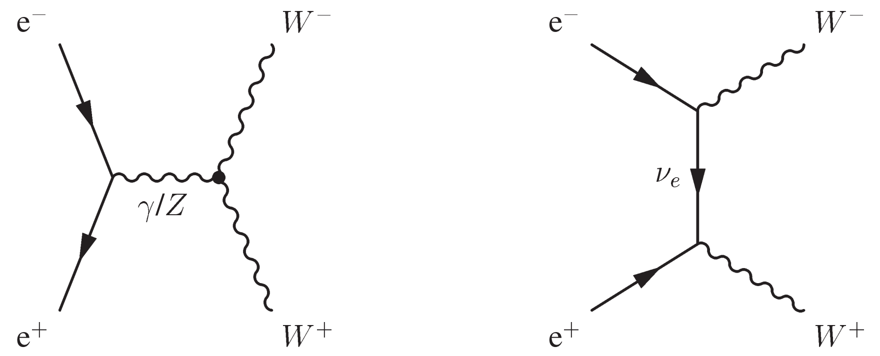

Figure 1.3: *Feynman diagrams for the process $e^+e^- \to W^+ W^-$. The diagram on the left shows the s channel of the process (with the photon or Z boson exchange), the diagram on the right shows the conversion in the t channel via neutrino exchange.*

their SM predictions. For instance one could introduce deviations in g_{WWZ} alone by assuming a new heavy sector boson Z' with strong self-couplings by a local $SU(2)_V$ gauge symmetry [55, 56]. The supersymmetric contributions to the TGC parameters have been calculated [57] but they seem to be negligible even in the most optimal configuration of the supersymmetric parameters.
Despite the early enthusiastic expectations most of the effects should be small at LEP-2 due to gauge invariance or unitarity requirements. They are nevertheless a unique window to new physics phenomena.
The reduction in the number of free TGC parameters, as it has been done in Section 1.4, serves the purpose of making tests on the SM. These reductions cannot substitute for a general fit in the case where deviations are observed. In that case a multi-parameter fit or a model-independent analysis has to be performed in order to determine and understand any new physical behaviour.

1.5 W pair production in e^+e^- annihilation

Triple Gauge Boson Couplings can be directly probed via W pair production at e^+e^- colliders. This production proceeds at tree level via the three Feynman graphs given in Figure 1.3. In the following sections the W pair production will be discussed at different levels of theoretical accuracy. In Section 1.5.1 both W's are considered on mass-shell and we limit ourselves to the three diagrams in the Born approximation of Figure 1.3. These processes are also called CC03 (charged current interaction, 3 diagrams). A fourth diagram, with the exchange of a Higgs particle, is not relevant at LEP-2 energies as this diagram is highly suppressed. The coupling of the Higgs boson is proportional to mass hence this diagram is neglected in the discussion presented below. However to avoid unitarity problems at very high energies in a full calculation this diagram must be included.
In Section 1.5.2 the W is no longer considered as a stable particle and the differential cross-sections are presented in the approximation of narrow width ($\Gamma_W \sim 0$). In the following section (1.5.3) the full four-fermion process is treated and the width of the W is introduced. In the last two sections (1.5.4 and 1.5.5) radiative corrections to the W pair production process and interconnection phenomena in the fully hadronic final state are discussed.

1.5.1 Tree level production of stable W bosons

Let σ, $\overline{\sigma}$, λ and $\overline{\lambda}$ be the helicity states of e^+, e^-, W^+ and W^- respectively for the process

$$e^+(p_1,\sigma) + e^-(p_2,\overline{\sigma}) \to W^+(p_3,\lambda) + W^-(p_4,\overline{\lambda}). \tag{1.20}$$

Starting from the electroweak Lagrangian and the expressions for the couplings from the vector bosons to the fermions, the following results can be obtained:

- $\sigma = -\overline{\sigma} = \pm\frac{1}{2}$;
- right-handed electrons ($\sigma = +\frac{1}{2}$) do not contribute to the t-channel with neutrino exchange, so their interaction is entirely dominated by γ and Z exchange. The interaction of the left-handed electrons, on the contrary, is entirely dominated by neutrino exchange.

In general a massive spin-1 boson has three polarisation states. This means that the helicity states of the W boson $\lambda = -\overline{\lambda}$ can be $\pm$ 1 and 0. The indices T and L refer to the transverse ($W^\pm$ helicity $\pm$ 1) and longitudinal ($W^\pm$ helicity 0) polarisation states respectively.
The kinematics of the process is defined in Figure 1.4. We choose the scattering angle Θ between the W^- and the e^-, so in the centre-of-mass (CM) system of the e^+e^- pair, also referred to as laboratory (LAB) system, the momenta read (with units c = 1 and the x,z plane taken as the scattering plane)

$$\begin{aligned} p_1^\mu = E(1,0,0,-1) \quad &, \quad p_2^\mu = E(1,0,0,1), \\ p_3^\mu = E(1,-\beta\sin\Theta,0,-\beta\cos\Theta) \quad &, \quad p_4^\mu = E(1,\beta\sin\Theta,0,\beta\cos\Theta), \end{aligned}$$

with $E = \frac{\sqrt{s}}{2}$ the beam energy and $\beta \equiv \sqrt{1-(\frac{2M_W}{\sqrt{s}})^2}$ the velocity of the W boson. The Bjørken-Drell metric is used with $g_{\mu\nu} = \mathrm{diag}(+1,-1,-1,-1)$.

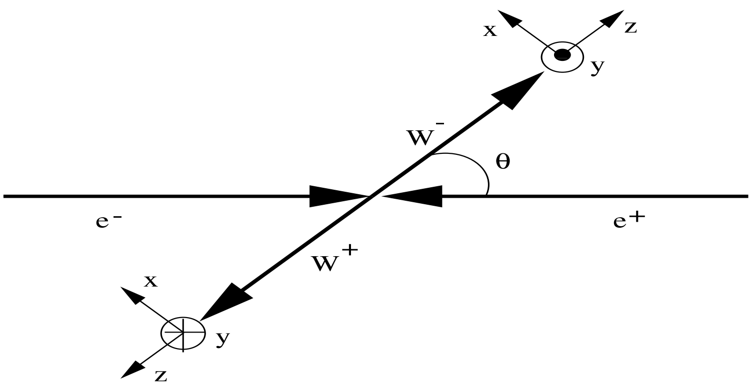

Figure 1.4: *Definition of the coordinate system used in the cross-section for the reaction $e^+e^- \to W^+W^- \to f_1\overline{f_2}f_3\overline{f_4}$. The production angle Θ is defined as the angle between the incoming electron and the outgoing W^-. The set of decay angles from each W decay is defined in the rest frame of the decaying $W^-(W^+)$ as θ and ϕ of the (anti) down type fermion. In total five angular variables are used to describe the process.*

The matrix element for on-shell W^+W^- production at LEP at the Born level can be expressed as [51, 58]

$$\mathcal{M} = \sqrt{2}e^2[\tilde{\mathcal{M}}_\gamma + \tilde{\mathcal{M}}_Z + \tilde{\mathcal{M}}_\nu(\Theta)]\Delta\sigma(-1)^{\overline{\lambda}} d^{J_0}_{\Delta\sigma,\Delta\lambda}(\Theta) \tag{1.21}$$

in terms of reduced amplitudes $\tilde{\mathcal{M}}$ by splitting off the leading angular dependence in terms of the d-functions [59] d^{J_0} where $J_0 \equiv max(|\Delta\sigma|, \Delta\lambda)$ denotes the minimum angular momentum of the system. The reduced amplitudes associated with γ, Z and ν exchange are written in the most general case of TGCs (defined in the Lagrangian of Equation 1.18) as follows:

$$\begin{aligned} \tilde{\mathcal{M}}_\gamma &= -\beta\delta_{|\Delta\sigma|,1} A^\gamma_{\lambda\overline{\lambda}}, \\ \tilde{\mathcal{M}}_Z &= \beta[\delta_{|\Delta\sigma|,1} - \tfrac{1}{2\sin^2\theta_W}\delta_{\Delta\sigma,-1}]\tfrac{s}{s-M_Z^2} A^Z_{\lambda\overline{\lambda}}, \\ \tilde{\mathcal{M}}_\nu &= \tfrac{1}{2\beta\sin^2\theta_W}\delta_{\Delta\sigma,-1}[B^\nu_{\lambda\overline{\lambda}} - \tfrac{1}{1+\beta^2-2\beta\cos\Theta} C^\nu_{\lambda\overline{\lambda}}], \end{aligned} \tag{1.22}$$

where $\Delta\sigma = \sigma - \overline{\sigma}$, $\Delta\lambda = \lambda - \overline{\lambda}$, $\delta_{i,j}$ represents the Kronecker delta function and the terms A, B, C and d are given in Table 1.5. We can consider two cases: when the W bosons are produced

$\Delta\lambda$	$(\lambda\overline{\lambda})$	$A^V_{\lambda\overline{\lambda}}$	$B^\nu_{\lambda\overline{\lambda}}$	$C^\nu_{\lambda\overline{\lambda}}$	$d^{J_0}_{\sigma,\lambda-\overline{\lambda}}$
± 2	(+ −),(− +)	0	0	$2\sqrt{2}\beta$	$-\lambda\sin\Theta\frac{(1-\lambda\cos\Theta)}{2\sqrt{2}}$
+1	(+ 0),(0 −)	$\gamma(g_V^1 + \kappa_V + \lambda_V)$	2γ	$2(1+\beta)/\gamma$	$\frac{(1+\sigma\cos\Theta)}{2}$
−1	(0 +),(− 0)	$\gamma(g_V^1 + \kappa_V + \lambda_V)$	2γ	$2(1-\beta)/\gamma$	$\frac{(1-\sigma\cos\Theta)}{2}$
0	(+ +),(− −)	$g_V^1 + 2\gamma^2\lambda_V$	1	$1/\gamma^2$	$\frac{-\sigma\sin\Theta}{\sqrt{2}}$
0	(00)	$g_V^1+2\gamma^2\kappa_V$	$2\gamma^2$	$2/\gamma^2$	$\frac{-\sigma\sin\Theta}{2}$

Table 1.5: *Coefficients for the e$^+$e$^-$ $\rightarrow W^+W^-$ matrix element. The γ used in the coefficients is $(1-\beta^2)^{-1/2}$, while the superscript V label represents a photon or Z boson.*

at threshold and when they are produced at high energies.

- At threshold $\beta \rightarrow 0$, the W pair is produced at rest and has no angular momentum. The total spin J_0 of the system must be 0, 1 or 2. The case where the total spin $J_0 = 0$ is prevented by conservation of electron chirality, because $\Delta\sigma$ is either 1 or -1. CP invariance eliminates the case where $J_0 = 1$. Only the helicity amplitudes given by the Clebsch-Gordan coefficients corresponding to $J_0 = 2$ remain, hence only the ν exchange diagram contributes to the final state at threshold.
  The terms $\tilde{\mathcal{M}}_\gamma$ and $\tilde{\mathcal{M}}_Z$ in Equation 1.22 are proportional to β hence the t-channel neutrino exchange will dominate the W^+W^- production. Since the phase space factor introduces a further β dependence the t-channel has a β dependence as the s-channel varies as β^3. This implies that the γ and Z exchange play nearly no role. As a consequence the triple gauge boson couplings cannot be studied with enough sensitivity at production threshold.

- at high energies ($\sqrt{s} \gg M_W$) $\gamma \rightarrow \infty$ and $\beta \rightarrow 1$. Some terms in Table 1.5 go to infinity, but the total cross-section is not divergent because of cancellations in the Standard Model (g_V^1 = κ_V = 1 and λ_V = 0). The reduced amplitude $\tilde{\mathcal{M}}_Z$ consists of two terms. The first one conserves parity and is called the "electromagnetic" component, which is cancelled by $\tilde{\mathcal{M}}_\gamma$

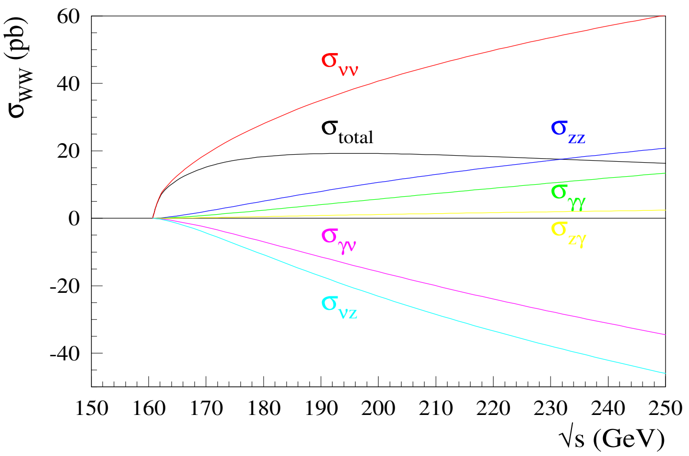

Figure 1.5: *The $e^+e^- \to W^+W^-$ cross-section in Born level approximation, the six individual contributions to the total are shown. These terms arise, when squaring the matrix elements, from the interference of the three component diagrams.*

as $A^Z_{\lambda\overline{\lambda}} = A^\gamma_{\lambda\overline{\lambda}}$. In the same way the second or "weak" term in $\tilde{\mathcal{M}}_Z$ is cancelled by the first term in $\tilde{\mathcal{M}}_\nu$ because at high energies $A^Z_{\lambda\overline{\lambda}} = B^\nu_{\lambda\overline{\lambda}}$. The divergences in $C^\nu_{\lambda\overline{\lambda}}$ are all suppressed by a factor γ in its denominator.

All contributions to the total cross-section are shown in Figure 1.5. We see that the purely t-channel contribution $\sigma_{\nu\nu}$ grows quickly although the total cross-section rapidly reaches its peak and then as a consequence of the gauge cancellations in the SM has a well behaved nature at high energies. For general Triple Gauge Boson Couplings the cancellations described above no longer occur, of course form factors should provide the necessary damping in this case. Departures from the SM predictions have the common features of destroying the gauge cancellations which ensure the decrease with energy of the total cross-section (especially LL and LT final states), and of modifying the angular distributions especially in the backward region, where the neutrino exchange is weaker. Through the violation of gauge theory cancellation the cross-section will become very sensitive to anomalous couplings. Though in early stages non-gauge invariant or non-unitary parametrisations were adopted, leading to huge changes in the cross-section, we now realise that to avoid contradiction of low energy results, a more complicated parametrisation is suitable. Along these lines, the effects on the total cross-section are usually small (away from obvious thresholds) and much of the effects are to be sought in the angular distributions.

1.5.2 Differential cross-sections

The cross-section for the reaction e$^+$e$^-$ $\to W^+W^-$ at fixed centre-of-mass energy $\sqrt{s}$, followed by the decay of the W^- and W^+ bosons into $f\bar{f}$ pairs, can be expressed in terms of 5 angular variables (see Figure 1.4) defined following the convention of reference [51]

- the W^- production angle Θ (as defined above);

- the decay angles (θ_1, ϕ_1) of the fermion in the rest frame of the W^-;
- the decay angles (θ_2, ϕ_2) of the anti-fermion in the rest frame of the W^+.

In the W^- frame we define the momentum of the decay fermion for $W^- \to f_1\overline{f}_2$ as

$$p_1^\mu = \frac{m_W}{2}(1, \sin\theta_1\cos\phi_1, \sin\theta_1\sin\phi_1, \cos\theta_1), \tag{1.23}$$

and, similarly, for $W^+ \to f_3\overline{f}_4$, the anti-fermion in the W^+ frame is given by

$$p_4^\mu = \frac{m_W}{2}(1, \sin\theta_2\cos\phi_2, -\sin\theta_2\sin\phi_2, -\cos\theta_2). \tag{1.24}$$

To obtain the five-fold differential angular distribution for the process $e^+e^- \to W^+W^- \to f_1\overline{f}_2 f_3\overline{f}_4$, in the narrow width approximation we combine the production and decay amplitudes

$$\begin{aligned}\frac{d^5\sigma(e^+e^- \to W^+W^- \to f_1\overline{f}_2 f_3\overline{f}_4)}{d\cos\Theta\, d\cos\theta_1\, d\phi_1\, d\cos\theta_2\, d\phi_2} = & \tfrac{\beta}{32\pi s}(\tfrac{3}{8\pi})^2 B(W \to f_1\overline{f}_2)B(W \to f_3\overline{f}_4) \\ & \times \textstyle\sum_{\sigma,\lambda,\overline{\lambda},\lambda',\overline{\lambda'}} F(\sigma,\lambda,\overline{\lambda})F^*(\sigma,\lambda',\overline{\lambda'}) \\ & \times D_{\lambda,\lambda'}(\theta_1,\phi_1) D_{\overline{\lambda},\overline{\lambda'}}(\pi-\theta_2, \phi_2+\pi).\end{aligned} \tag{1.25}$$

In this expression, $F_{\sigma\lambda\overline{\lambda}}$ is the helicity amplitude (which was called $\mathcal{M}$ in the previous section) for the production of the W^- and W^+ with respective helicities λ and $\overline{\lambda}$ from e^- and e^+ with helicities σ and $-\sigma$. These are functions of $\sqrt{s}$ and $\cos\Theta$, and contain the dependence on the coupling constants to be determined (see previous Section 1.5.1). These amplitudes have been calculated in [51, 53]. If the calculation is done in a gauge invariant way, the main effect of the TGC parameters is found in the angular distributions. The decay tensors $D_{\lambda,\lambda'}(\theta_1,\phi_1)$ and $D_{\lambda,\lambda'}(\pi-\theta_2,\phi_2+\pi)$, describing the W^- and W^+ decay angles respectively, are well-known functions based on the V-A decay of W bosons and depend only on the values of the relevant decay angles. The appearance of $\pi-\theta_2$ and $\phi_2+\pi$ in Equation 1.25 and in the decay tensors is due to the swap of particle with anti-particle. As can be seen from Figure 1.4 the transformation

$$\begin{aligned}\cos\theta_i &\leftrightarrow -\cos\theta_i; \\ \phi_i &\leftrightarrow \phi_i + \pi,\end{aligned}$$

corresponds to the exchange of the two decay products.
In case where only one of the W decays is observed, here assumed to be the W^-, an integration over the remaining angles results in the following expression:

$$\begin{aligned}\frac{d\sigma}{d\cos\Theta\, d\cos\theta_1\, d\phi_1} = & \tfrac{3\beta}{256\pi^2 s} B(W \to f_1\overline{f}_2) \\ & \times \textstyle\sum_{\sigma,\lambda,\lambda',\overline{\lambda},\overline{\lambda'}} F^\sigma_{\lambda\overline{\lambda}}(s,\cos\Theta) F^{*\sigma}_{\lambda'\overline{\lambda'}}(s,\cos\Theta) D_{\lambda\lambda'}(\theta_1,\phi_1).\end{aligned} \tag{1.26}$$

Finally if none of the decay angles is measured, integrating Formula 1.25 over all the decay angles of the W's leads to an expression for the differential cross-section as function of the production angle:

$$\frac{d\sigma}{d\cos\Theta} = \frac{\beta}{32\pi s}\sum_{\sigma\lambda\overline{\lambda}} |F^\sigma_{\lambda\overline{\lambda}}(s,\cos\Theta)|^2. \tag{1.27}$$

	TT $\lambda = \overline{\lambda}$	TT $\lambda = -\overline{\lambda}$	LL	LT
σ_0 Standard Model	s^{-3}	s^{-1}	s^{-1}	s^{-2}
$\delta\sigma$ For $\delta_Z \neq 0$	s^{-2}		constant	s^{-1}
$\delta\sigma$ For $x_Z, x_\gamma \neq 0$			constant	s^{-1}
$\delta\sigma$ For $y_Z, y_\gamma \neq 0$	s^{-1}			s^{-1}

Table 1.6: *The asymptotic behaviour and the distribution to the various helicity states for the Standard Model (top row) and of the various non-standard contributions.*

From Table 1.5 it is evident that not all TGC parameters contribute to all W^+W^- helicity states. Certain combinations of helicity amplitudes have a specific dependence on the coupling parameters. The longitudinal cross-section, proportional to $\sum_\sigma |F_{\sigma 00}|^2$, contributes to the dipole parameters κ_γ and κ_Z, but not to the quadrupole parameters λ_γ and λ_Z. The combination of the transverse helicity amplitudes $\sum_\sigma(|F_{\sigma--}|^2 + |F_{\sigma++}|^2)$ depends on quadrupole but not on the dipole couplings.
As the TGC parameters appear through similar terms in the helicity amplitudes one can anticipate strong correlations, as has been pointed out in reference [53], among certain sets of parameters like (δ_V, x_V, y_V).
At LEP-2, energies will be attained which bring us in the regime $s \gg M_Z^2$. It follows from Equation 1.22 and from the helicity amplitudes (expressions can be found in reference [53]) that $WW\gamma$ and WWZ couplings enter through combination in helicity amplitudes via terms

$$\frac{g_{WW\gamma}}{s} - \frac{g_{WWZ}(a - 2b\sigma)}{s - M_Z^2}, \tag{1.28}$$

with σ the electron helicity, $a = \frac{-1+4s_W^2}{4s_W c_W}$ and $b = -\frac{1}{4s_W c_W}$. This effect, which makes it difficult to disentangle both couplings, is referred to as the γ - Z conspiracy [53]. The only true possibility of disentangling $WW\gamma$ from WWZ would be to use e$^+$ and e$^-$ beam polarisation, where transversally polarised beams seem to be the most effective and the larger the degree of polarisation the better for disentangling the various $WW\gamma/WWZ$ couplings. Changing the centre-of-mass energy s would also have an effect and disentangle better the two couplings. However at LEP-2 we are working in a zone far away from the Z peak.
Consider the cross-section, $\sigma^{AA'}(s)$, where (A, A') = (L,T), for the production of W^+W^- pairs of definite helicities in the assumption that the anomalous couplings are sufficiently small [60]:

$$\sigma^{AA'}(s) = \sigma_0^{AA'}(s) + \sum_i x_i \Delta_i^{AA'}(s), +O(x_i^2), \tag{1.29}$$

where $\sigma_0^{AA'}$ denotes the Standard Model cross-section and the parameters x_i stand for the five anomalous couplings $(x_1, x_2, ..., x_5) = (\delta_Z, x_\gamma, ..., y_Z)$ (c.f. Section 1.4). The asymptotic behaviour ($s \gg 4M_W^2$) with centre-of-mass energy is shown in Table 1.6 for the different helicity

W decay channel	Decay fraction	Available angular information
$jjl\nu$	$l = e$: 14.7% $l = \mu$: 14.7% $l = \tau$: 14.7%	$\cos\Theta$ ($\cos\theta_l,\phi_l$) ($\cos\theta_j,\phi_j)_{folded}$
$jjjj$	46%	$\|\cos\Theta\|$ ($\cos\theta_{j_1},\phi_{j_1})_{folded}$ ($\cos\theta_{j_2},\phi_{j_2})_{folded}$
$l\nu l\nu$	10%	$\cos\Theta$ ($\cos\theta_1,\phi_1$) ($\cos\theta_2,\phi_2$) 2 solutions[4]

Table 1.7: *Availability of angular information in different WW final states. The production angle is denoted by Θ, and ($\theta_{l,j}, \phi_{l,j}$) denote decay angles for $W \rightarrow$ (leptons, jets) respectively. $(\cos\theta_j, \phi_j)_{folded}$ implies the ambiguity $\cos\theta_j \leftrightarrow -\cos\theta_j$, $\phi_j \leftrightarrow \phi_j + \pi$ incurred by the inability to distinguish quark from antiquark jets.*

states. The more rapid decline of the Standard Model contribution when compared to those of the couplings is the reason for the increasing sensitivity to the couplings with energy

$$\delta_Z, x_\gamma, x_Z, y_\gamma, y_Z \propto \sqrt{s\mathcal{L}}, \tag{1.30}$$

with $\mathcal{L}$ the integrated luminosity.
In the determination of the coupling parameters it is clearly preferable to use the full angular information from each event, represented by Equation 1.25, as this allows a separation for the various helicity amplitudes. Unfortunately the availability of angular information for an event depends on the W^+W^- final state because of ambiguities due to lack of knowledge about unmeasured neutrinos, quark flavours or W charge, the use of the differential cross-sections in this equation is complicated (c.f. Chapter 4). Three final states exist: $l\nu jj$, $jjjj$ and $l\nu l\nu$, also referred to as semi-leptonic, hadronic and leptonic channels, respectively. An overview of the available angular information per channel is given in Table 1.7. Ambiguities in angular information dilute the necessary information for TGCs.

1.5.3 Off-shell *W* pair production and four-fermion processes

The discussion of TGCs in the context of on-shell (narrow width approximation) W's and massless fermions, is only a first approximation from the point of view of studying effects of the TGCs. A full study of the TGCs will involve additional effects from the finite width of the decaying W's, initial state radiation and inclusion of the four-fermion background.
In this section the full process:

$$e^+e^- \rightarrow W^+W^- \rightarrow f_1 + \overline{f_2} + f_3 + \overline{f_4} \tag{1.31}$$

is described. The process described in Equation 1.31 involves two resonant W bosons in terms of Breit Wigner distributions, and introducing a finite width in the W propagator is the first step in the extension of the Born level on-shell CC03 cross-section. Figure 1.6 shows the W pair production cross-section in various approximations. As can be seen from this figure on-shell production of W^+W^- is not permitted for the region $\sqrt{s} < 2M_W$, and treating the W's as

[4] Although the problem is underconstrained, the neutrino momentum can be recovered, but is not unique as two solutions exist.

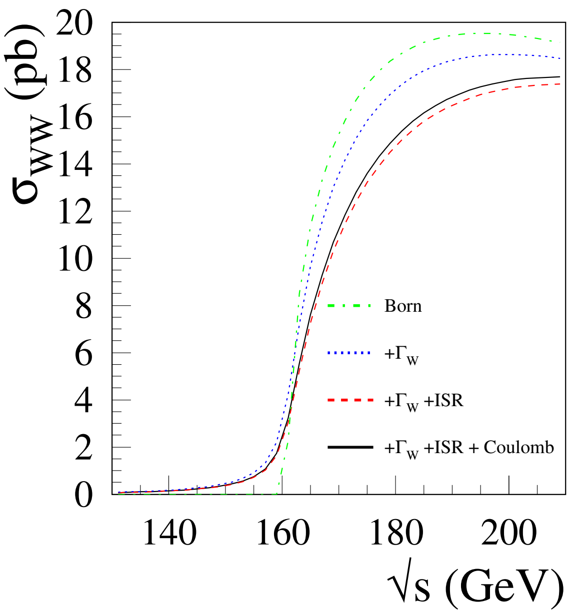

Figure 1.6: *W pair production cross-section in various approximations: at Born level (on-shell), at Born level (off-shell), with Initial State Radiation and with first order Coulomb correction.*

resonances has clearly the effect of smearing out the WW cross-section. In the leading order the off-shell cross-section for WW production can be written as [61]

$$\sigma(s) = \int_0^s ds_1 \int_0^{\sqrt{s}-\sqrt{s_1}} ds_2 \rho(s_1)\rho(s_2)\sigma_0(s, s_1, s_2), \tag{1.32}$$

with σ_0 the on-shell CC03 Born cross-section. The width of the W bosons is introduced by the Breit Wigner density $\rho(s)$:

$$\rho(s) = \frac{1}{\pi}\frac{\Gamma_W}{M_W}\frac{s}{(s - M_W^2)^2 + s^2\Gamma_W^2/M_W^2}, \tag{1.33}$$

with a mass dependent width $\Gamma_W(s) = s\Gamma_W/M_W$, where $\Gamma_W \equiv \Gamma_W(M_W^2)$.
If we have substituted the on-shell W's with their decay products, as in Equation 1.31, we are inevitably forced to consider the full four-fermion process [62]. This involves in the lowest order the production of two resonant W bosons and proceeds through the Feynman graphs given in Figure 1.3. These final states, consisting of four fermions, however can be produced through different intermediate states, which are considered as background processes to the two W boson production (which is the signal). These extra diagrams include diagrams for Z pair production, single W or Z production or even diagrams with no resonating bosons and they do not only contribute as background but as the final states are identical to the final state obtained through the CC03 diagrams, there is also interference between these processes [63]. All possible final states

can be subdivided into two classes. The first class comprises production of (up, anti-down) and (down, anti-up) fermion pairs:

$$(U_i, \overline{D}_i) + (D_j, \overline{U}_j), \tag{1.34}$$

where i and j are generation indices. The final states produced via virtual W pairs belong to this class. Therefore, we will call these "CC" or Charged Current type final states. The number of Feynman diagrams in the CC classes are shown in Table 1.8. Examples of CC processes are shown in Figure 1.3. The second class is the production of two fermion anti-fermion pairs:

$$(f_i\overline{f}_i) + (f_j\overline{f}_j), f = U, D. \tag{1.35}$$

As it is produced via a pair of two virtual neutral vector bosons we will call this a final state

	$\overline{d}u$	$\overline{s}c$	$\overline{e}\nu_e$	$\overline{\mu}\nu_\mu$	$\overline{\tau}\nu_\tau$
$d\overline{u}$	43	11	20	10	20
$e\overline{\nu}_e$	20	20	56	18	18
$\mu\overline{\nu}_\mu$	10	10	18	19	9

Table 1.8: *Number of lowest order Feynman graphs for the production of CC type final states.*

of "NC" or Neutral Current type. An example is shown in Figure 1.7(b). Obviously these two classes of final state overlap for certain cases. An example of the single W production which contributes to both classes is shown in Figure 1.7(a).

The `Excalibur` [64, 65] Monte Carlo event generator, which is used in this thesis, includes

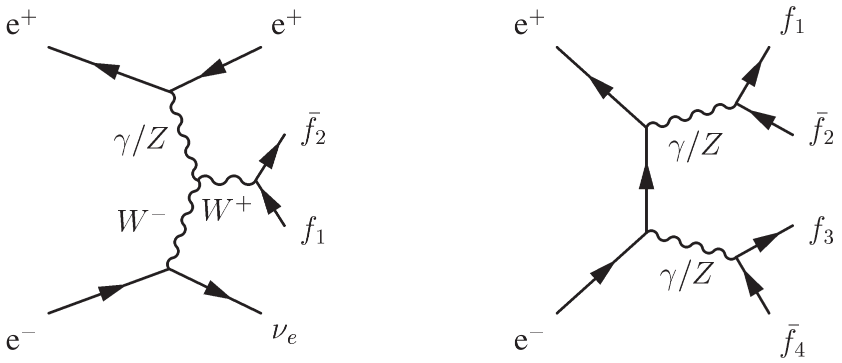

Figure 1.7: *Feynman diagrams for (a, left) single resonant W production and (b, right) an example for a four-fermion neutral current process.*

the full set of four-fermion diagrams with complete interference. This event generator uses a slightly different subdivision of all classes of contributing Feynman graphs. All possible classes of four-fermion diagrams are shown in Figure 1.8. The amplitudes receive contributions from "Abelian" and "non-Abelian" graphs, with two distinct topological structures. These so called generic diagrams make the assumption that all particles are out-going as can be seen from Figure 1.9. The particles and anti-particles can be assigned in six ways to the external lines by assigning + and $-$ to the helicity labels λ, ρ and σ. This gives a maximum of 144 different diagrams for the "Abelian" graphs and at most 8 for the "non-Abelian" diagrams. The contribution

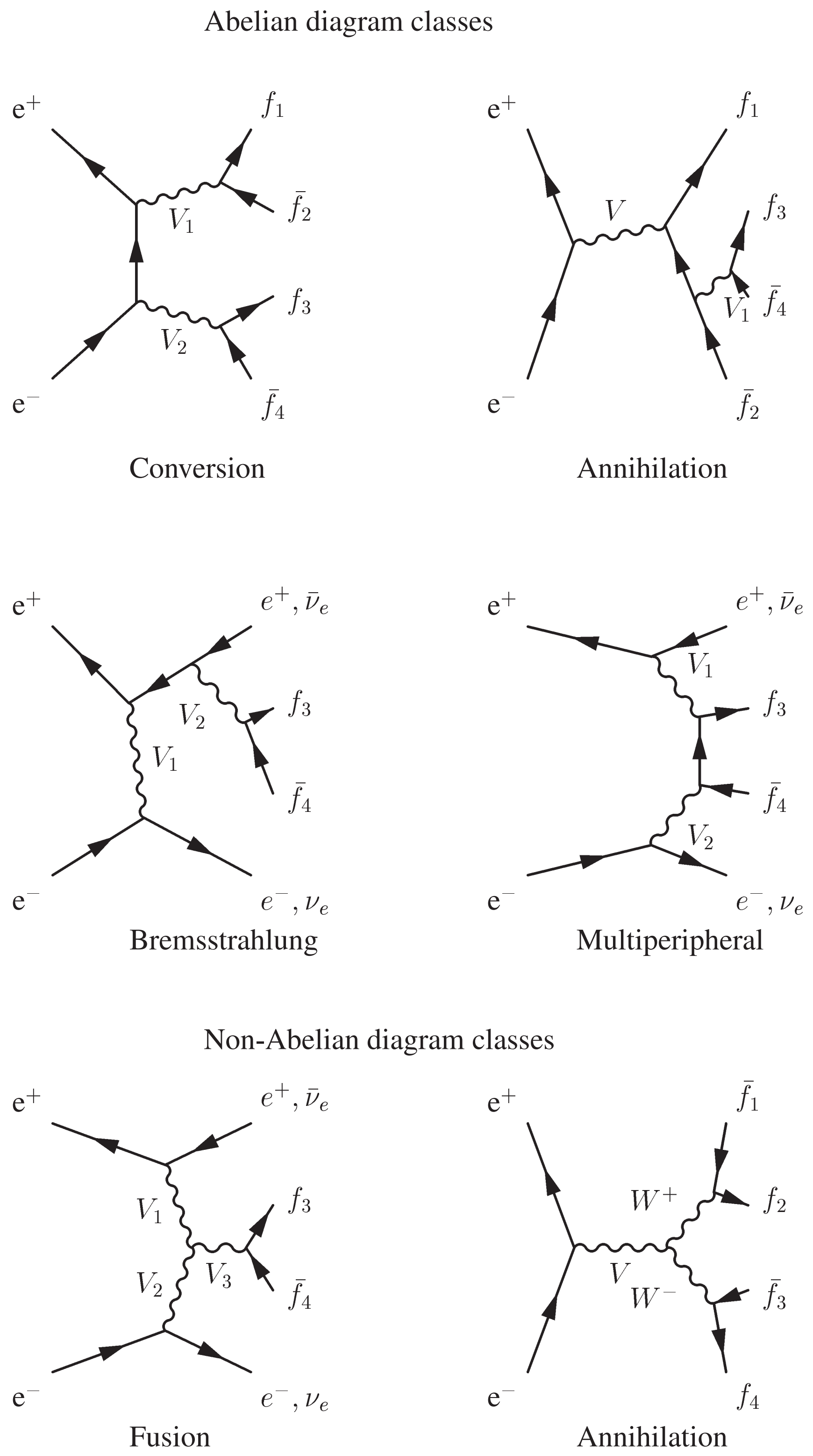

Figure 1.8: *Four-fermion production classes of diagrams, excluding Higgs graphs. The bosons $V_{1,2,3}$ denote either Z, $W^\pm$ or γ; V is either Z or γ.*

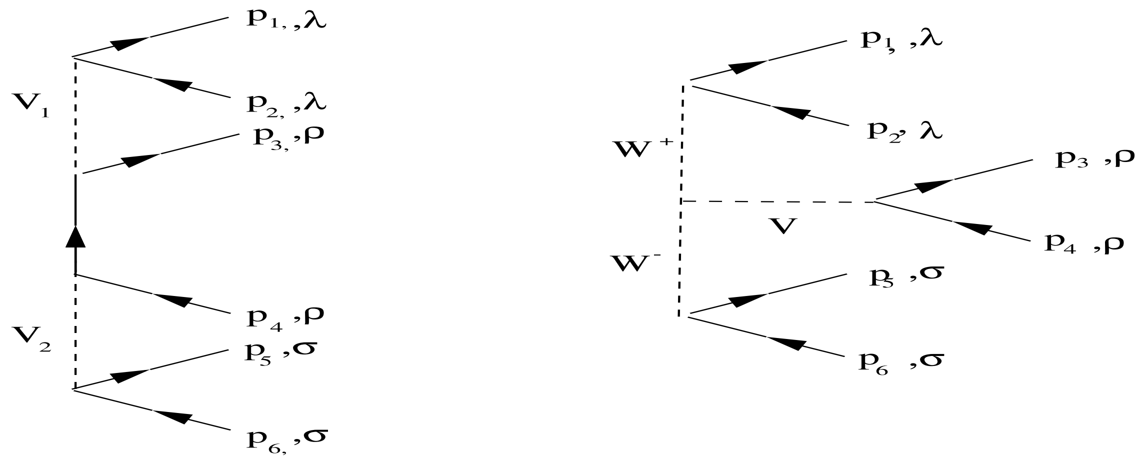

Figure 1.9: *Generic diagrams for four-fermion production excluding Higgs graphs. The bosons $V_{1,2}$ can be either Z, $W^{\pm}$ or γ; V can be either Z or γ. The diagram on the left-hand side represents the "Abelian" classes and the diagram on the right-hand side the "non-Abelian" classes of diagrams.*

of these extra final states and their interference is quite modest, but still can become large when the final state contains one or more electrons or ν_e. The diagrams relevant for W pair production are the "Abelian" conversion diagram and the "non-Abelian" annihilation diagram. In the latter the WWV vertex can be probed.
Given the very large number of possible diagrams it is necessary to implement an efficient algorithm for the construction of the diagrams and the calculation of the matrix elements in the Monte Carlo event generator. To do so the `Excalibur` event generator makes use of helicity amplitude techniques [62], which works under the assumption of massless fermions. This assumption means that all diagrams involving a Higgs boson which couples to fermions are neglected. As well as the inclusion of all possible diagrams with interference in the off-shell calculation the `Excalibur` event generator includes leading order photon radiation effects and CP-conserving Triple Gauge Boson Couplings.

1.5.4 Higher-order corrections

In addition to finite width and four-fermion contributions the W pair production is also affected by higher order corrections due to the width of the W and radiation of photons. The emission of photons from the incoming e^+ and e^- is called Initial State Radiation or ISR. The photons may also be emitted by the final W's and final state four-fermions, this process goes under the name Final State Radiation or FSR. Studies on these effects in the final state have been made [66], but as the effect is not important for the work presented in this thesis these results are not discussed here. When the photons are exchanged between the two W's we speak of Coulomb Correction. In this section an overview of these effects and their importance is given.

Initial State Radiation
The most significant correction to the W pair production cross-section at LEP-2 energies is the

radiation of photons from the incoming electrons and positrons. The ISR effect invokes corrections of $\sim 7\%$ [67]. Elaborate studies have been published and the reader is referred to these for more detailed information [67, 68].
The distinction between soft and hard photons should be made. The first have low energy ($E_\gamma/\mathrm{E_{beam}} << 1$) and are produced mostly collinear with the initial particle and have to compensate the infrared divergences. The emission of energetic photons has a more important experimental effect as it reduces the effective centre-of-mass energy ($\sqrt{s'}$) of the collision[5] and consequently affects the s-dependent forward peak in the differential cross-section $d\sigma/d\cos\theta$ distribution due to neutrino exchange. ISR also produces smearing of the total W pair production cross-section, as can be seen from Figure 1.6.
The ISR effect can be taken into account in different ways [67]. The method used to incorporate ISR effects in the `Excalibur` event generator uses the structure function [69] approach where the emission of photons with zero transverse momentum is incorporated. This approach assumes that the ISR is factorised and hence the cross-section can be written as

$$\sigma(s) = \int_0^1 \int_0^1 dx_1 dx_2 \Phi(x_1)\Phi(x_2)\sigma_0(x_1, x_2, s), \tag{1.36}$$

with $\sigma_0(x_1, x_2, s)$ the non-radiative Born cross-section and Φ the radiation function of the photons. An expression for Φ can be found in [69].
The version of the `Excalibur` generator used in DELPHI treats Initial State Radiation using the `Qedps` program [70] for the final states which do not include e$^+$e$^-$pairs and uses the default collinear treatment for final states including e$^+$e$^-$.

Coulomb Correction
The second important correction to the WW cross-section is the Coulomb Correction. This effect originates from the exchange of a photon between the two almost stationary W bosons in the final state. The effects of this correction are particularly dominant at threshold (6%), and fall rapidly with $\sqrt{s}$. At 190 GeV the effect is less than 2%. The effect on the total cross-section can be seen from Figure 1.6. Because of the fact that the Coulomb Corrections are screened by the finite width of the W bosons and the off-shell effects, higher order Coulomb Corrections are not important for off-shell W pair production and the TGC measurement. The Coulomb Correction is implemented in the `Excalibur` event generator.

1.5.5 Bose Einstein Correlation and Colour Reconnection

Interconnection phenomena [71, 72] may obscure the separate identity of the two W bosons, so that the final state may no longer be considered as a superposition of two separate W decays. The separation between the two W bosons at the time of their disintegration is of the order of 0.1 fm, which is a result of the W width. This distance is much smaller than the hadronisation scale in the fully hadronic $q\bar{q}Q\bar{Q}$ decay channel which is of the order of 1 fm. It is clear that the disintegration products of the W's are in a region of space-time where they may interact in the framework of QCD. The interconnection effects, which may play an important role in the determination of TGCs in the fully hadronic decay channel as the W direction may be influenced, considered here are Colour Reconnection and Bose Einstein effects.

[5]This process is called "return to the Z" in the case of $q\bar{q}\gamma$ events.

Colour Reconnection

Colour Reconnection [73] is the most commonly used term for the exchange of gluons between the decay products of the two W's. This exchange can take place at two stages. At parton level, the first stage in the decay of the W's, soft and hard gluons can be radiated. This effect can be described by perturbative QCD. Only fairly soft gluons (Energy $\lesssim \Gamma_W$), with a wavelength larger than the distance between the W decay vertices, will feel the joint action of all four quark colour charges. Colour Reconnection in the perturbative decay space is expected to be a small effect.
In the second stage the fragmentations become correlated as the effect is characterised by a distance of ~ 1 fm. Describing the size of the non-perturbative distortions one has to rely on phenomenological models, which were tuned to describe the high statistics LEP-1 data taken at the Z peak, instead of on exact calculations. The introduction of Colour Reconnection is likely to affect the general event shape predictions of the model. Colour Reconnection models have been incorporated in the `Ariadne, Herwig` and `Pythia` fragmentation packages.
With the data taken at LEP-2 the challenge is open to study the phenomenon of Colour Reconnection in hadronic WW events and it could provide a new probe for non-perturbative QCD dynamics.

Bose Einstein effect

Bose Einstein effects [72] are interference effects between identical bosons with small momentum separations. In the hadronisation process of the W decay products large number of pions are produced and, as already noted above, the space time regions of the two decaying W's are overlapping. It is clear that Bose Einstein effects may occur between the two W's.
This well known effect has been observed in the decay products of the Z LEP-1 data [74]. It also has been observed in the decay products of single W hadronic decays [75]. It is not yet established whether Bose Einstein Correlations exist between decay products of different W's. As there is a serious lack of theoretical formulation these effects are studied with phenomenological models [76]. It is expected that these will affect the measurement of the W boson mass but do not have much influence on the measurement of the Triple Gauge Boson Couplings.

Chapter 2

Experimental set-up The DELPHI detector and the LEP accelerator

2.1 Introduction

In this chapter an overview of the LEP collider and the DELPHI detector is given. DELPHI or DEtector for Lepton, Photon and Hadron Identification has a vast number of sub-detectors each of which is described. In the last part of this chapter the trigger and data read-out system as well as the offline processing software is commented.
Further information on the subjects discussed in this chapter can be found in references [77, 78] for DELPHI and [79, 80, 81, 82] for LEP .

2.2 The LEP accelerator

The Large Electron Positron collider (LEP) is situated near the French-Swiss border at the CERN laboratory. This ring, consisting of eight alternating straight and curved sections, has a circumference of 27 km and lies in a tunnel complex at an average depth of 100 m. The particles are injected in the main LEP ring at an energy of 20 GeV. To achieve this energy the electrons and positrons go through an injector chain consisting of the 5 pre-injectors. In a first step a linear accelerator or linac accelerates electrons to 200 MeV and shoots them on a target to create positrons. These electrons and positrons are then accelerated to 600 MeV by a second linac. These 600 MeV particles are stored in the Electron-Positron Accumulator (EPA) which injects them into the CERN Proton Synchrotron (PS). Here the particles are accelerated to 3.5 GeV. In a last step the PS injects into the SPS or the CERN Super Proton Synchrotron which operates as a 20 GeV electron-positron injector for LEP. After injection in the main ring electrons and positrons circulate in opposite directions in so called bunches, or small packets of particles. The two particle beams are separated by electrostatic separators. These are installed in each of the eight possible collision points and prevent the beams from colliding before a sufficient number of particles could be accumulated and accelerated to their nominal energies. A schematic overview of LEP and its injector chain is depicted in Figure 2.1.

Within the straight sections of the main LEP ring e$^-$ and e$^+$ particles are accelerated to their nom-

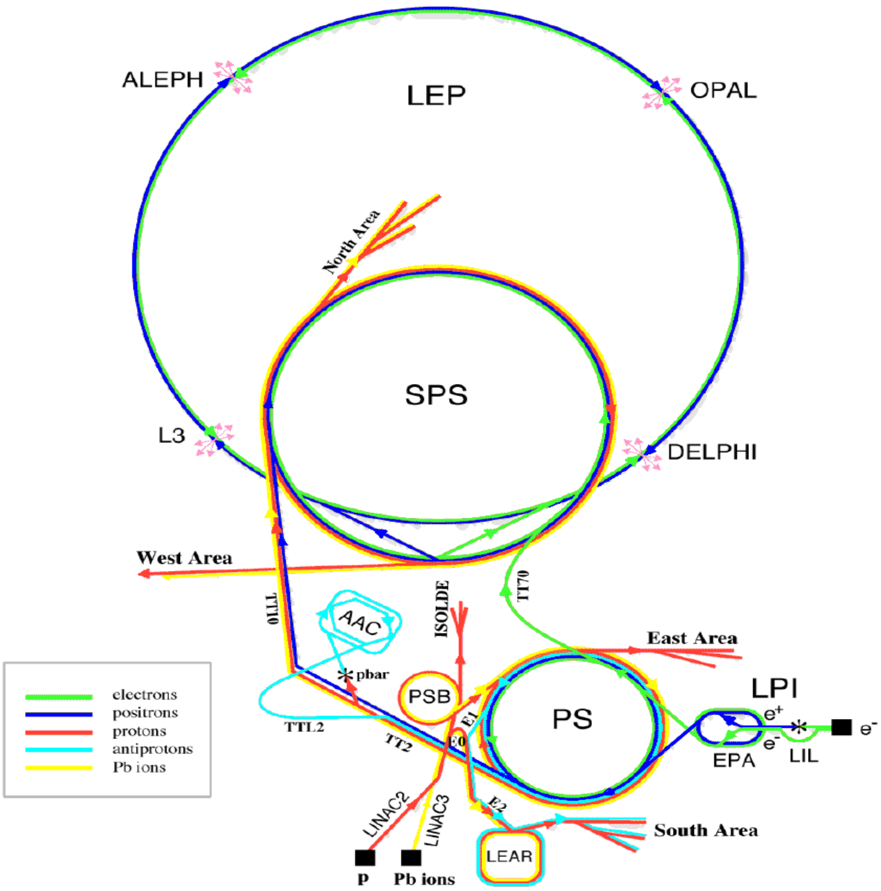

Figure 2.1: *Schematical representation of the CERN accelerators.*

inal energies, by a system consisting of 52 copper and 272 superconducting RF cavities. Once the required energy has been achieved LEP is operated as a storage ring. The RF cavities are used to continually replenish the energy lost in synchrotron radiation by the particles on each revolution. The radiation loss per revolution of a particle of energy E_{beam} (the beam energy) being bent in a circular path of radius r is proportional to E^4_{beam}/r.

The electromagnetic field guide system bends the particles in the curved sections and keeps the beam in its place within the vacuum pipe. The complete magnet system consists of dipoles, quadrupoles, sextupoles, horizontal and vertical dipole correctors. The strings of dipole magnets bend the electrons and positrons in a piecewise circular trajectory. The quadrupoles act as focusing lenses on the beam to contain it in the vacuum chamber. The sextupoles compensate for the dependence of the focusing strength on the beam energy. The horizontal and vertical correctors steer the beam through the centre of the vacuum pipe.

In four of the straight sections multi-purpose detectors are installed: L3, ALEPH, OPAL and DELPHI. The detectors are located in these straight sections to protect them against synchrotron radiation. In the centre of each detector the electron and positron beams collide head-on (whenever nominal energies are attained after the so called ramping) in what is called the interaction point (IP). Each experimental collision point is surrounded by a large solenoidal magnet.

The two fundamental design parameters of a particle accelerator are the beam energy range and the luminosity. The first one must be sufficient to allow observation of the interesting physical processes, the second one ensures that these events are produced at a reasonable rate.
The initial goal of LEP was a high accuracy study of Z bosons. Approximately four million Z events were collected and studied by each of the four experiments during the first seven years of operation (1989-1995). In what is called phase two (LEP-2, started in 1996) precision measurements of the $W^{+/-}$ bosons are being carried out. So LEP was designed to run with a beam energy ranging from 40 up to 100 GeV.
The rate at which events are produced is determined by the total cross section σ of the corresponding process and the luminosity $\mathcal{L}$ of the colliding beams:

$$\frac{dN}{dt} = \sigma\mathcal{L}. \tag{2.1}$$

The integrated luminosity $L = \int \mathcal{L}dt$ over the duration of the experiment is a good measure of the statistics of a data sample. For identical beams colliding head-on, the luminosity at any collision point can be expressed in terms of beam parameters:

$$\mathcal{L} = \frac{N_b^2 f_b}{A}, \tag{2.2}$$

where A is the effective transverse elliptical cross section of the beam at a collision point, N_b the number of particles in a bunch and f_b the frequency at which collisions take place in the experiment. In order to increase the luminosity, the bunches of each beam must be tightly focused to very small dimensions in the centre of the IP of the detectors. This is accomplished by a set of superconducting quadrupoles with very strong field gradients that focus the transverse beam dimensions to ~ 10 μm and 250 μm in the vertical and horizontal plane respectively. The number of particles in a bunch is mainly limited by beam-beam interactions.
In this thesis the data collected in 1997 and 1998 will be used. In that phase of LEP the collider operated at centre-of-mass energies of respectively 183 GeV and 189 GeV. At these energies the integrated luminosity delivered by LEP to the experiments was ~ 60 and ~ 175 pb^{-1}. In both years LEP was operated with four bunches of electrons and four bunches of positrons circulating in the ring. The time between beam cross-overs (BCOs) was 22 μs.

2.3 The DELPHI detector

The DELPHI detector is one of the four experiments operating at LEP, designed for e$^+$e$^-$physics. This general purpose detector aims at a powerful particle identification, high track reconstruction efficiency, good calorimetric performance and a precise vertex identification and reconstruction over a 4π solid angle. The detector itself is installed in a cavern 100 m below ground and consists of a barrel (cylindrical section) and two end-caps. The latter can be axially moved to allow access to the sub-detectors. The detector has an overall length and diameter of over 10 m.
The DELPHI experiment is built up out of different sub-detectors each giving three-dimensional information about the impact points or energy deposition due to a traversing particle. The following sections describe the track reconstruction, the energy reconstruction in the calorimeters and particle identification. The present layout of the barrel and one end-cap of the DELPHI detector is shown schematically in Figure 2.2.

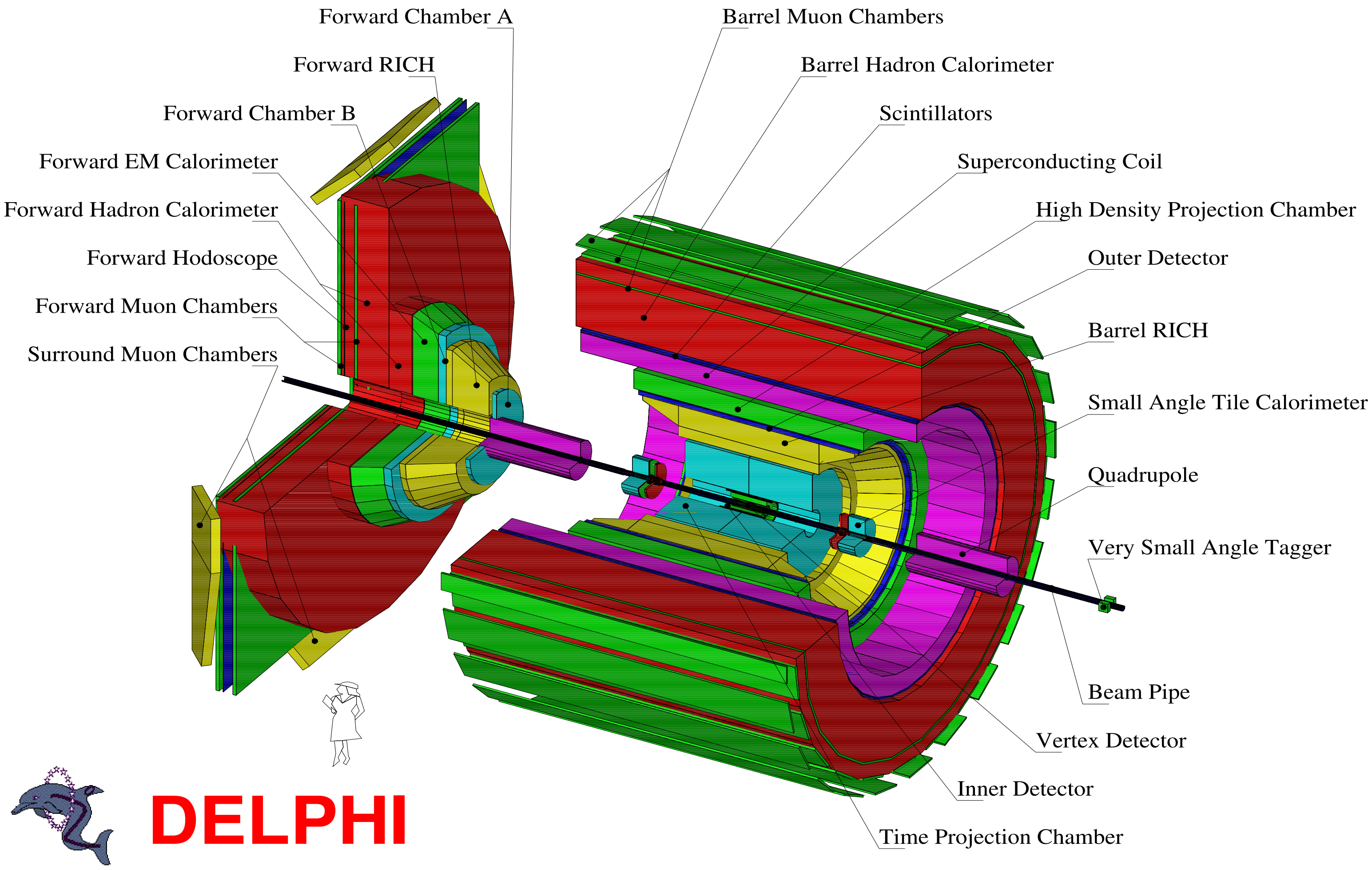

Figure 2.2: *A cut-away view of the DELPHI detector.*

In the standard DELPHI coordinate system the z axis is along the e$^-$ direction, the x axis points towards the centre of LEP and the y axis points upwards. Cylindrical coordinates are also used: the polar angle to the z axis is θ and the azimuthal angle around z is called ϕ. The radial coordinate R is defined as being equal to $(x^2+y^2)^{1/2}$. These coordinate systems are illustrated in Figure 2.3.

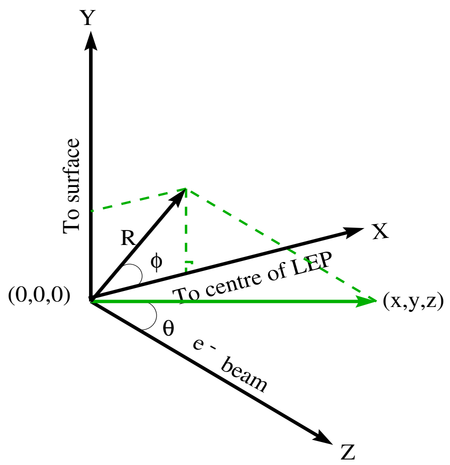

Figure 2.3: *The* DELPHI *coordinate systems (x,y,z) and (R,ϕ,θ), are defined with respect to the nominal centre of* DELPHI .

2.3.1 Tracking detectors

In DELPHI charged particle tracks are reconstructed by a software program called `Delana` [83] that associates the track elements found by the sub-detectors. The main characteristics of this program will be given later. The ensemble of tracking detectors is enclosed in the superconducting solenoid which generates a highly uniform magnetic field of 1.2 T parallel to the z axis. The curvature of a particle traversing this field is used to measure its charge and momentum. An overview of position, resolution and acceptance of the central tracking system can be found in Table 2.1.

	Position R(cm)	$\mid$ z $\mid$ (cm)	Acceptance θ(deg)	No. Points along track	Resolution per point σ (mm)
VD (barrel)	6.6/9.2/10.6	$\leq$ 24	$\geq$ 21	$R\phi$: 3 z: 2	$R\phi$: 0.008 z: 0.010
VFT			11-26	4	x,y: 0.1
ID drift ID straws	11.8 - 22.3 23-28	$\leq$62 $\leq$105	$\geq$15 $\geq$15	24 5	$R\phi$: 0.085 $R\phi$: 0.25
TPC	35-111	$\leq$ 134	$\geq$20	$R\phi$,z: 16 $R\phi$: 192	$R\phi$: 0.23 z: 0.9
OD	198-206	$\leq$ 232	$\geq$43	$R\phi$: 5 z: 3	$R\phi$: 0.11 z: 44
FCA	30-103	155-165	11-33	6	0.3
FCB	53-195	267-283	11-35	12	0.25

Table 2.1: *Specifications and performance of the* DELPHI *central tracking system. The acceptance is measured in absolute value of θ and goes up to 90^0.*

- **Micro-vertex detector (VD)** [84]
  The micro-vertex detector, in its present configuration, was installed in 1996 and consists of barrel and forward region parts. Three coaxial cylindrical layers of silicon strip detectors build up the barrel region. Each shell consists of 24 slightly overlapping sectors assuring a full azimuthal coverage and four detectors are placed along the z direction. Two out of the three layers are equipped with double sided microstrip silicon detectors (with the strips orthogonally placed) so information on the z coordinate can also be read out. All three layers provide a maximum resolution in $R\phi$ measurements.
  The forward region part or Very Forward Tracker as it is called was installed in 1996 and was fully operational in 1997. Each side consists of two layers of pixels and two layers of back-to-back mini-strip detectors. The aim of this detector is to improve the tracking efficiency and resolution in a polar angle region from 11^0 up to 25^0.

- **Inner detector (ID)**
  The Inner Detector consists of two concentric sections. The innermost part is a drift chamber built up of 24 azimuthal sectors which give up to 24 $R\phi$ space points along the track of a charged particle traversing the chamber. The second part of this detector consists of 5 cylindrical layers of straw tube detectors providing further $R\phi$ information. These layers were introduced in 1995 and are mainly used in triggering. They solve as well the left/right ambiguities inherent to the jet chamber.

- **Time Projection Chamber (TPC)**
  The TPC is the principal tracking device; all pattern recognition starts from its information. This information consists of the three-dimensional space point information and the measurement of particle dE/dx. These measurements are made when a particle traverses the TPC gas volume causing ionisation. The generated drift field is parallel to the DELPHI magnetic field. The produced electrons drift to one of the two end-caps of the TPC, which are divided into 6 azimuthal sectors. Each sector is a multi-wire proportional chamber with 192 sense wires and 16 circular cathode pad rows.

The inclusion of the RICH detectors in DELPHI limited the size of the TPC detector. This implied that additional track chambers were installed to improve momentum resolution.

- **Outer detector (OD)**
  The OD consists of 5 layers of drift tubes operated in limited streamer mode. All layers provide $R\phi$ information and three layers read out the z coordinate. This detector is essential for fast triggering and improves the momentum resolution.

- **Forward chambers (FCA and FCB)**
  The Forward Chambers A are positioned on opposite sides of DELPHI next to the end-caps of the TPC. On each side the chambers consist of three modules, each one built up of two staggered planes of drift tubes operated in limited streamer mode. Between the tubes of two modules there is a rotation of 120^0 allowing a three dimensional readout.
  A second tracking detector, FCB, is installed in the end-caps between the RICH and the electromagnetic calorimeters. FCB is a drift chamber which consists of 12 read out planes of wires. FCA provides together with FCB a powerful tracking and triggering in the forward region.

2.3.2 Calorimeters

The energy of the neutral and charged particles is measured by the DELPHI calorimetry system. This system consists of the electromagnetic calorimeters, where the deposited energy of the electrons and photons is measured, and the hadron calorimeter. An overview of the specifications of the different calorimetric detectors in DELPHI is given in Table 2.2.

	Position R(cm)	$\mid$ z $\mid$(cm)	Acceptance θ(deg)	Depth	Resolution (σ_E/E)(%)
HPC	208-260	$\leq$254	≥ 43	$18X_0(\sim 0.6\lambda)$	$.043 \oplus \frac{.32}{\sqrt{E}}$
FEMC	46-240	284-340	10-36.5	$20X_0(\sim 1\lambda)$	$.003 \oplus \frac{.12}{\sqrt{E}} \oplus \frac{.11}{E}$
HCAL barrel	320-479	< 380	≥ 43	$\sim 6\lambda(\sim 57X_0)$	$.21 \oplus \frac{1.12}{\sqrt{E}}$
HCAL forward	65-460	340-489	10-43	$\sim 6\lambda(\sim 57X_0)$	
STIC	6.4-41	218-249	1.7-10.6	$27X_0$	$.0152 \oplus \frac{.135}{\sqrt{E}}$

Table 2.2: *Specifications of the* DELPHI *calorimeters. The acceptance is measured in absolute value of θ and goes up to 90^0.*

- **Electromagnetic Calorimeters**
When an electron or photon enters the electromagnetic calorimetry system it will develop an electromagnetic shower through e^+e^- pair production and Bremsstrahlung processes. The radiation length X_0, depending on the material, is the parameter describing the development of an electromagnetic shower as it enters into the expression describing the energy loss $\frac{dE}{dx}$ by Bremsstrahlung of an electron of very high energy E:

$$(\frac{dE}{dx}) \sim -\frac{E}{X_0}. \tag{2.3}$$

The specifications of the different electromagnetic calorimetry systems used in DELPHI are given in Table 2.2, their various designs are described hereafter:

  - **High Density Projection Chamber (HPC)**
  In the barrel region the 144 modules of the HPC collect the charges from electromagnetic showers using a time projection technique. Each module is a small TPC with layers of a high density material dividing the gas volume. The layers of lead wire act as converter material and provide also the electrical drift field. As in the TPC a proportional wire chamber is used to read out the drift volume. Hence a three dimensional image of the electromagnetic shower can be obtained.
  - **Forward Electromagnetic Calorimeter (FEMC)**
  The FEMC consists of two arrays (one in each end-cap) of 4532 lead glass truncated pyramids pointing to the interaction region. Charged particles of electromagnetic showers developed in these blocks emit Cherenkov photons which are detected by photomultipliers placed at the end of each block.
  - **Small Angle Tile Calorimeter (STIC) and Very Small Angle Taggers (VSAT)**
  In the very forward region at very low angle the STIC and VSAT[1] are used. They

[1] The VSAT is not used in this analysis.

mainly serve for luminosity measurements using Bhabha scattering at very low angles. The STIC built according to the “shashlik” technique [85, 86], is a sampling lead-scintillator calorimeter formed by two cylindrical detectors placed on either side of the DELPHI interaction region. Perpendicular threaded through the lead-scintillator layers are optical fibres reading out the light produced in the scintillators. The reconstruction of the shower direction is aided by two layers of silicon strip detectors embedded in the front part of the calorimeter.

For cabling purposes, the electromagnetic calorimetry system of DELPHI, consisting of the HPC and FEMC, has cracks in its coverage. These exist at $\theta = 40^0$ and $\theta = 140^0$ and between the HPC modules in ϕ and at 90^0 polar angle. Supplementary photon taggers are installed to cover these gaps and obtain complete hermiticity.

- **Hadronic Calorimeter (HCAL)**
  Hadron calorimeters rely on detecting the showers of secondary particles produced by inelastic hadronic interactions with the nucleons of the converter material. The interaction length λ, mentioned in Table 2.2 is defined in a material as the mean free path of a particle before undergoing an inelastic interaction. The Hadron Calorimeter or HCAL is a sampling calorimeter where the converter material, consisting of iron plates (forming the return yoke of the magnet), is sandwiched between radiation sensitive layers of limited streamer tubes. The HCAL measures the hadronic energy in both the end-caps and the barrel region.

2.3.3 Identification of particles

Good particle identification is one of the important characteristics of the DELPHI detector. Some detectors like the RICH (Ring Imaging Cherenkov) and muon chambers are especially designed for this purpose, others like the calorimeters and TPC have particle identification as a secondary function.

- **Identification of electrons by the TPC, HPC and FEMC**
  As already mentioned the TPC provides the dE/dx measurement which is the specific ionisation energy loss per unit length. For a given momentum this energy loss of a particle depends on its velocity. This measurement together with the energy deposit in the HPC or FEMC is used for electron identification.

- **Identification of muons**
  The ensemble of muon chambers, consisting of three separate sub-detectors covering the whole polar angle region, is placed near the outside of the DELPHI detector. The specifications are described in Table 2.3. The principle of muon identification is simple: most of the hadrons are stopped in the HCAL and do not succeed in penetrating the muon chambers, while almost all muons of an energy over 2 GeV reach the chambers. A correspondence between the trajectory interpolation and the signal in the muon chambers is then made.

  - **Barrel Muon Chambers (MUB)**
    The MUB consists of three layers of muon chamber modules. The inner layer lies

	Position R(cm)	$\mid$ z $\mid$(cm)	Acceptance θ(deg)	No. Points along track	Resolution per point σ(mm)
MUB	$\sim$ 445	$\leq$ 385	52-128	2-6	$R\phi$: 1.5 z: 10
MUF	70-460	463/500	9-43	$4(x, y)$	(x, y): 5.0
MUS	550	487	42-53	2	10×10

Table 2.3: *Specifications and performances of the* DELPHI *muon chambers. The resolution quoted for the MUS is given in the local coordinate system of each chamber.*

20 cm inside the iron of the Hadron Calorimeter, and the two outer layers outside the iron. Each MUB module is built up of two active layers comprising staggered planes of drift chambers operated in proportional mode. The drift time of the electrons on the anode wire, placed centrally in every drift chamber, is used to determine the $R\phi$ coordinate. A delay line sits opposite every anode wire. This allows to determine the z coordinate by measuring the relative timing of the signals travelling on this delay line to the ends of the chamber.

– **Forward Muon Chambers (MUF)**
The forward muon chambers consist of two detection planes for each end-cap. The first plane lies 20 cm inside the iron of the forward Hadron Calorimeter, the second one outside. Each plane comprises four quadrants, consisting of two orthogonal layers of 22 drift chambers operated in limited streamer mode. The MUF reads out two cartesian coordinates (x, y), these are derived from the anode drift time and the timing of the delay line signal.

– **Surround Muon Chambers (MUS)**
The Surround Muon Chambers consist of 8 modules and are installed at each end of DELPHI to cover the gap at a polar angle $\theta \sim 45^0$ between the MUF and the MUB. Each module consists of two staggered layers of streamer tubes.

- **Ring Imaging Cherenkov detectors**[2]
Particle identification founded on the dE/dx measurement of the TPC becomes more delicate for momenta higher than a few GeV. For these particles (electrons, pions, kaons and protons) the RICH detectors, reconstructing the Cherenkov angle in the barrel and end-cap region, allow a powerful identification.

2.3.4 Scintillators

- **Forward Hodoscope (HOF)**
In between the two detection planes of the MUF a layer of scintillators is placed providing a fast muon trigger.

[2]The RICH detectors are not used in this analysis.

- **Time of Flight counter (TOF)**
  A cylinder of scintillator counters lies between the solenoid and its return yoke. They provide a fast event triggering in the barrel region.

2.3.5 Trigger system

To be able to cope with the high luminosities and large backgrounds (beam-gas interactions, cosmic events,...) a triggering algorithm composed of four successive levels of increasing selectivity exists:

- **Level 1 (T1)**
  The T1 decision is taken 3.5 μs after the BCO. This trigger acts as a loose pre-trigger using the input from detectors with fast read-out times: ID, OD, FCA, FCB, the scintillators, FEMC and MUB. The T1 rate is typically $\sim$ 500 Hz.

- **Level 2 (T2)**
  The T2 decision is taken 39 μs after the BCO with signals coming from the TPC, HPC and MUF. The T2 trigger rate is typically $\sim$ 5 Hz.

The level 3 and 4 trigger (T3 and T4) are software filters performed asynchronously with respect to the BCO. T3 repeats the T2 logic using more detailed detector information and again halves the background passing T2. The final trigger level T4 is based on a tailored version of the DELPHI reconstruction program `Delana` (Section 2.3.6) and halves roughly the trigger rate of T3.

2.3.6 Data Acquisition System, offline processing and data simulation

The Data Acquisition System (DAS) [78] digitizes, reads and stores the data from the detector for subsequent analysis. The raw data are also used to monitor the detector performance online (Quality Checking). Detector operation is monitored and controlled by the Slow Controls system [87].
To produce data suitable for direct use in physics analyses the raw data has to be processed by the DELPHI offline system. The main component of this processing is performed by the DELPHI central processing program `Delana` [83]. This program applies the calibration correction, pattern recognition algorithms and track fitting. At this stage identification algorithms are used as well. The output of `Delana` is stored on magnetic tapes, called Data Summary Tapes (DST), in a format based on `Zebra` [88]. The subsequent analyses extracting and analysing the information on these DSTs rely upon packages like `Phdst` [89] and `Skelana` [90].
A program called `Delsim` [91] simulates the detector response for the neutral and charged particles in generated events traversing the detector. This program produces simulated raw data in the same format as the real data and in a next step the `Delana` program is applied to produce a DST tape, in a manner analogous to that used on the real data.

Chapter 3

Event selection

3.1 Introduction

As the W bosons are short lived ($\Gamma_W \sim 2$ GeV), the two W bosons produced in the e$^+$e$^-$ annihilation give rise to three different final state topologies:

- HADRONIC CHANNEL: e$^+$e$^-$ $\rightarrow W^+W^- \rightarrow q\bar{q}Q\bar{Q}$, BR $\sim$ 46%;
- SEMI-LEPTONIC CHANNEL: e$^+$e$^-$ $\rightarrow W^+W^- \rightarrow q\bar{q}l\nu$, BR $\sim$ 44%;
- LEPTONIC CHANNEL: e$^+$e$^-$ $\rightarrow W^+W^- \rightarrow l\nu l\nu$, BR $\sim$ 10%.

The notation used above is generic: $l = l^+$ or l^-, $\nu = \bar{\nu}$ or ν and $q\bar{q} = q_1\bar{q}_2$. In the analysis described in this thesis we determine the Triple Gauge Boson Couplings (TGC) parameters with the fully hadronic events, taken at centre-of-mass energies of 183 GeV and 189 GeV. This decay channel has a substantial branching ratio ($\sim$ 46%) and is expected to add significant information in the parameters determination. Following the SM and with the luminosity taken at 183 and 189 GeV we expect to produce 355 and 1139 events in the hadronic channel at the respective energies. In Figure 3.1 an example of a $W^+W^- \rightarrow q\bar{q}Q\bar{Q}$ decay is shown. This event, taken at a centre-of-mass energy of 189 GeV, illustrates the typical topology of such events. Four well spaced jets are observed and the high number of particle tracks use the full detector space. We see that the energy is deposited throughout the 4π detector. Another characteristic of this class of events is the important amount of visible energy, which should be close to collision energy as energy can only be lost by particles escaping in detector cracks or in the beam pipe, or by neutrinos in decay processes. According to this specific topology, a selection procedure, closely following the DELPHI procedure described in [92], has been developed. The ensemble of variables used to separate the fully hadronic events from the background, which is mainly dominated by $q\bar{q}(\gamma)$ and ZZ events, is discussed in the second half of this chapter (Section 3.9). Before describing the event selection all the necessary ingredients for, and steps preceding this signal selection are presented. First a short overview of the Monte Carlo generators used in this analysis is given. Another subject presented in the first part of this chapter is the track selection and its goals. The measurement of the beam energy and luminosity are also explained. The run quality study is discussed. The principles of the clustering algorithm used and the constrained fit are presented.

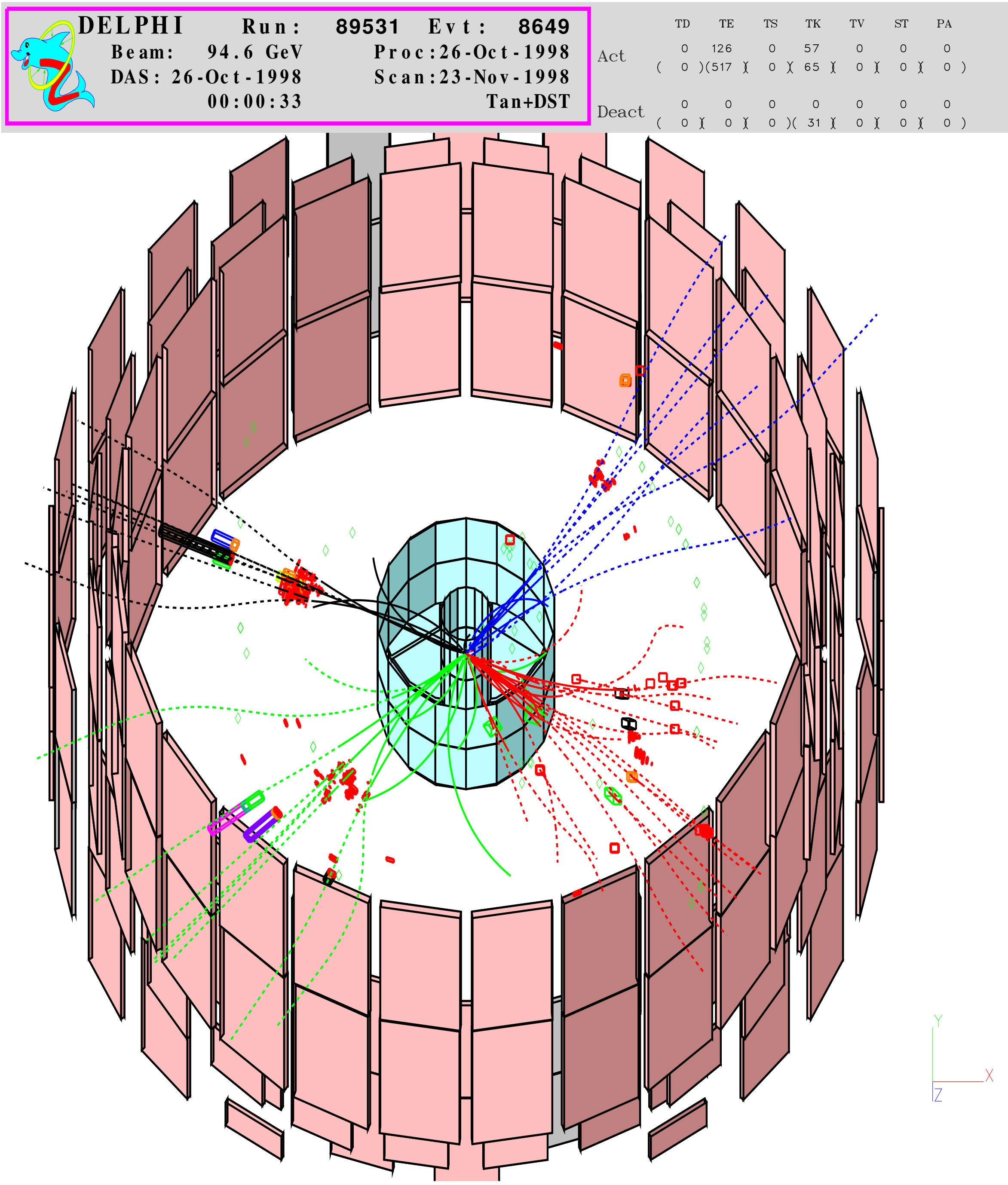

Figure 3.1: *An example of a $q\bar{q}Q\bar{Q}$ event observed in the* DELPHI *detector at* $\sqrt{s}$ = *189 GeV.*

3.2 Event simulation

The event generators are used to simulate the production of the full set of final state particles that would result from a given physics process. This occurs in three main stages, first the primary hard process, followed by the parton shower and finally the hadronisation model. Figure 3.2 gives a schematic overview of the different steps in the generation process. The particles obtained are then passed through the detector simulation program called `Delsim` in the case of the DELPHI experiment (see Section 2.3.6).
The primary hard process describing the signal we are interested in is

$$\mathrm{e}^+\mathrm{e}^- \to W^+W^- \to f_1\bar{f}_2f_3\bar{f}_4, \tag{3.1}$$

where $f_{i=1-4}$ stands for fermion. Two generators were used for this process: `Pythia` [93] and `Excalibur` [64]. The latter is already described in Chapter 1, Section 1.5.3. The `Pythia` generator generates the WW pair production process at CC03 level, including Final State Radiation (FSR) and Initial State Radiation (ISR) effects.
In the following perturbative phase the parton showers are produced, as is indicated in Figure 3.2. The most commonly used description of this parton shower mechanism is the `Jetset` [93] algorithm. The evolution is stopped at a fixed mass scale when fragmentation takes over.
Quarks and gluons do not exist in a free state. Perturbative QCD cannot currently provide full theoretical insight into the transition of the primary quarks to the observable hadrons, which brings us to the last step in the generation process which is shown in Figure 3.2. In the description of this so called fragmentation or hadronisation process phenomenological models are used. The fragmentation model used here is that in `Jetset`, which is based on the Lund string scheme [94]. When a quark and an anti-quark move apart with large energies a colour field is stretched between them. This field breaks into pieces with the production of new quark anti-quark pairs and finally hadrons.
The cross-sections for typical SM processes at LEP-2 are given in Figure 3.3. In Section 3.9 we discuss how to select the signal process in which we are interested: $\mathrm{e}^+\mathrm{e}^- \to W^+W^- \to q\bar{q}Q\bar{Q}$. The main background processes to this channel are

- $\mathrm{e}^+\mathrm{e}^- \to Z/\gamma \to q\bar{q}(+ng)(\gamma)$ with $n \geq 0$,
- $\mathrm{e}^+\mathrm{e}^- \to ZZ$,
- $\mathrm{e}^+\mathrm{e}^- \to W^+W^- \to q\bar{q}l\bar{\nu}$,
- $\mathrm{e}^+\mathrm{e}^- \to Z/\gamma \to Z\mathrm{e}^+\mathrm{e}^-$,

abbreviated throughout the text as $q\bar{q}(\gamma)$, ZZ, the semi-leptonic channel and Zee respectively.
An overview of the simulated samples used in this analysis and their cross-sections is given in Table 3.1. In addition to these samples, all generated at SM values of the anomalous TGC couplings, samples with non-SM values were also used. These are described in Chapter 4.

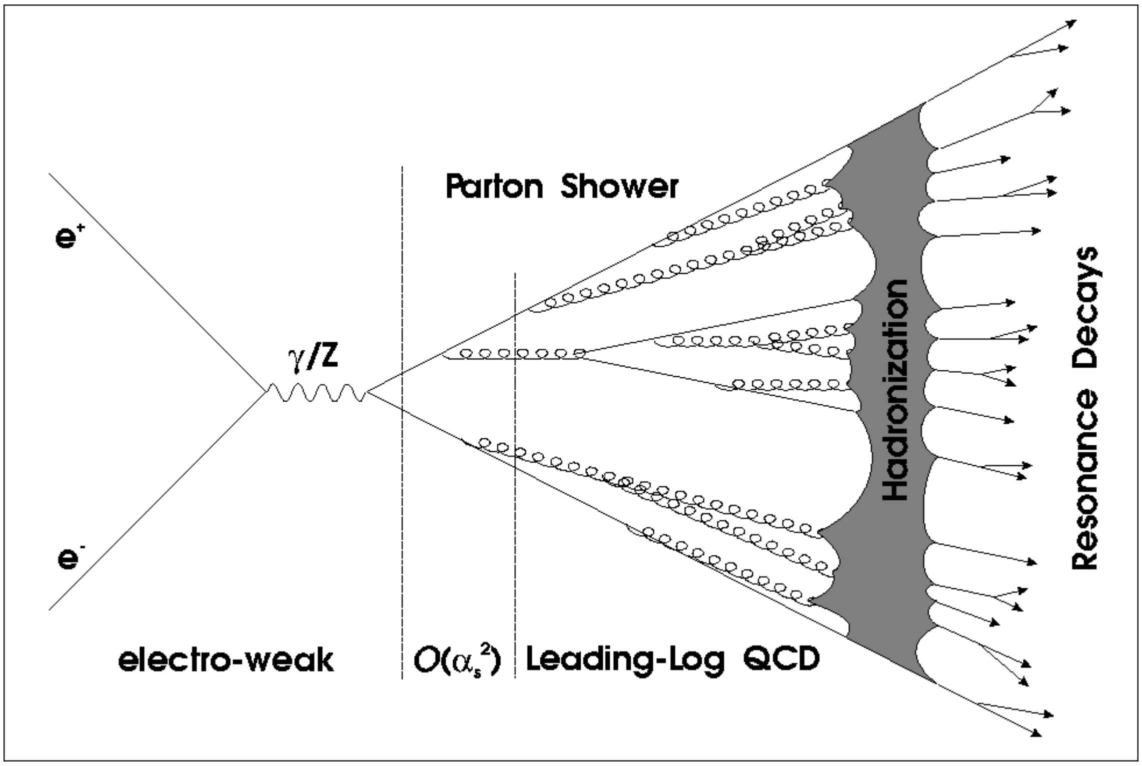

Figure 3.2: *The different steps in the generation process: the electroweak part (left side) followed by the parton shower and the hadronisation process.*

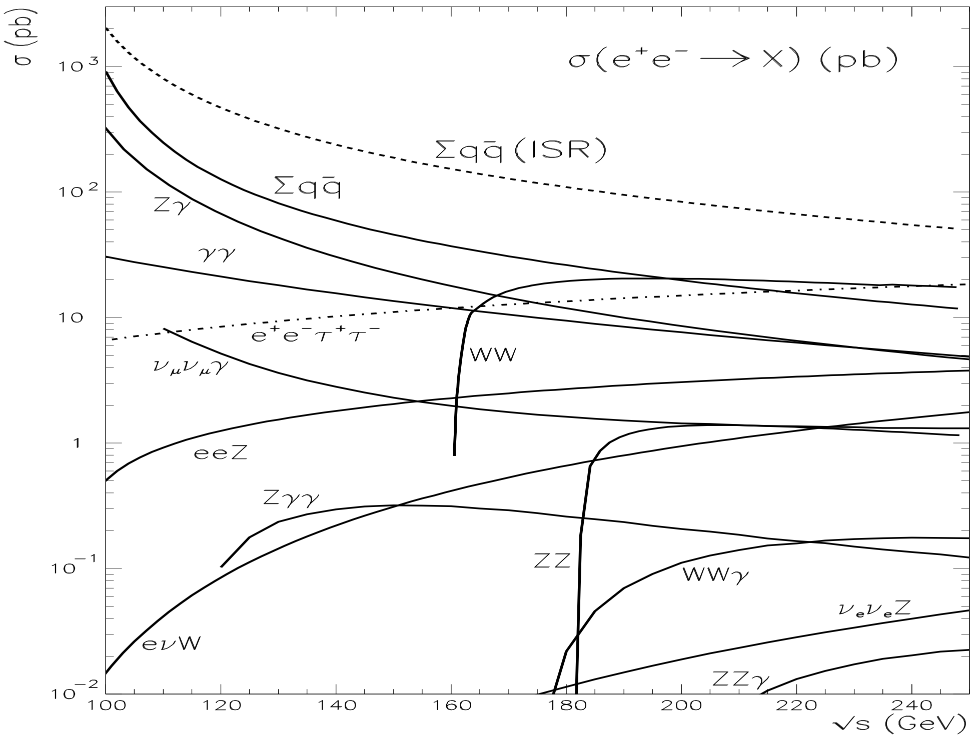

Figure 3.3: *Cross-sections for some typical standard model processes at LEP-2 energies.*

Process	MC Generator	$\sqrt{s}$ = 183 GeV		$\sqrt{s}$ = 189 GeV	
		σ (pb)	$\mathcal{L}$ (pb^{-1})	σ (pb)	$\mathcal{L}$ (pb^{-1})
$q\bar{q}(\gamma)$	`Pythia`	106	274	99.5	1688
ZZ	`Pythia`	1.338	4786	1.587	8266
Zee	`Pythia`	6.81	374	8.161	3099
WW	`Pythia`	15.44	2752	16.51	6535
$q\bar{q}Q\bar{Q}$	`Excalibur`	7.547	1613	8.02	206

Table 3.1: *The different Monte Carlo samples and cross-sections of the different processes presented in this analysis. The cross-section values for the $q\bar{q}(\gamma)$ process were calculated with* `Zfitter` *[95], the cross-sections for the other processes are taken from the corresponding generator.*

3.3 Selection of charged and neutral particle tracks

The aim of the particle track selection is twofold: on one hand this procedure improves the measurement quality of the kinematic parameters and on the other hand we hope to remove fake particle tracks (e.g. coming from electronic noise or pattern recognition faillures), cosmic rays and tracks coming from beam-gas interaction or secondary interactions (for instance with detector material). This procedure ensures that the charged particle tracks come from the primary e$^+$e$^-$ interaction vertex and as well that the selected charged particle tracks are well measured. The energy of neutral particles can be badly measured due to fake clusters in the calorimeters induced by electronic noise.
A particle track selection throwing away all these tracks is necessary as it is impossible to include all the effects, which have been described above, in the simulation. After the selection procedure a better description of the global event follows naturally as the agreement between data and Monte Carlo improves at the level of the charged and neutral particle track reconstruction. We wish to retain the maximum amount of kinematical information available for our analysis. Tracks that have been badly reconstructed are rejected the effects of which are corrected for in a later stage of this analysis.
The principles of the track selection, which is the DELPHI standard track selection, are implemented in `Skelana` [90] and are explained in the next two sections.

3.3.1 Charged particle tracks

The selection of good charged particle tracks is based on the momentum measurement, the error on the measured energy and the impact parameter.

Impact Parameters
The impact parameters of a track IP$_{R\Phi}$ and IP$_Z$ are defined from the distance of closest approach of the charged particle track extrapolation to the centre of the e$^+$e$^-$interaction region, in the $R\Phi$ plane and along the e$^-$ beam axis respectively. The definition of the DELPHI coordinate system can be found in Section 2.3 and in Figure 2.3. A cut on these parameters rejects badly reconstructed charged particle tracks, cosmic radiation particles, tracks from beam-gas interactions

and tracks which are not coming from the primary vertex. These can originate from the decay of lambdas ($\Lambda \rightarrow p\pi$) or neutral kaons ($K_s^0 \rightarrow \pi^+\pi^-$). Photons may also interact and produce secondary electron-positron pairs. The cuts imposed on these parameters IP are:

- $\mathrm{IP}_{R\Phi} \leq 4$ cm,
- $\mathrm{IP}_Z \leq 4$ cm/$\sin\theta$,

where the latter cut varies with the polar angle θ of the track. This dependence is introduced because the z coordinate of the point of closest approach is a less reliable indicator of the tracks true z distance of closest approach when the track is travelling in the forward direction.

Track momentum and error on the energy
When the momentum of a charged particle is too low, the reconstruction of its track becomes inprecise. This is due to the small radius of curvature. Therefore a cut on the measured momentum is applied:

- $|\vec{p}_{ch}| > 200$ MeV/c.

An additional cut on the energy of a charged particle is imposed in order to remove badly determined particle trajectories. The track energy E is computed out of the particles momentum and its mass (set to the pion mass). Tracks with an error on the energy ΔE larger than the track energy E are rejected.

High momentum tracks
Unphysical high momentum particles, this means that their measured energy is significantly higher than 90 GeV, are the result of a bad reconstruction of their trajectory. In the selected hadronic events, before track selection has been applied, approximately 0.08% of the particles have a momentum greater than 75% of the beam energy E_{beam}[1]. Failure to remove such a track could bias an event and affect the reconstructed direction of the initial partons (jet axis for instance). Such unphysical tracks were rejected by removing all tracks which had a reconstructed energy greater than 1.5 times the beam energy. The energy of the track was calculated assuming the pion mass.

Tracking detectors
Furthermore tracks which are only seen by the Vertex Detector were dropped. So are the tracks which are only reconstructed by the Vertex Detector and Inner Detector without any z information. The VD (Vertex Detector) and ID (Inner Detector) are described in Section 2.3.1.

3.3.2 Neutral particles

Approximately one third of all energy in an event is carried by neutral particles. These were reconstructed from the electromagnetic and hadronic showers which are deposited in the DELPHI

[1]Tracking algorithms have improved over the years which makes that the fraction of unphysical high energy tracks is strongly reduced. To be specific: one out of 400 tracks had a momentum greater than 2/3 of the beam energy during the 1996 data taking.

calorimetry system (see Section 2.3.2). Firstly showers reconstructed in the calorimeters were associated to charged particle tracks extrapolated to the calorimeters, as remaining showers were identified as coming from neutral particles if they satisfied certain criteria. In order to eliminate electronic noise in the calorimeters the following cuts are made:

- the cluster energy of
  - HPC had to be greater than 500 MeV,
  - FEMC had to be greater than 400 MeV,
  - STIC had to be greater than 300 MeV,
- the hadronic energy deposited in the HCAL had to be greater than 900 MeV.

3.4 Run quality selection

Data were only included in the data sample if they were collected during runs where the relevant DELPHI subdetectors (see Section 2.3) were performing correctly. The following criteria, optimized for hadronic events, were imposed on the selected run files:

- the TPC, HPC and EMF data taking efficiency for the run was greater than 90%,
- the TPC status flags on event-by-event basis [96] were verified in order to assure that the high voltages were on and the TPC was fully operational for the DAS (see Section 2.3.6).

3.5 Luminosity

The luminosity was derived from the rate of events due to Bhabha scattering reconstructed in the high precision Small Angle Tile Calorimeter (STIC) of which a description can be found in Section 2.3.2. The total integrated luminosity for the two data taking periods considered in this analysis corresponds to 53 pb^{-1} and 155 pb^{-1}. The errors are estimated to be $\pm$ 0.6%, which is dominated by the experimental uncertainty on the Bhabha measurements of $\pm$ 0.5% ([92] and [97]).
After the run quality selection the luminosity for the analysed data samples is 52.6 pb^{-1} at 183 GeV and 154.39 pb^{-1} at 189 GeV, which is a reduction of 0.8% and 0.4% respectively. An overview of the luminosities for the two centre-of-mass energies is provided in Table 3.2.

3.6 Beam energy

At energies well above the Z resonance the LEP energy cannot be determined directly by resonant depolarisation. The centre-of-mass energies for the data taken in 1997 and 1998 are determined by using a model of the LEP energy [98, 99]. The estimated uncertainties on the LEP beam energies are 25 and 20 MeV at beam energies of 91.5 and 94.5 GeV respectively. The luminosity weighted average beam energies 182.65 GeV and 188.63 GeV are referred to as 183 GeV and 189 GeV respectively throughout the text.

Centre-of-mass energy (GeV) (GeV)	Luminosity (pb^{-1})	Luminosity after run qual.(pb^{-1})
182.65	53	52.6
188.63	155	154.39

Table 3.2: *The table gives an overview of average centre-of-mass energy and corresponding luminosity, recorded by the* DELPHI *experiment (second column) during the runs in 1997 and 1998 and the luminosity after the run quality selection has been applied (third column). The values are taken from references [92] and [97].*

3.7 Jet clusterisation algorithm

To determine the original W direction from the full set of reconstrcuted particles observed in the event we need to know which final state particles belong to which primary quark. These primary quarks originate from the hadronic decays of the W bosons. From a combinatorial point of view numerous ways exist to attribute these particles to their parent W. It is quite impossible to try out all these in order to reconstruct the original W boson. Hence jet clustering algorithms become an indispensable tool in the study of multi-hadronic events. From the full set of tracks observed in the event the number of primary quarks and their directions and energies is obtained from regrouping the tracks in clusters using kinematical information.
A large number of jet clusterisation algorithms has been suggested and an overview can be found in [100]. The algorithms all start from the large list of particles considered as an initial set of clusters.
The jet reconstruction in this analysis is performed by means of the `Durham` algorithm [101, 102]. The distance measure d_{ij} between cluster i and j, using the transverse momentum, is defined as

$$d_{ij}^2 = 2min(E_i^2, E_j^2)(1 - \cos\theta_{ij}), \tag{3.2}$$

with θ_{ij} the angle between the two clusters. The scaled or dimensionless expression

$$y_{ij} = \frac{d_{ij}^2}{E_{vis}^2}, \tag{3.3}$$

normalised to E_{vis}, the visible energy in the event (which will be used in this analysis, see Section 3.9), is more common. The visible energy E_{vis} would agree with the centre-of-mass energy for a perfect detector to the extent that some particles are lost or mismeasured.
Two of these clusters (i and j) are grouped into a new one k if their relative "distance" is found to be smaller than a certain desired separation cut value d_{cut}. The four-momentum of the new cluster k is found from its constituents i and j by simple addition of the four-momenta $p_k = p_i + p_j$. This joining is repeated until all pairs of clusters have a separation above d_{cut} and the final set of clusters is then called a set of jets.

3.8 Kinematic reconstruction

The presence of neutrinos in the event, the fact that some particle tracks are not reconstructed (in the blind zones of the detector) and errors on the measurement of energy and momentum of the particle tracks affect the jet reconstruction. A correction can be made for these effects on the base of kinematical arguments [71]. With the requirement of energy and momentum conservation (4 constraints) on the event the losses in energy and momentum can be compensated for.
In this analysis the constrained fitting algorithm described in references [103, 104] was used. In this way all information available in the event is used. The fit can be performed using only the constraints of energy and momentum conservation or also including the constraint that the masses of the two reconstructed W's be equal or including that the two masses are equal to a certain value (compatible with the W boson mass distribution). In the hadronic channel this gives a 4C, 5C or 6C fit respectively. In such a fit the measured parameters are varied until a solution is found which satisfies the constraints imposed and also minimizes the χ^2 difference between the measured and the fitted values.
Figure 3.4 shows, for Monte Carlo simulated events, the difference in resolution on the polar angle and energy of the reconstructed W boson before and after a 4C kinematic fit has been performed. As the errors on the jet energies are much larger than the errors on the angular measurements, we see that the direction of the jets (and hence the W boson) is much less affected than the jet energy (and the W boson energy).

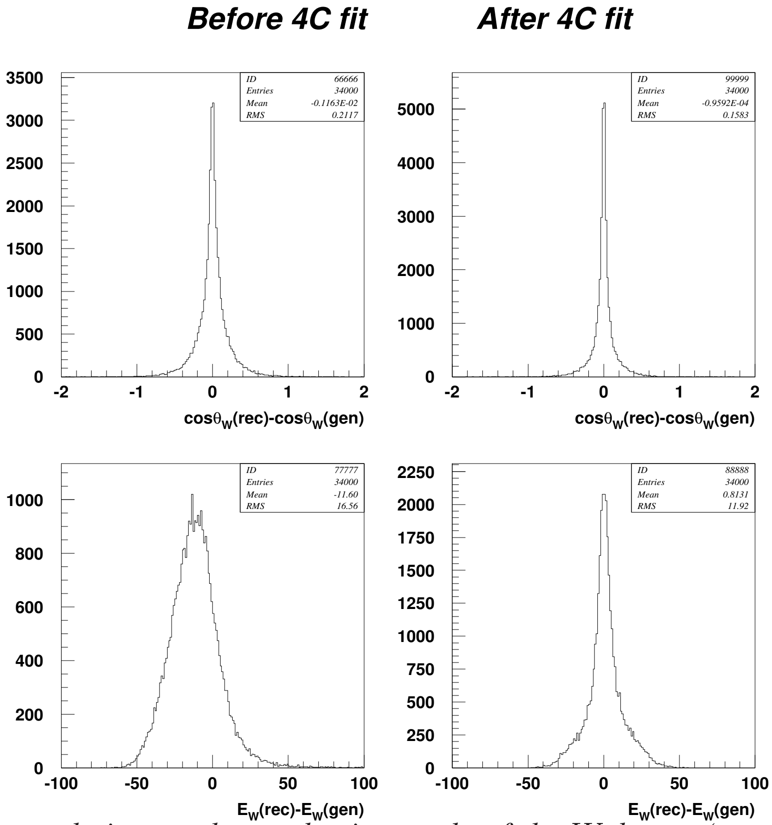

Figure 3.4: *The resolution on the production angle of the W boson (upper plots) and on the measured energy of the W boson (lower plots) before (left-hand side) and after (right) performing a 4C kinematic fit on MC simulated events.*

3.9 Selection of the signal: $e^+e^- \to W^+W^- \to q\overline{q}Q\overline{Q}$

In this section the different variables used to select the signal events $e^+e^- \to W^+W^- \to q\overline{q}Q\overline{Q}$ will be described. The signal selection starts from the events which contain only well measured tracks. The `Pythia` generator samples have been used for the signal and background processes. As has been said in the introduction Section 3.1 the events are characterised by an important visible energy, a high charged multiplicity and often four well spaced jets. The Standard Model cross-sections for the signal process are $\sim$ 7.1 pb and $\sim$ 7.6 pb at respectively 183 GeV and 189 GeV. A difficulty in the selection of hadronic WW decays is the presence of a large irreducible background from : $e^+e^- \to Z/\gamma \to q\bar{q}(+ng)(\gamma)$, and other backgrounds like $e^+e^- \to ZZ$, the semi-leptonic WW decays and the Zee channel. An overview of the cross-sections for typical SM processes is given in Figure 3.3 and illustrates the difficulty to select the signal process. The other background processes mentioned in Figure 3.3 can easily be reduced by simple cuts as will be shown in the next paragraphs.
The QCD process $e^+e^- \to Z \to q\bar{q}(+ng)(\gamma)$ has a cross-section of 106 pb at 183 GeV and 99 pb at 189 GeV, which is about a factor 6 higher than the WW production process (see Table 3.1). This process can be subdivided into two classes depending on the virtuality of the Z:

- the production of an on mass shell Z accompanied by a hard radiative photon normally escaping in the beam pipe,
- events with a soft ISR photon and as a consequence a large visible energy, which constitute the potentially most dangerous QCD background contribution.

The variables and cut values used to select the samples at centre-of-mass energy of 183 GeV are the same as at 189 GeV, unless stated otherwise. They are listed hereafter.

Charged particle multiplicity
Imposing a cut on the charged particle multiplicity removes all low multiplicity reactions, such as dilepton production, two-photon processes and the fully leptonic WW decay modes. With an average of $\sim$ 35 charged particle tracks per event, coming from the hadronisation process, the $W^+W^- \to q\bar{q}Q\bar{Q}$ is a high multiplicity process. The distribution of the charged particle multiplicity after all cuts (including the cut on the charged multiplicity) is shown in Figure 3.5. Imposing that the number of charged tracks per event must be greater than or equal to 14 eliminates all these low multiplicity processes without cutting in the signal process.

Visible energy
A cut on the visible energy of the event is efficient to reduce the $q\bar{q}\gamma$ background events with a photon collinear to the beam axis and to cut away a large part of the events which are characterised by a large missing energy as in $WW \to q\bar{q}l\bar{\nu}$ events. The visible energy E_{vis} is the sum of all energies measured in the DELPHI detector, coming from charged and neutral particles. The cut used for optimal reduction of the background processes without removing the signal events, was $E_{vis} > 1.15E_{beam}$. In Figure 3.6 this distribution is shown after all cuts have been made.

Effective centre-of-mass energy
In $q\bar{q}\gamma$ events very energetic photon(s) with total energy E_γ and momentum p_γ are emitted in the

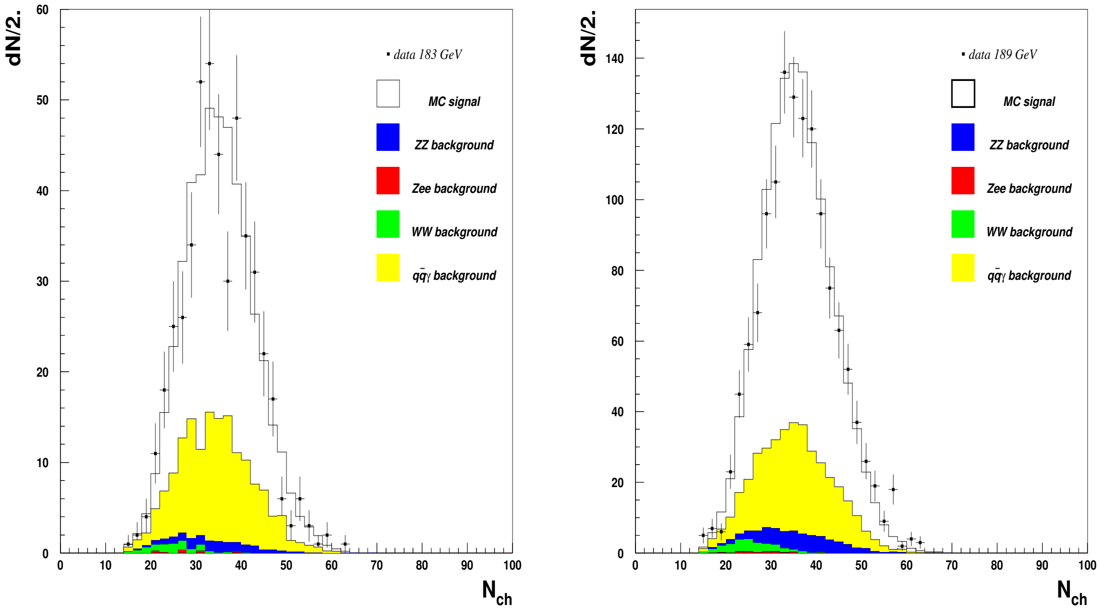

Figure 3.5: *The charged multiplicity distribution after all cuts have been made, for data (points), signal MC (white area) and background MC (hatched areas). The figure on the left is for the data taken at 183 GeV, the figure at the right is for the data taken at 189 GeV.*

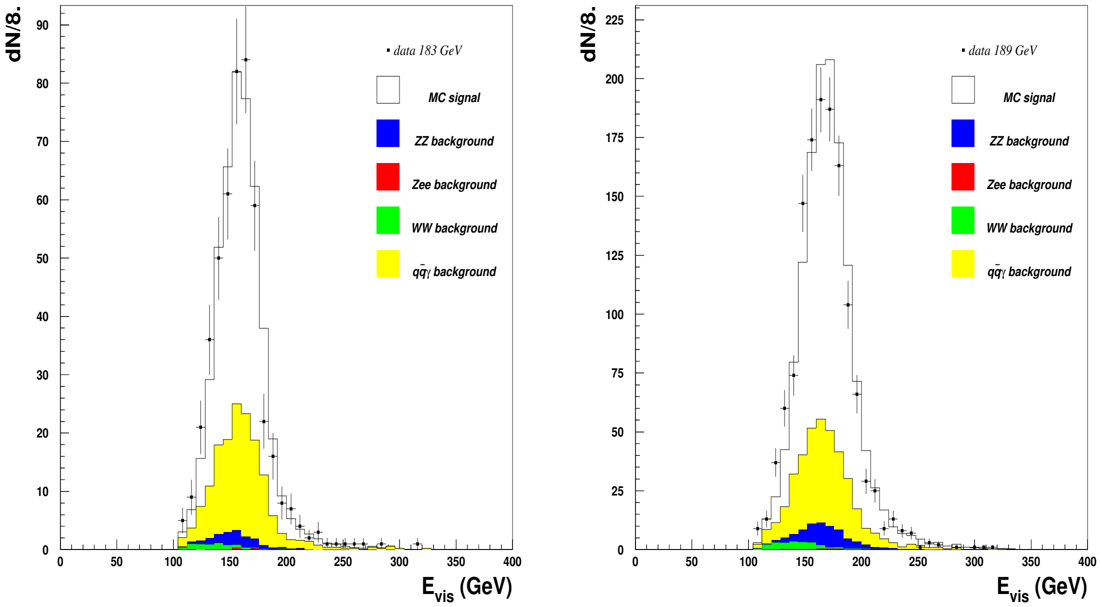

Figure 3.6: *The distribution of the visible energy in the event after all cuts have been made, for data (points), signal MC (white area) and background MC (hatched areas). The figure on the left is for the data taken at 183 GeV, the figure at the right is for the data taken at 189 GeV.*

initial state. The energy in the centre-of-mass of the e^+e^- collision has a high probability to be reduced to the effective centre-of-mass energy $\sqrt{s'}$:

$$\sqrt{s'} = \sqrt{(\sqrt{s} - E_\gamma)^2 - E_\gamma^2}. \tag{3.4}$$

If there is return to the Z peak (Z *radiative return* events) the effective centre-of-mass energy is reduced to the Z mass and consequently the energy of the photons E_γ will be equal to $(s - M_Z^2)/(2\sqrt{s})$.
By calculating the effective centre-of-mass energy $\sqrt{s'}$ and imposing a cut on this variable one is able to cut away a large part of the radiative return events. As in semi-leptonic events the amount of missing energy is large the effective centre-of-mass energy $\sqrt{s'}$ will be significantly lower for these events than for the signal events. In this way this variable can be used as well to make a discrimination of these events.
The DELPHI `Sprime+` [105] package is used for the calculation of the effective centre-of-mass energy. This method computes the effective centre-of-mass energy in e^+e^- annihilation by determining the energy and momentum of ISR photons from a constrained fit.
The distribution of the variable $\sqrt{s'}/\sqrt{s}$ is shown in Figure 3.7 showing a double peak structure, where the first smaller bump (at $\sqrt{s'}/\sqrt{s} \sim .5$) is populated with $e^+e^- \to q\bar{q}\gamma$ events while the second peak at $\sqrt{s'} \sim \sqrt{s}$ is mainly populated with the $q\bar{q}Q\bar{Q}$ events. As can be seen from these plots cutting at $\sqrt{s'}$ greater than 150 GeV halves the amount of the radiative QCD events and cuts away some of the semi-leptonic W^+W^-decays.

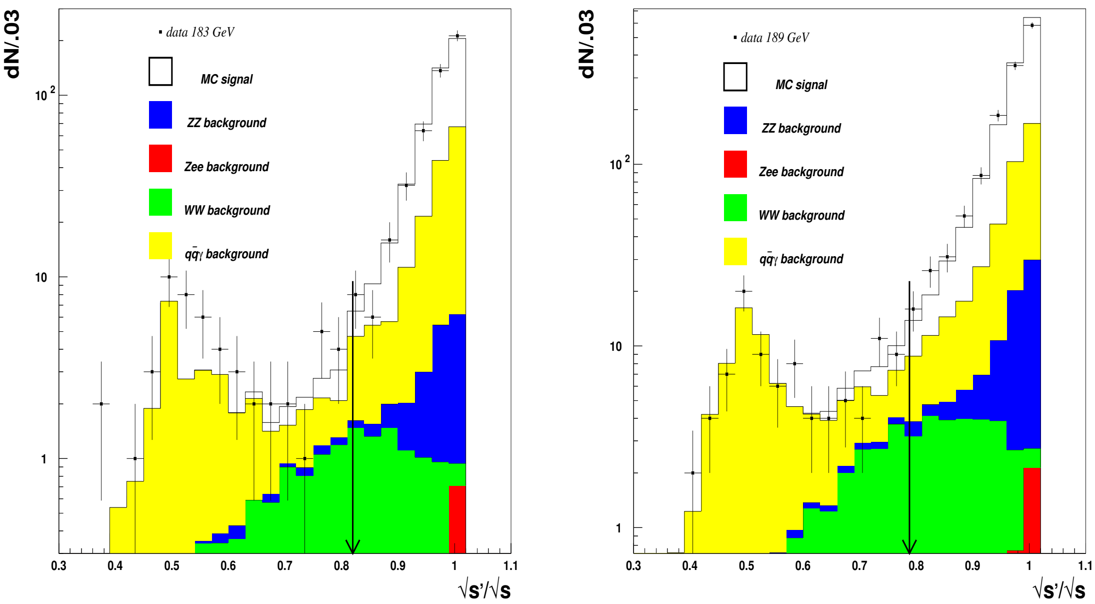

Figure 3.7: *The distribution (on logarithmic scale) of the effective centre-of-mass energy normalised to the centre-of-mass energy of the event after all cuts have been made but the cut on $\sqrt{s'}$, for data (points), signal MC (white area) and background MC (hatched areas). The figure on the left is for the data taken at 183 GeV, the figure at the right is for the data taken at 189 GeV. The arrow indicates the cut.*

Clustering

The Durham algorithm [101, 102] is used to cluster and force the selected charged and neutral particle tracks into four jets. The y_{cut} clusterisation measure (see Section 3.7) is increased until two of these jets are combined, and the event is re-clustered in three jets: the variable is referred to as $y_{cut}4 \to 3$, the value of the variable needed to go from four to three jets. The W^+W^-events decaying into four quarks have four or more natural well spaced jets and hence a high value of $y_{cut}4 \to 3$. The $q\bar{q}$ events typically have two hard jets and other softer jets created by gluon emission. These will recluster at smaller values of $y_{cut}4 \to 3$ than the $q\bar{q}Q\bar{Q}$ events. The distribution of the $y_{cut}4 \to 3$ variable can be seen in Figure 3.8 for the data sets taken at 183 and 189 GeV. No cut on this variable was made as the D variable (see later) is more powerfull and both parameters are completely correlated.

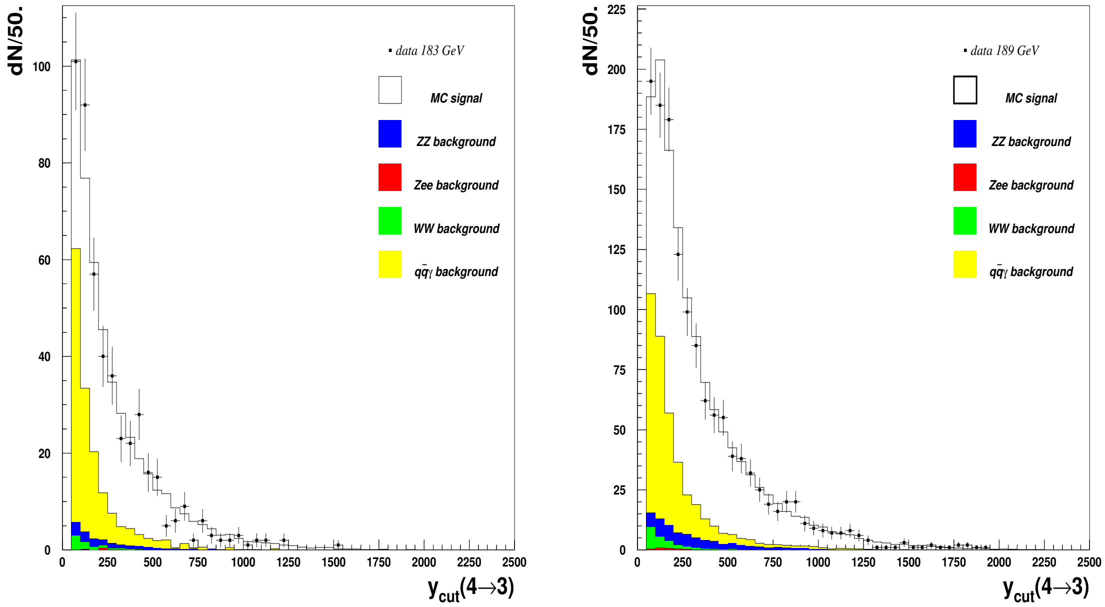

Figure 3.8: *The $y_{cut}4 \to 3$ distribution (in GeV^2) after all cuts have been made, for data (points), signal MC (white area) and background MC (hatched areas). The figure on the left is for the data taken at 183 GeV, the figure at the right is for the data taken at 189 GeV.*

Jet quality

Having clustered all the selected events in a four jet topology we impose a minimum quality on these jets. Jets originating from quark fragmentation are characterised by a large number of tracks (charged and neutral), while softer gluon jets or artificial jets have lower multiplicity. We require the jetmass M_j to be greater than 1 GeV and the number N_{ch+neu} of charged and neutral tracks per jet to be greater than 2 for all jets.

The variable D_{var}

The QCD background which remains after the previous cuts have been made, is very hard to remove. A variable which helps to remove some of this background ($\sim 26\%$) is the variable D_{var}

defined as

$$D_{var} = \theta_{min}^{jet} \times E_{min}^{jet}, \tag{3.5}$$

with θ_{min}^{jet} the minimum interjet angle and E_{min}^{jet} the energy of the jet with the smallest energy. This variable is computed after the 4C fit (see also Section 3.8) has been performed. The distribution of this variable for data taken at the two energies considered is shown in Figure 3.9 and shows the efficiency of the cut on this variable. The following requirements were imposed

$$D_{var} \geq 13 \text{ rad GeV at 183 GeV,}$$
$$D_{var} \geq 15 \text{ rad GeV at 189 GeV.}$$

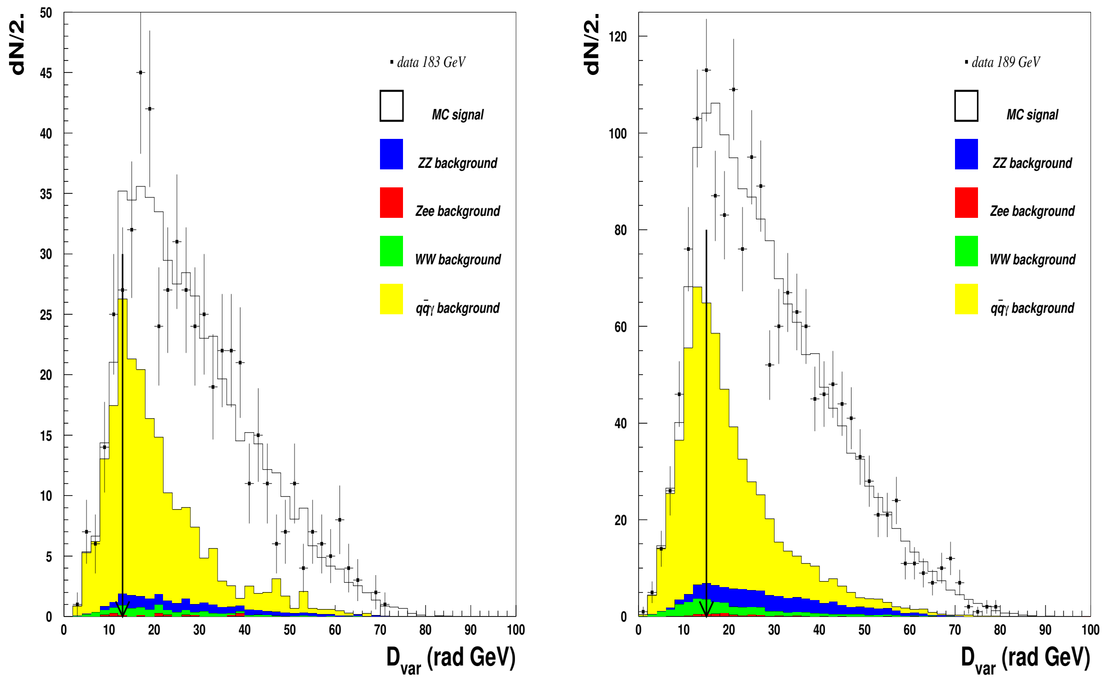

Figure 3.9: *The distribution of the D variable D_{var} after all cuts have been made but the cut on D_{var}, for data (points), signal MC (white area) and background MC (hatched areas). The figure on the left is for the data taken at 183 GeV, the figure at the right is for the data taken at 189 GeV. The arrow indicates the cut.*

Summary

Table 3.3 gives an overview of the performance of the selection criteria we used to discriminate the signal events from the various background processes. All imposed cuts are summarised in Table 3.4. The selection efficiencies in Table 3.3 are calculated using `Pythia` simulation as the fraction of true signal events which survived the selection criteria, over the total number of simulated signal events. A total of 476 events were selected at a centre-of-mass energy of 183 GeV and 1326 events at 189 GeV, which is well in agreement with the number of expected events for the given luminosities of 52.6 pb^{-1} and 154.39 pb^{-1} at these energies respectively. All the distributions of the variables used to select the signal events show agreement between data and

	Units	183 GeV selection	189 GeV selection
Signal selection efficiency	%	85.9 ± .3	82.5 ± .3
σ_{res} $(q\bar{q}\gamma)$	pb	2.58 ± .110	2.00 ± .05
σ_{res} (ZZ)	pb	0.256 ± .008	0.378 ± .009
σ_{res} (non 4j WW)	pb	0.122 ± .007	0.127 ± .005
σ_{res} (Zee)	pb	0.024 ± .008	0.029 ± .003
σ_{res} (total)	pb	2.98 ± .11	2.53 ± .05
Purity	%	67.0 ± 2.0	71.0 ± 2.0
Expected events		475± 6	1357 ± 8
Selected events		476	1326

Table 3.3: *Performance of the hadronic event selection at 183 GeV and at 189 GeV.*

simulation (see figures 3.5 - 3.9).
Table 3.3 also gives cross-sections of the various irreducible background processes after cuts. The expected purity of the final sample is computed with respect to the hadronic WW signal events. The largest fraction of background comes from the $q\bar{q}(\gamma)$ process. This is because this process resembles the signal process $WW \to q\bar{q}Q\bar{Q}$ too much as in some cases each quark radiates an energetic gluon. The other irreducible background is the ZZ process as the two bosons have a mass of $\sim$ 91 GeV and are kinematically close to the signal characterised by two objects of mass close to 80 GeV.

Cross-section estimate
The total cross-section σ_{qqqq} of the fully hadronic channel ($\sigma_{WW} \times BR(q\bar{q}Q\bar{Q})$) can be estimated from the total number N of selected data events. The relation between the total number of selected events N, the total integrated luminosity $\mathcal{L}$, the selection efficiency of the signal ϵ and σ_{BKG}, the background cross-section, is

$$N = (\epsilon\sigma_{qqqq} + \sigma_{BKG}) \times \mathcal{L}. \tag{3.6}$$

The total cross-section has been estimated as

$$\sigma_{qqqq} = 7.05 \pm 0.48 \text{ (stat)} \pm 0.14 \text{ (syst) pb at 183 GeV},$$
$$\sigma_{qqqq} = 7.34 \pm 0.28 \text{ (stat)} \pm 0.09 \text{ (syst) pb at 189 GeV}.$$

The dominant contribution to the systematic error comes from the uncertainty on the background, the other components are due to uncertainties in the efficiency and luminosity. This cross-section

	Cut value
Charged multiplicity N_{ch}	≥ 14
Visible energy E_{vis}	$> 1.15 E_{beam}$
Jet quality $\forall j$ M_j N_{ch+neu}	 ≥ 1 GeV > 2
$\sqrt{s'}$	> 150 GeV
D_{var}	≥ 13 rad GeV at 183 GeV ≥ 15 rad GeV at 189 GeV

Table 3.4: *Overview of the applied cuts for the $q\bar{q}Q\bar{Q}$ selection. The second column gives the cut values for data taken at 183 GeV and at 189 GeV.*

analysis is a good cross check and the obtained results are comparable with the DELPHI published results [92, 97]

$$\sigma_{qqqq} = 7.19 \pm 0.46 \text{ (stat)} \pm 0.13 \text{ (syst) pb at 183 GeV},$$
$$\sigma_{qqqq} = 7.36 \pm 0.26 \text{ (stat)} \pm 0.10 \text{ (syst) pb at 189 GeV}.$$

Although these results are quite similar the analyses differ. The selection criteria used are not the same for both analyses resulting in a larger fraction of the background processes and a different number of selected events for the cross-section analysis presented in this thesis. The systematic error analyses were not performed in the same way. This analysis takes only the uncertainty of the background and efficiency into account while the DELPHI published analysis had a more elaborate study of systematic errors.

Chapter 4

Monte Carlo study of the analysis method

4.1 Introduction

This chapter describes the method used to extract measurements of the different TGC parameters ($\alpha_{W\phi}$, α_W, $\alpha_{B\phi}$) or ($\Delta g_Z^1, \Delta\kappa_\gamma, \lambda_\gamma$) from the total cross-section for the process $e^+e^- \to W^+W^- \to q\bar{q}Q\bar{Q}$ and the distribution of the production angle θ_{W^-} of the W^- with respect to the incoming electron. The advantage of the high branching fraction of the fully hadronic channel is counter balanced by the experimental difficulties associated with the purely hadronic nature of the final state. When both W's decay hadronically the problem arises of selecting the correct pairs of jets corresponding to the two W decays and of assigning the W charges. These problems are tackled in Sections 4.2 and 4.3 respectively.
In the next section we discuss the measurement of the production angle and its dependence on the anomalous couplings. The statistical framework used, the Extended Maximum Likelihood technique is discussed in Section 4.5. In the last two sections a Monte Carlo study of the analysis method used is presented. The description of the analysis at $\sqrt{s}$ = 189 GeV is given first as this analysis is carried out for all the TGC parameters with a larger data sample implying a more precise determination of the anomalous couplings. A complete study at generator and reconstruction level is discussed. In the last paragraph the analysis at $\sqrt{s}$ = 183 GeV is revisited; the properties of the estimator are only checked at reconstruction level.
Only four TGC parameters are determined ($\alpha_{W\phi}$, α_W, $\alpha_{B\phi}$, Δg_Z^1) and not two times three as discussed previously[1]. One can demonstrate that determining α_W is equivalent to determining λ_γ and the analogous $\alpha_{B\phi} = \Delta\kappa_\gamma$ for single parameter fits where we vary one parameter and all others are held at their SM value. Throughout the text α represents one of the four anomalous couplings to be determined.

[1]Three of these four parameters are independent: $\alpha_{W\phi}$, α_W and $\alpha_{B\phi}$; Δg_Z^1 and $\alpha_{W\phi}$ are related (see Equation 1.19).

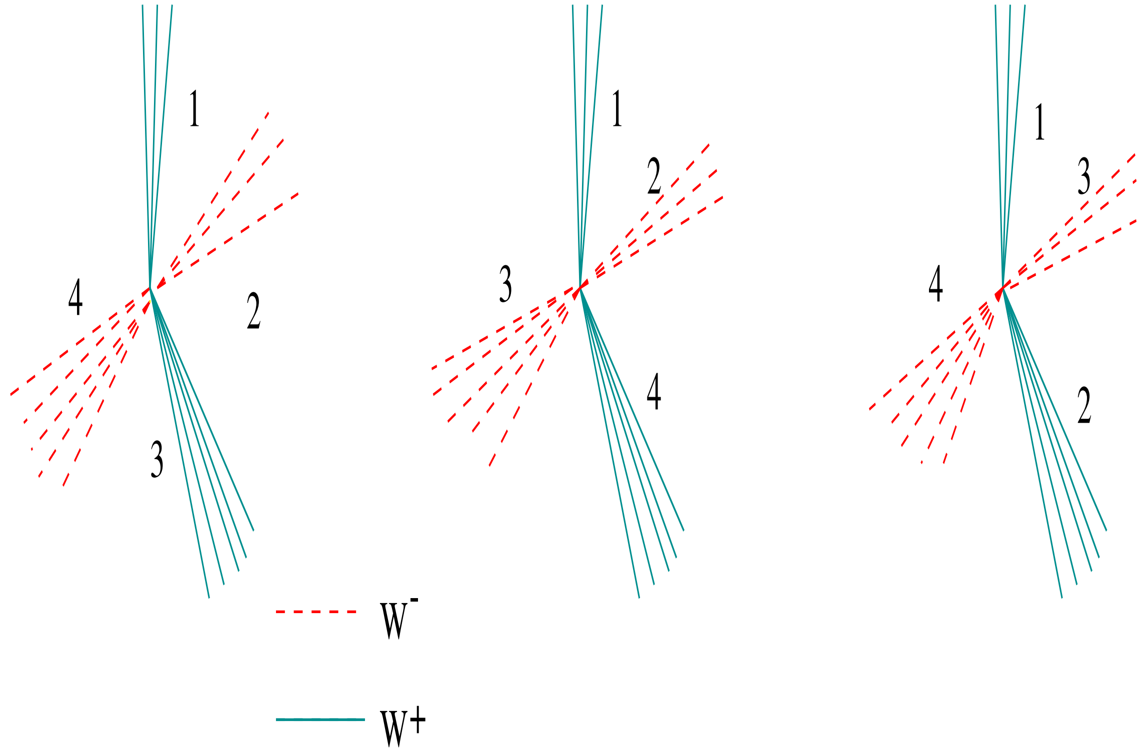

Figure 4.1: *All possibilities to assign jet pairs to the W's.*

4.2 Jet pairing

Once the event is selected and all particles have been assigned to a jet, we are left with a four jet topology for each event. Three possibilities exist to assign a pair of two jets to a W as we can see in Figure 4.1. In this figure the directions of the generated W^- and W^+ boson in an event can be retrieved from the momenta of the particles schematically represented by dashed and full lines respectively. The jets numbered from one to four can be assigned in three ways to either W. These jet pairing combinations will be named (12-34), (13-24) and (14-23). In this section a range of methods is considered for obtaining the correct jet pairing from the possible combinations (see Table 4.1). Amongst these methods of choosing the best pairing of the four jets into two W's are methods based on a kinematic fit. For more details on the kinematic fits we refer to Section 3.8 and references [103, 104]. The efficiencies which are quoted were obtained from simulated events.

The first method tried in this study assumes that the best pairing combination is the one where the mass difference, computed after a 4C fit, between the two jet-jet combinations is the smallest. This method is given the name “mass difference” method. The di-jet mass values obtained after performing a 4C fit are denoted M_{ij}^{4C} and M_{kl}^{4C}.

With the so called “mass method”, the best combination is taken to be the one where the difference in mass, after a 4C kinematic fit, of a two jet combination and a reference value of the W boson mass M_W^{ref} is the smallest. We only take into account one di-jet mass in this method and put no constraint upon the other di-jet mass. In this study the reference mass was taken as the

generated value of M_W for the simulation events. It is clear that this method is biased as we see in Figure 4.2(a). In this figure the invariant mass of the two reconstructed W bosons is plotted. We choose the solution where the mass difference between the combination W_1 and a reference was the smallest, while we did not put any constraints on the mass of W_2. That is why the invariant mass distribution of W_1 resembles more a Breit Wigner than the invariant mass distribution of W_2. In this invariant mass distribution a tail at lower mass values is clearly visible.
In a third method we make the choice of the best jet pairing on the basis of the lowest χ^2 of a 5C kinematic fit where the fifth constraint is the requirement that the two reconstructed jet-jet masses are equal within errors.
Finally, for each of the three pairings a 6C kinematic fit can be made which imposes on top of energy-momentum conservation the equality of the two reconstructed invariant jet-jet masses with a reference mass M_W^{ref} for the W boson. Figure 4.2(b) shows the distribution of the invariant masses of the two W bosons reconstructed with this method. As we see both distributions resemble a Breit Wigner distribution.
The performance of all methods tried in this study was obtained from simulated events and is

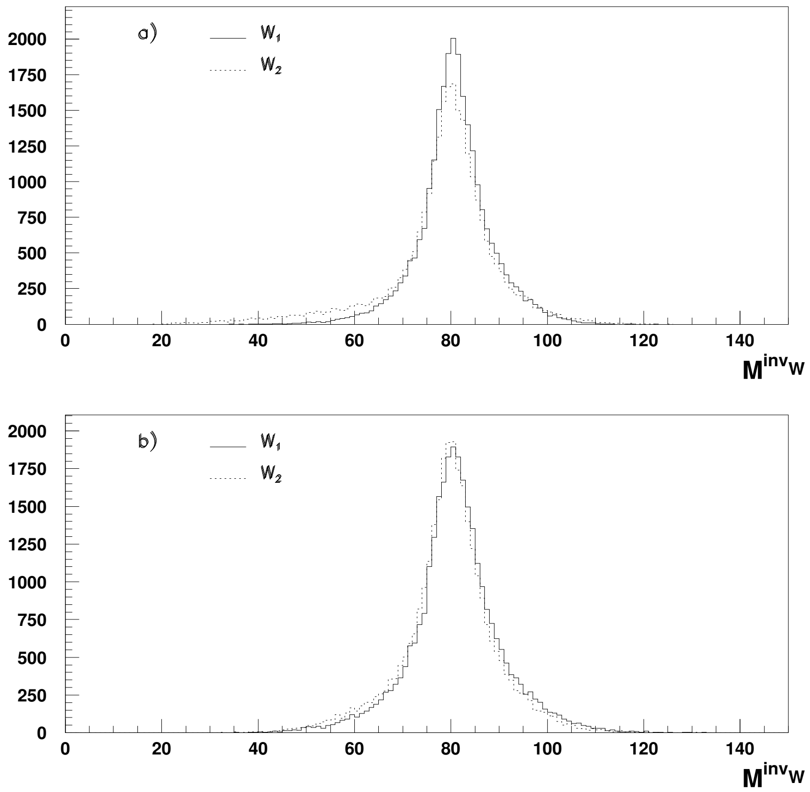

Figure 4.2: *The invariant mass distributions for both reconstructed W bosons in the event: (a) with the mass method and (b) with the 6C kinematic fit.*

shown in Table 4.1. The efficiency gives the rate of events for which the so called best pairing solution (selected with a given method) corresponds to the correct combination for the event. The correct combination for the simulated events was obtained from the reconstructed jet which was

Method	Algorithm used	Efficiency at 183 GeV	Efficiency at 189 GeV
Mass difference	$min\|M^{4C}_{ij} - M^{4C}_{kl}\|$ ij=12, 13 or 14 and kl=34, 24 or 23	$(45.3 \pm 0.4)\%$	$(46.3 \pm 0.2)\%$
Mass	$min\|M^{4C}_{ij} - M^{ref}_{W}\|$ ij=12, 13 or 14	$(62.1 \pm 0.4)\%$	$(63.0 \pm 0.2)\%$
5C kinematic fit	lowest χ^2_{5C}	$(61.3 \pm 0.4)\%$	$(62.4 \pm 0.2)\%$
6C kinematic fit	lowest χ^2_{6C}	$(72.8 \pm 0.3)\%$	$(74.0 \pm 0.2)\%$

Table 4.1: *Jet pairing efficiencies for simulated $q\bar{q}Q\bar{Q}$ events.*

closest to a generated quark or W direction. The figures in Table 4.1 are for `Pythia` MC samples at centre-of-mass energies of 183 GeV and 189 GeV. Similar pairing efficiencies were estimated with simulated `Excalibur` events: $(74.2 \pm 0.4)\%$ at 183 GeV and $(74.8 \pm 1.0)\%$ at 189 GeV for the 6C fit method. No differences in efficiencies were observed for the $q\bar{q}Q\bar{Q}$ samples generated at non-SM TGC parameter values. While for `Pythia` MC events the original W direction is known, for `Excalibur` MC events the W direction was estimated from the quark directions. From the table it is clear that the use of a reference mass can greatly improve the accuracy of the selection. The method which makes use of the 6C kinematic fit was found to perform best and will be further used in this analysis.

4.3 *W* charge assignment

The identification of the W^- and the reconstruction of its production angle is complicated by the absence of a clean charge signature of the W^- which is not the case in the semi-leptonic channel. In order to attempt to resolve the ambiguity on the production angle, a jet charge Q_{jet} can be defined by weighting the charge Q_i of each particle assigned to a jet with its momentum $\vec{p}_i$

$$Q_{jet} = \frac{\sum_{i \in jet} Q_i |\vec{p}_i|^k}{\sum_{i \in jet} |\vec{p}_i|^k}, \tag{4.1}$$

with k a real number. Different algorithms were tried as can be seen from Table 4.2.
It appears to be very difficult to identify the charge of each individual jet. Since the difference between the charges of the two W's is equal to ± 2, one can however distinguish the W^- from the W^+ with a relative high separation efficiency by considering the W charge difference ΔQ. Each W charge is then defined by the sum of the charges of the two jets assigned to it on the basis of a 6C kinematic fit (as we have seen in the previous section), $Q_W = Q_{jet1} + Q_{jet2}$. To estimate the degree of ambiguity in the W charge assignment a probability P^- for a di-jet to arise from a W^-

Jet charge algorithm Q_{jet}=	Performance at $\sqrt{s}$ = 183 GeV	Performance at $\sqrt{s}$ = 189 GeV
$\sum_{i=1,n} Q_i$	$(70.5 \pm 0.6)\%$	$(71.2 \pm 0.4)\%$
$\frac{\sum_{i=1,N} Q_i \lvert\vec{p}_i\rvert}{\sum_{i \in jet} \lvert\vec{p}_i\rvert}$	$(72.9 \pm 0.6)\%$	$(74.3 \pm 0.4)\%$
$\frac{\sum_{i=1,n} Q_i \lvert\vec{p}_i\rvert}{\sum_{i=1,n} \lvert\vec{p}_i\rvert}$	$(73.6 \pm 0.6)\%$	$(74.9 \pm 0.4)\%$
$\frac{\sum_{i=1,N} Q_i \lvert\vec{p}_i\rvert^{1/2}}{\sum_{i \in jet} \lvert\vec{p}_i\rvert^{1/2}}$	$(76.2 \pm 0.5)\%$	$(77.4 \pm 0.3)\%$
$\frac{\sum_{i=1,n} Q_i \lvert\vec{p}_i\rvert^{1/2}}{\sum_{i=1,n} \lvert\vec{p}_i\rvert^{1/2}}$	$(76.0 \pm 0.5)\%$	$(77.0 \pm 0.3)\%$

Table 4.2: *The probability of assigning the negative charge to the W^- in $q\bar{q}Q\bar{Q}$ events, using different variants of the algorithm from Equation 4.1; N is the total number of particles in the jet and n is the number of charged particles in the jet.*

decay was constructed from simulated events. The probability P^- was calculated as a function of the charge difference between the two jet pairs, $\Delta Q = Q_{W_1} - Q_{W_2}$, and is given by

$$P^-(\Delta Q) = \frac{N_-(\Delta Q)}{N_+(\Delta Q) + N_-(\Delta Q)}, \tag{4.2}$$

with N_- the distribution of the charge difference ΔQ between the two W systems where W_1 was the true W^-. In an analogous way N_+ is defined as the distribution of the charge difference ΔQ between the two W systems where W_1 was the true W^+. The probability P^- is only determined for the fraction of events which were correctly paired by the 6C kinematic fit and are also called the good paired events (see previous section). In this way the performance for correct W^- charge determination could be estimated from MC for a given cut on ΔQ.

An overview of the W^- charge assignment performance for the different jet charge algorithms can be found in Table 4.2 for simulated `Pythia` samples at 183 GeV and 189 GeV. In the calculation of these efficiencies the W_1 boson was W^- when $\Delta Q < 0$. One sees that including the neutral particles in the weighted sum of Equation 4.1 does not change the performance of the algorithms significantly. The algorithm using only the sum of the charges was not very performant so it was discarded. This can be explained by the fact that not all charged particles in the jet are detected. The algorithm with $k = 1/2$ with the weighted sum over charged particles only was selected. The efficiency for correct W^- charge assignment was computed to be $\epsilon = (76.0 \pm 0.5)\%$ and $\epsilon = (77.0 \pm 0.3)\%$ for correctly paired hadronic W^+W^- events at centre-of-mass energies of 183 GeV and 189 GeV respectively.

The aim of this performance study was to choose the best jet charge determination algorithm. We do not ascribe a definite charge to each di-jet with a ΔQ cut dependent efficiency for the Extended Maximum Likelihood fits, but rather adopt a weighting procedure with $k = 1/2$ taking

only account of the charged particles, considering both W^- charge solutions with corresponding weights $P^-(\Delta Q)$ and $1 - P^-(\Delta Q)$.
The distribution of Q_{W_1} for $\Delta Q < 0$ ($\Delta Q > 0$) at 183 GeV is shown in Figure 4.3(a) (4.3(b)). The data is well reproduced by the MC simulation. Figure 4.3(c) shows the distribution of the reconstructed charge difference ΔQ between the two W systems as calculated with the charge algorithm for W_1 equal to the true W^- or W^+ respectively, obtained from MC generator information. The distribution of P^-, obtained from MC simulation, is depicted in Figure 4.3(d).
This study was also performed for samples generated at a centre-of-mass energy of 189 GeV and

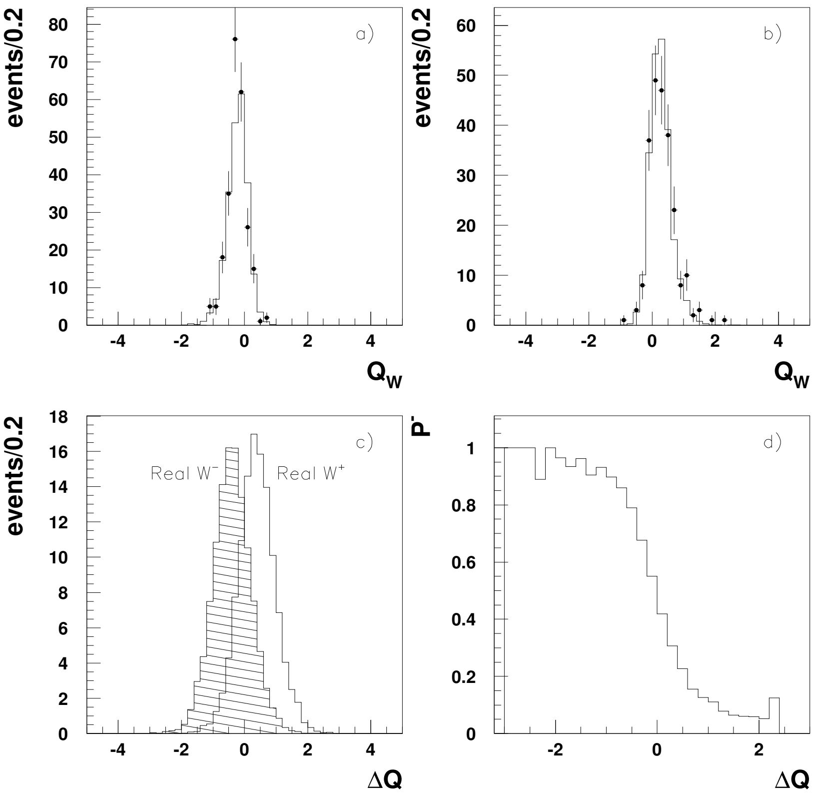

Figure 4.3: *W charge tagging distributions at 183 GeV. (a), (b) Distributions of W^- (selected by $\Delta Q < 0$) and W^+ (selected by $\Delta Q > 0$) reconstructed charges, respectively. The data are represented by dots and the MC by the histograms. The number of MC events is normalised to the integrated luminosity of the data (53 pb^{-1}). (c) The distribution of the charge difference for W_1 equal to the simulated true W^- (hatched) and to the true W^+ boson (white). (d) The probability P^- as function of the charge difference between the two W's.*

the same conclusions can be drawn, as can be seen from Figure 4.4.
No significant difference in performance was found between the `Excalibur` and `Pythia` samples. The efficiency of the chosen jet charge algorithm for the assignment of the negative charge to the W^- obtained from `Excalibur` samples is $(77.6 \pm 0.5)\%$ and $(76.0 \pm 2.0)\%$ at 183 and 189 GeV respectively.

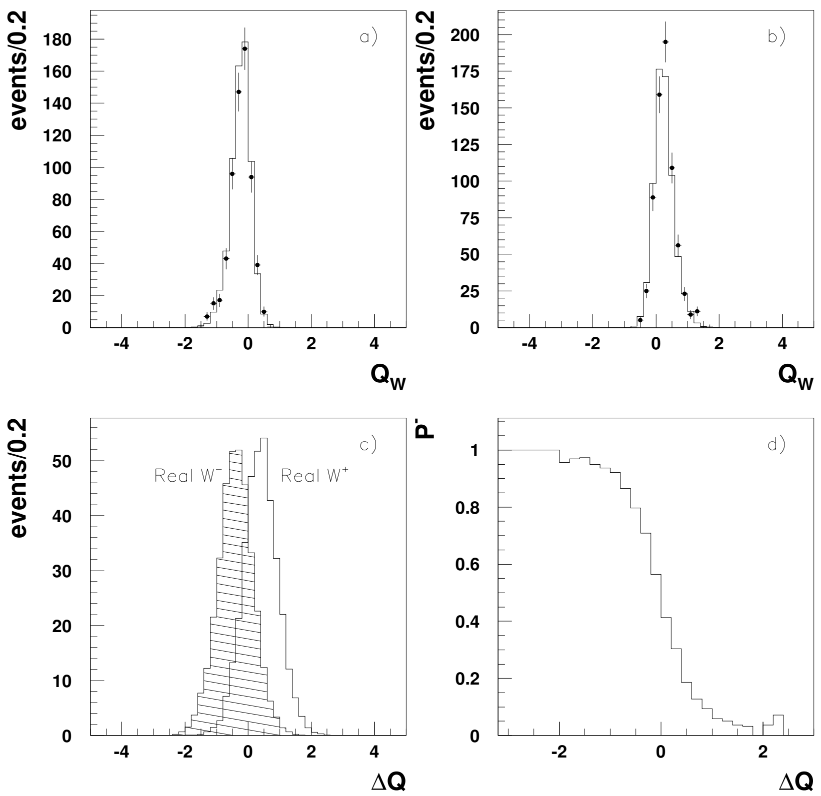

Figure 4.4: *W charge tagging distributions at 189 GeV. (a), (b) Distributions of W^- (selected by $\Delta Q < 0$) and W^+ (selected by $\Delta Q > 0$) reconstructed charges, respectively. The data are represented by dots and the MC by the histograms. The number of MC events is normalised to the integrated luminosity of the data (154 pb^{-1}). (c) The distribution of the charge difference for W_1 equal to the simulated true W^- (hatched) and true W^+ boson (white). (d) The probability P^- as function of the charge difference between the two W's.*

4.4 The *W* production angle

In the previous two sections we have discussed the solutions to tag both jet charge and charge of the W^- boson and have developed an algorithm to decide which jets belong to a given W boson. We will now compute the production angle of the W^- boson in the lab frame and show how this variable depends on the couplings we want to determine.
The production angle θ_{W^-} is defined as the angle between the incoming electron and the outgoing W^-. This is illustrated in Figure 1.4. The production angle is reconstructed from the momenta of the four jets after a 4C kinematic fit has been applied. The reason for applying a 4C kinematic fit is the significant improvement on the angular resolution as can be seen from Figure 3.4 and the correction for the rejected tracks (see Section 3.3 on track selection).
In Figure 4.5 the polar angular distribution of the W_1 boson[2] is depicted for the data and the signal and the background MC. The background, normalised to the data size, includes the following

[2]The W_1 boson is defined in the same way as in the previous sections; it is the first di-jet pair combination (12, 13 or 14) in the event for which a 6C kinematic fit gave the lowest χ^2.

processes: $q\bar{q}(\gamma)$, ZZ, semi-leptonic WW decays and Zee events (as we have seen in Chapter 3). The signal MC is subdivided into two classes: the correctly paired and the incorrectly paired events. For the events in the first class the 6C kinematic fit gave the right pairing solution, while for the events in the second class it did not. Where the incorrectly paired events are uniformly distributed in $cos\theta_{W_1}$, the good paired events have a shape depending on the anomalous couplings to be determined. The background processes ZZ, Zee, the semi-leptonic WW decay channels and the $q\bar{q}(\gamma)$ process however tend to have a non-flat distribution in $\cos\theta_{W_1}$. This is parametrised as such in the fit of the TGC parameters (see further).

An expression for the differential cross-section for W pair production as a function of the W^-

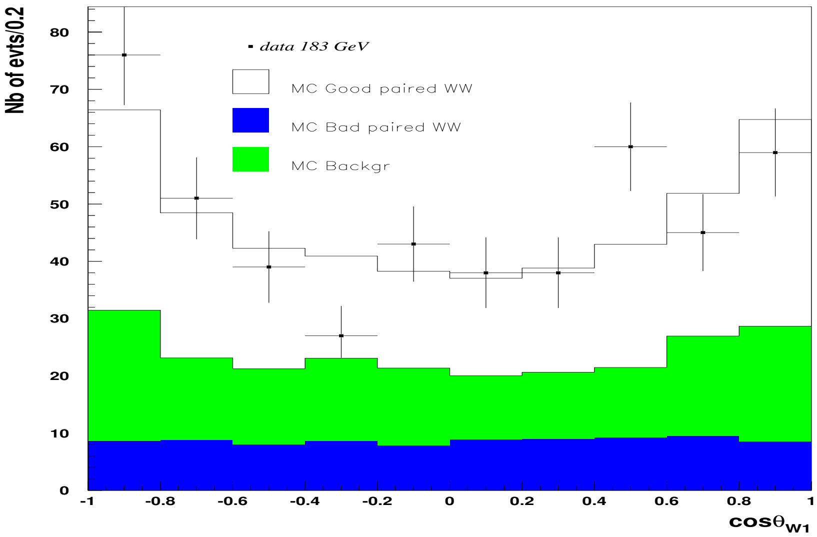

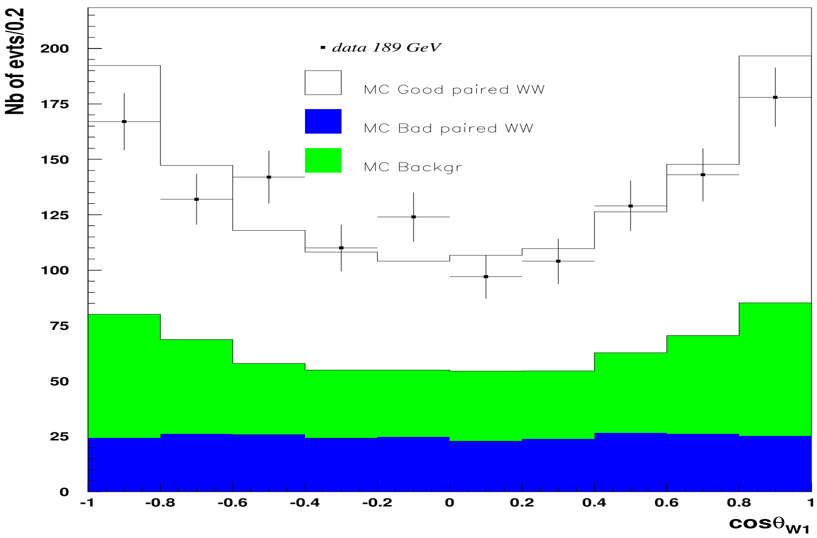

Figure 4.5: *Distribution of the production angle of the W_1. The white histogram represents the MC good paired events, the black and grey histograms represent the badly paired events and the MC background events as indicated. The data are represented by the squares.*

production angle, and depending on the TGC parameters is provided in Equation 1.27. For a deeper discussion on this subject we refer to Chapter 1. Figure 4.6 gives the shape of the differential cross-section computed at a centre-of-mass energy of 183 GeV for different (SM and non-SM) values of each of the four parameters α to be determined, leaving the others at their SM values. From the figure it is clear that the differential cross-section is very sensitive to the TGC coupling parameters $\alpha_{W\phi}$, α_W and Δg_Z^1, but much less sensitive to $\alpha_{B\phi}$.

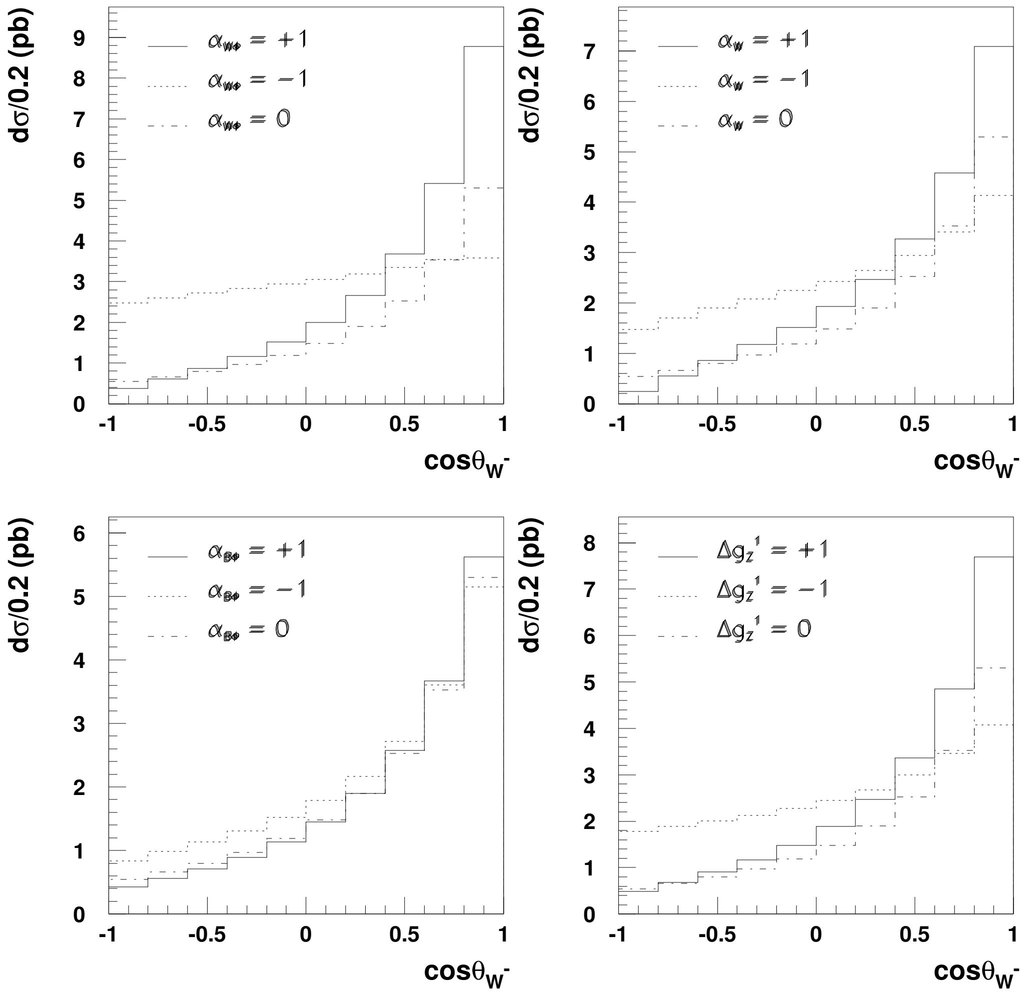

Figure 4.6: *The sensitivity of the W^- production angle distribution for the four different coupling parameters. The calculation has been made with the Bilenky semi-analytic expression [51] at a centre-of-mass energy of 183 GeV.*

4.5 The Extended Maximum Likelihood (EML) procedure

The Maximum Likelihood method is a very powerful tool for determining unknown parameters in physical theories and has been described extensively elsewhere. As it is not the goal of this chapter to give an exhaustive review of this technique the reader is referred to references [106, 107, 108, 109, 110] for more details.

The likelihood method requires a Probability Density Function (PDF) P, which gives the probability that an event described by the observables, Ω, came from a distribution defined by the set of parameters, α. The PDF is normalised to one over the full range of Ω:

$$\int P(\alpha,\Omega)d\Omega = 1, \forall\alpha, \tag{4.3}$$

interpreted as $(P(\alpha)|\Omega)$ it gives the PDF of α. For a set of n events to be fitted a likelihood function, L, is constructed:

$$L(\alpha) = \prod_{i=1}^{n} P(\alpha,\Omega_i), \tag{4.4}$$

where Ω_i is the value of Ω for the i^{th} event. The value of α for which L is maximised is the likelihood estimator for α. In most cases it is convenient to consider the logarithm of the likelihood function

$$\begin{aligned} l &= \ln L, \\ &= \sum_{i=1}^{n} \ln P(\alpha,\Omega_i). \end{aligned}$$

The Extended Maximum Likelihood, abbreviated as EML, is a modification of the maximum likelihood function for the situation where the number of observed events, along with the distribution of observables, depends on α. A new PDF or better an event density, Q, is then normalised to the number of expected events, $N_{exp}(\alpha)$:

$$\int Q(\alpha,\Omega)d\Omega = N_{exp}(\alpha)\int P(\alpha,\Omega)d\Omega = N_{exp}(\alpha), \tag{4.5}$$

instead of being normalised to 1. Using the Poisonian probability of observing n events when $N_{exp}(\alpha)$ were expected one obtains the expression (up to an irrelevant constant):

$$\ln L_{EML} = \sum_{i=1}^{n} \ln(Q(\alpha,\Omega_i)) - \mathcal{L}\sigma(\alpha), \tag{4.6}$$

$$Q(\alpha,\Omega_i) = \mathcal{L}\frac{d\sigma}{d\Omega}(\alpha,\Omega_i), \tag{4.7}$$

and $\frac{d\sigma}{d\Omega}(\alpha,\Omega)$ is the differential cross-section and $\mathcal{L}$ is the integrated luminosity.

One of the most serious drawbacks of the likelihood method is the amount of computation it generally requires. This arises because the method involves a maximisation. Fortunately good software packages have been written to do this. In the analysis presented in this thesis the `Minuit` [111] program was used. The program is written to search the minimum of the function $-\ln L_{EML}$, instead of the maximum of expression used in Equation 4.6.

In cases where the likelihood function L is Gaussian (implying that the logarithm of the likelihood function is parabolic) the error on the likelihood estimator σ_α can be estimated as

$$l(\alpha_0 \pm \sigma_\alpha) = l(\alpha_0) - \frac{1}{2}, \tag{4.8}$$

with α_0 the value of the parameter which maximizes the likelihood function. When the likelihood distribution is not Gaussian we can use the definition of Equation 4.8 above to find two values α_1 and α_2 such that

$$l(\alpha_i) = l(\alpha_0) - \frac{1}{2}, \text{with i} = 1 \text{ or } 2. \tag{4.9}$$

Then the range

$$\alpha_1 \leq \alpha \leq \alpha_2 \tag{4.10}$$

still has the property that the probability that it contains the true value of the parameter is 68$\%$.

4.5.1 Efficiency, consistency and bias of the estimator

Before we move on to the fitting of the data we first need to understand the measurements in terms of expected precision and accuracy. Furthermore we have to verify whether our likelihood estimator fulfills the three qualities of a "good" estimator. The likelihood estimators have to be checked for biases, this means that the estimator can be called **unbiased** if its expectation value is equal to the parameters "true" value. The estimator has to be **consistent**, which means that the bias will vanish for large samples. We call the estimator **efficient** if its variance is small.

A serious drawback of the Maximum Likelihood technique is that there exists no direct method to decide whether the fit was "good" such as we have in the method of least squares. To verify the "goodness of fit" and check the bias and efficiency of the likelihood estimator we apply the same fit as we will use for the data to a large series of MC experiments of size equal to the data. In this way we obtain a value of the estimator α_{FIT} and its error $\sigma_{\alpha_{FIT}}$ for each of the experiments, while we know the true value of the parameter to be fitted. We then compute the pull for each experiment defined as

$$\frac{\alpha_{FIT} - \alpha_{TRUE}}{\sigma_{\alpha_{FIT}}}. \tag{4.11}$$

The distribution of the pull values for a large series of MC experiments should be a Gaussian with mean zero and standard deviation one if the likelihood function is unbiased and if the error on the fitted value is correctly estimated. If the width of the distribution is smaller than one it means the error has been overestimated, and a width larger than one implies that the error on the fitted parameter has been underestimated. This method requires a large amount of MC which in general does not exist (see Table 3.1). To perform these kinds of tests it is necessary to "reshuffle" the available MC events, which means we randomly pick out events of a large MC sample and put them together in samples of the size of the data.

4.5.2 Estimation of the number of events

For WW decays both the cross-section and the angular distributions of the W's are sensitive to the values of the TGC parameters as we have seen in Sections 1.5.1, 1.5.2 and 4.4. This is exploited in the EML principle where we make both use of the shape of the angular distribution and of the total cross-section. The PDF in the EML is normalised to the number of observed events as we have seen in Section 4.5.

The total W pair production cross-section is quadratic in the parameters α, as the matrix element for WW production is linear in these parameters. The parabolic dependence of the total cross-section is not identical for the four parameters as can be seen from Figure 4.7. In this figure the

total cross-section for fully hadronic events is plotted, calculated with the Bilenky [51] expression, as a function of the four TGC parameters at a centre-of-mass energy of 189 GeV.
The `Excalibur` generator enables calculation of the W pair production cross-section for dif-

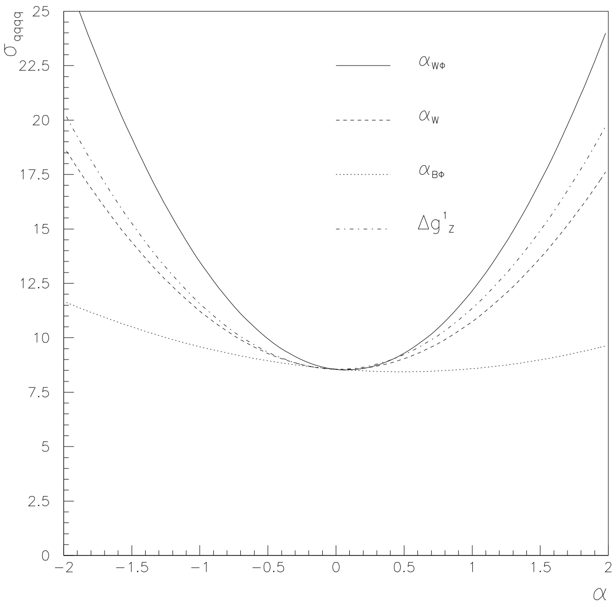

Figure 4.7: *The total cross-section for the fully hadronic channel as function of the four TGC parameters at 189 GeV.*

ferent values of the anomalous coupling parameters. Doing this for three different values of α and assuming the above quadratic behaviour, one can fit a parabola through these three points. When we do this for the total W pair production cross-section at 183 GeV we obtain the curves in figures 4.8 represented by the dashed line. The full line in these figures represents the Bilenky cross-section calculation for these TGC parameters. The difference between the Bilenky and `Excalibur` parametrisation is mainly due to the absence of ISR in the Bilenky semi-analytic expression. These quadratic `Excalibur` parametrisation expressions will be used in Sections 4.6 and 4.7 where the EML fits are performed.

4.6 The extraction of the TGC parameters at 189 GeV

In this section the analysis is presented as it was carried out for the data taken at a centre-of-mass energy of 189 GeV. In the first section (Section 4.6.1) the EML fit is performed on MC samples and tested extensively at generator level. In the last section these tests are repeated for the EML fit but this time at reconstruction level.

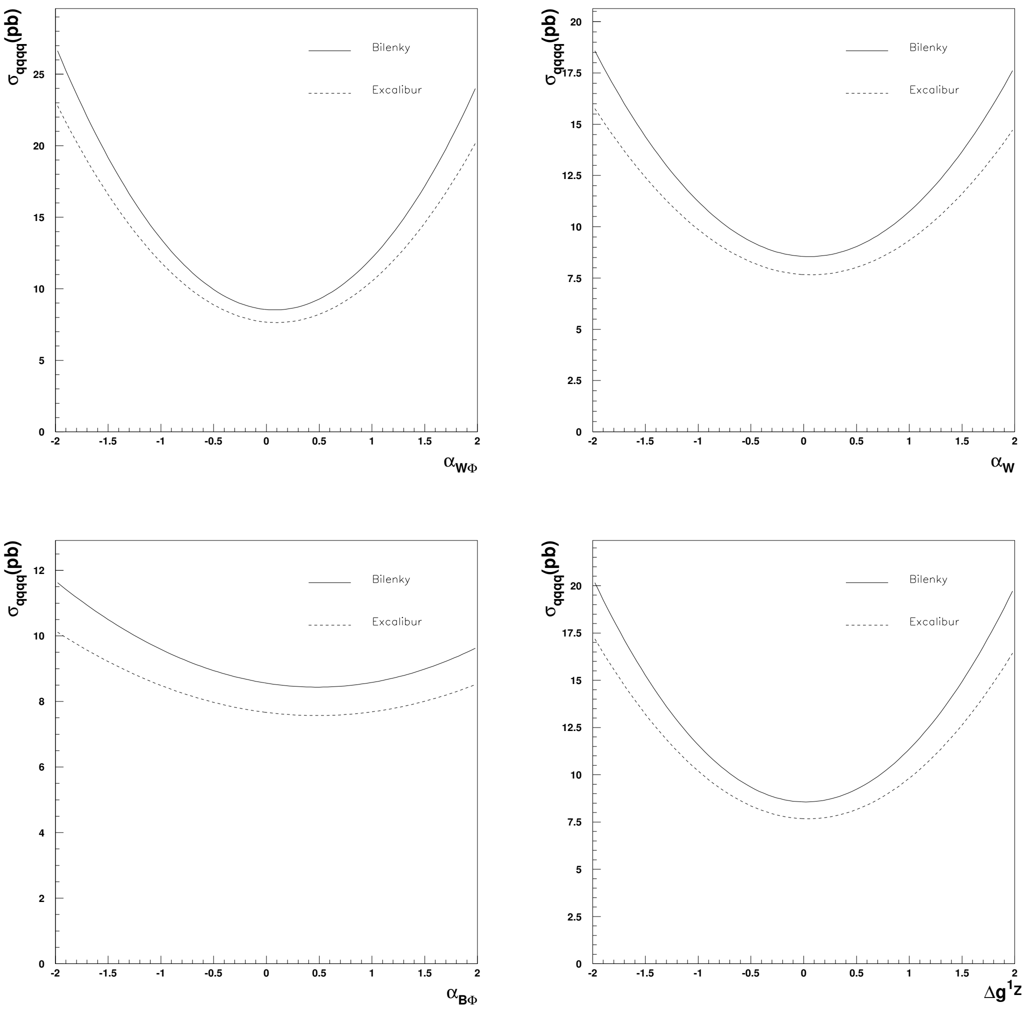

Figure 4.8: *The cross-section for the fully hadronic channel at 183 GeV as function of the TGC parameters. The full line represents the Bilenky parametrisation, the dashed curve the* `Excalibur` *calculation.*

4.6.1 The EML fit at generator level

The EML fit was performed to extract the TGC parameters from MC samples at generator level, which means that only pure physics effects are considered as the detector effects play no role. The production angle can be correctly estimated, and will be referred to as the true production angle $\cos\theta_T$ as it is determined from the quark four-momenta.
The EML for n signal events at generator level makes use of Equation 4.6:

$$\ln L_{EML} = \sum_{i=1}^{n} \ln(\mathcal{L}C_{ISR}C\frac{d\sigma^{BIL}}{d\cos\theta_T}(\alpha, \cos\theta_{T_i})) - \mathcal{L}\sigma^{EXC}(\alpha), \tag{4.12}$$

with σ^{EXC} the $q\bar{q}Q\bar{Q}$ production cross-section evaluated with the `Excalibur` generator (see also Section 4.5.2), $\mathcal{L}$ the integrated luminosity and $\frac{d\sigma^{BIL}}{d\cos\theta_T}$ the semi-analytical expression in zero width approximation computed by Bilenky [51], multiplied by a correction factor C

$$C = \frac{\sigma^{EXC}(\alpha)}{\int_{-1}^{+1} C_{ISR}(\cos\theta_T)\frac{d\sigma^{BIL}}{d\cos\theta_T}(\alpha,\cos\theta_T))d\cos\theta_T}, \tag{4.13}$$

to correct for the lack of Initial State Radiation (ISR) in the Bilenky expression and assure a proper normalisation. The ISR correction factor C_{ISR}, depending on $\cos\theta_W$, is obtained from the ratio of the `Pythia` cross-section over the Bilenky cross-section from Figure 4.9 for all $q\bar{q}Q\bar{Q}$ events. This figure shows the ratio, in bins of $\cos\theta_{W^-}$ (the production angle of the W^-), of the cross-section as calculated with the `Pythia` generator over the cross-section as predicted with the Bilenky model. The latter has no ISR effects included, as was already remarked in the comparison of total cross-sections (see Section 4.5.2). The figure on the left is for simulated $q\bar{q}Q\bar{Q}$ events at a centre-of-mass energy of 183 GeV, while the one on the right is for simulated $q\bar{q}Q\bar{Q}$ events at 189 GeV. The `Pythia` events are divided in two sub-categories as indicated by the caption. To distinguish the $q\bar{q}Q\bar{Q}$ events with ISR from those without, a cut was made on the true centre-of-mass energies

$$E_{\mathrm{CM}}^{\mathrm{true}} > 0.99(2\times E_{Beam}) \text{ for events without ISR,}$$
$$E_{\mathrm{CM}}^{\mathrm{true}} \leq 0.99(2\times E_{Beam}) \text{ for events with ISR,}$$

with $E_{\mathrm{CM}}^{\mathrm{true}}$ the true centre-of-mass energy calculated out of the four-momenta of the four quarks. In this way the fraction of events with ISR was estimated to be 18% at 183 GeV and 20% at 189 GeV. The cross-section ratio was calculated for each sub-category. As can be clearly seen from the figure the ratio is flat in $\cos\theta_W$ for `Pythia` events without ISR and the structure (for low values of $\cos\theta$) present in the distribution for all $q\bar{q}Q\bar{Q}$ events clearly comes from the fraction of events with ISR. This effect is however less pronounced for the data at 183 GeV than it is for the data at 189 GeV. An ISR correction function as a function of $\cos\theta_{W^-}$ was included in the analysis.

Not correcting the fit for this ISR effect provokes a bias as can be seen in Figure 4.10. The distributions on the left represent the Δg_Z^1 fit results for 500 SM MC samples each of data size at a centre-of-mass energy of 189 GeV. The fit was performed at generator level: the quark four-momenta were used to obtain the production angle of the W^-. On the right of Figure 4.10 the pull distributions are shown. The top line shows the results when no ISR correction function is included in the fit, while the results on the bottom line are obtained for an EML fit function with ISR effects included. It is clear that the fit results shown in the Figures 4.10(a) are biased and that this effect disappears when the ISR correction is included as is shown in Figures 4.10(b).

The first verification of the fitting procedure is made by applying the fit to 500 simulated `Pythia` samples of 150 pb^{-1} for each of the four TGC parameters allowing only one parameter to deviate from its Standard Model value of zero. In Figure 4.11 the distributions of the fit results for α (1st column), the error on α (2nd column) and the pulls (3rd column) are shown. No bias is observed for $\alpha_{W\phi}$, α_W and Δg_Z^1, while for $\alpha_{B\phi}$ a few percent of the samples tends to populate a peak at positive values. The pull distributions are all nicely Gaussian distributed around zero with a width equal to one except for $\alpha_{B\phi}$ which has a somewhat smaller width of 0.87 ± 0.03. Hence the error will be slightly overestimated.

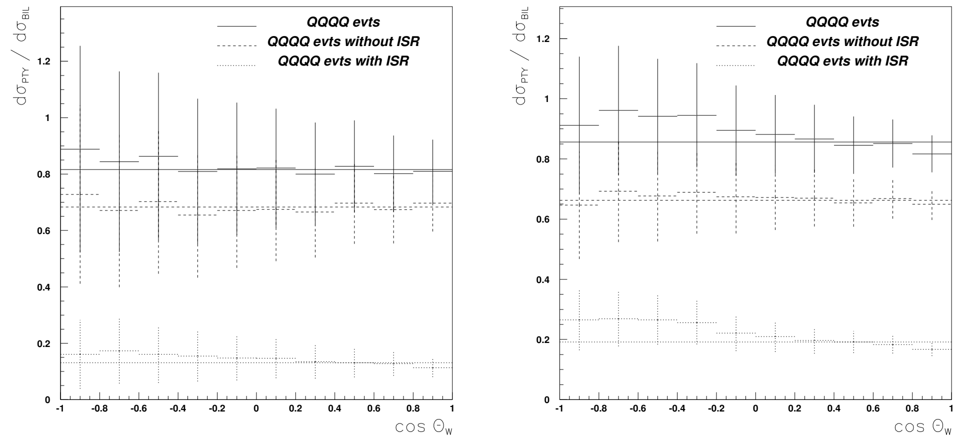

Figure 4.9: *The effects of Initial State Radiation on the differential angular distribution for simulated events at 183 GeV (left) and at 189 GeV (right). The ratio of the total sample of $q\bar{q}Q\bar{Q}$ events over the total Bilenky differential cross-section is represented by the full line, while the ratios for the two sub-samples with and without ISR are shown in dotted and dashed lines respectively.*

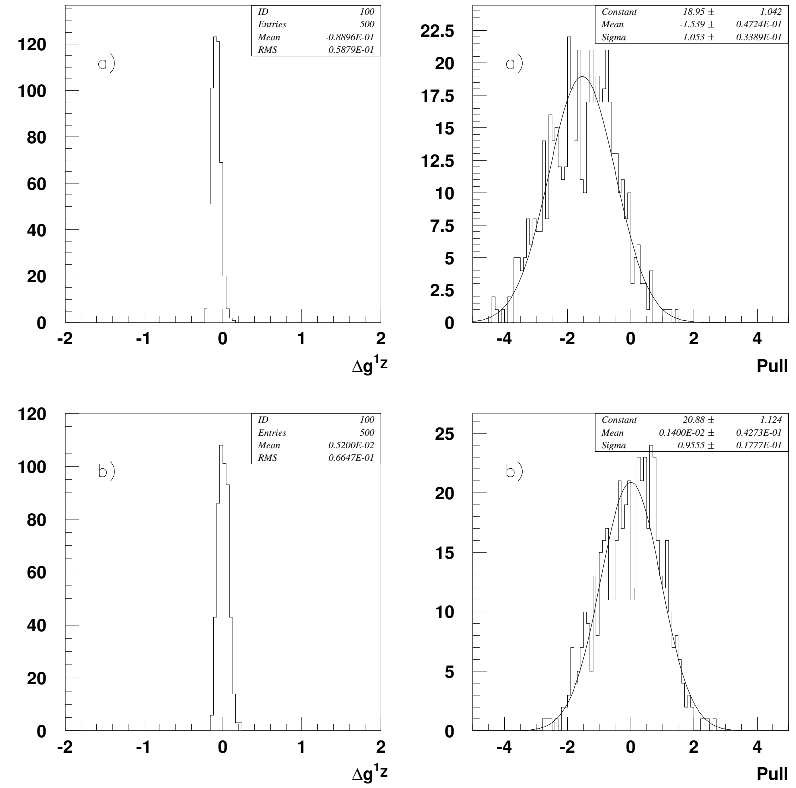

Figure 4.10: *The effects of Initial State Radiation on the fit results at 189 GeV. The fit was performed to 500 MC samples each of data size with an EML fit function without (a) and with (b) ISR effects included.*

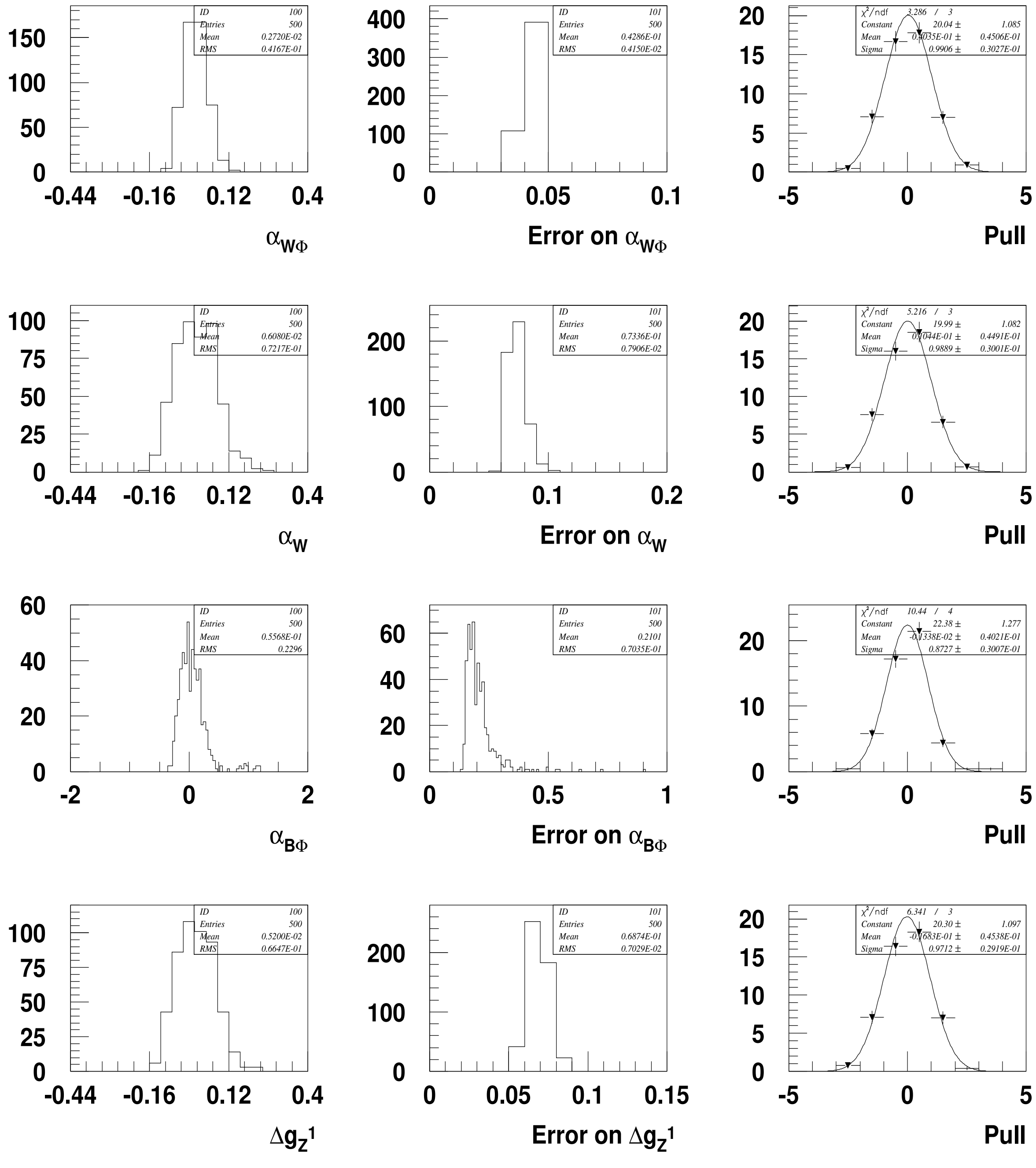

Figure 4.11: *Distributions of the fitted values, the associated statistical errors and the pulls for the four TGC parameters $\alpha_{W\phi}$, α_W, $\alpha_{B\phi}$ and Δg_Z^1 for the fit at generator level at a centre-of-mass energy of 189 GeV performed with 500 MC samples of 150 pb^{-1} equivalent integrated luminosity.*

To verify the consistency and bias of the estimator the fit was also applied to a large `Pythia` MC sample (about 40 times the data size) with all TGC parameters at their SM values and to smaller (about the data size) `Excalibur` samples with and without anomalous couplings. The results of the fitted parameter values can be found in Table 4.3 in the fifth column. All parameters are found to be within one or two standard deviations at most from the generated values, except for the non-SM sample where $\alpha_{B\phi}$ was generated at a value of +1, where we have a loss in sensitivity. In Figure 4.12 (in the left column) the anomalous parameters obtained from a fit at generator level

Generator	Coupling	gen. value	$\mathcal{L}(\mathrm{pb}^{-1})$	fit. value (from true level)	fit. value (from rec. level)
`Pythia`	$\alpha_{W\phi}$	0.	6535.	$0.004^{+.006}_{-.006}$	$0.061^{+.017}_{-.016}$
`Excalibur`		0.	206.	$0.007^{+.039}_{-.038}$	$0.073^{+.087}_{-.078}$
`Pythia`	α_W	0.	6535.	$0.005^{+.011}_{-.011}$	$0.13^{+.035}_{-.034}$
`Excalibur`		0.	206.	$0.018^{+.073}_{-.067}$	$0.090^{+.134}_{-.122}$
		-0.5	168.	$-0.49^{+.050}_{-.049}$	$-0.469^{+.077}_{-.072}$
		+0.5	193.	$0.626^{+.076}_{-.086}$	$0.385^{+.133}_{-.240}$
`Pythia`	$\alpha_{B\phi}$	0.	6535.	$0.035^{+.029}_{-.029}$	$0.305^{+.160}_{-.098}$
`Excalibur`		0.	206.	$-0.059^{+.185}_{-.157}$	$0.453^{+.426}_{-.353}$
		$-1.$	182.	$-0.958^{+.105}_{-.102}$	$-0.564^{+.192}_{-.168}$
		+1.	203.	$1.53^{+.150}_{-.180}$	$0.996^{+.283}_{-.518}$
`Pythia`	Δg_Z^1	0.	6535.	$0.005^{+.010}_{-.010}$	$0.084^{+.026}_{-.025}$
`Excalibur`		0.	206.	$0.022^{+.072}_{-.064}$	$0.070^{+.116}_{-.108}$
		-0.5	186.	$-0.498^{+.043}_{-.042}$	$-0.469^{+.067}_{-.062}$
		+0.5	190.	$0.626^{+.062}_{-.069}$	$0.408^{+.091}_{-.108}$

Table 4.3: *Results of the consistency tests at generator and reconstruction level for MC data at a centre-of-mass energy of 189 GeV. True level (reconstruction) refers to fits performed using generated (reconstructed) four-momenta.*

to the different `Excalibur` $q\bar{q}Q\bar{Q}$ samples are shown as a function of their original true values. A linear fit was performed to each of these figures. If the fit were unbiased the slope and offset along the y axis would be respectively one and zero. This is what is observed within 2.5 standard deviations at most.

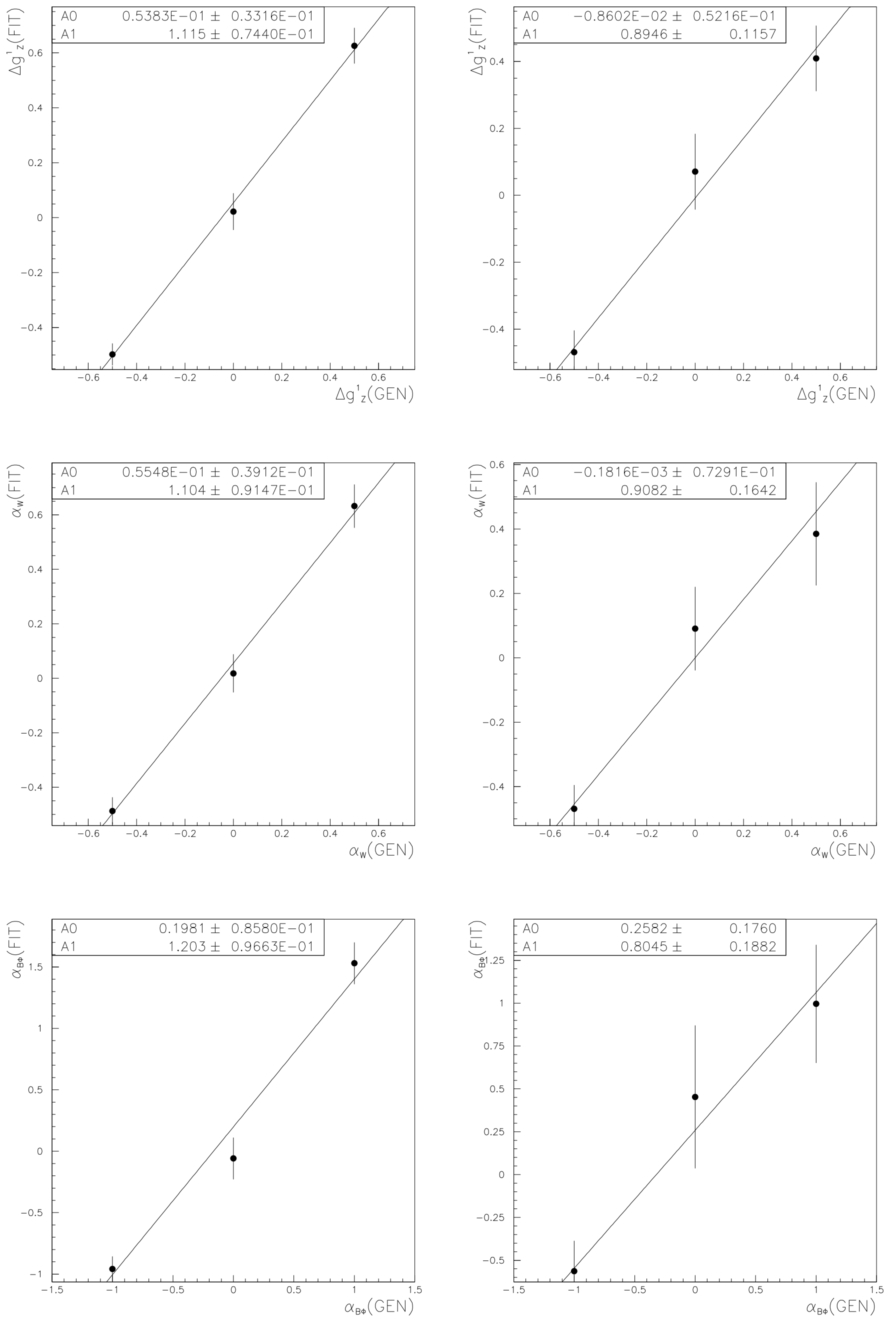

Figure 4.12: *Bias of the estimator for signal events at $\sqrt{s}$ = 189 GeV for generator level kinematic information (left) and for reconstruction level kinematic information (right). The reconstructed parameters are labeled 'FIT' and the true parameter values labeled 'GEN'.*

4.6.2 At reconstruction level

We will now assemble the likelihood function for reconstructed events where the production angle of the W^- is obtained from the reconstructed four-momenta. In the previous section the fit was performed in an ideal case but we now have to take into account other effects such as the imperfection in reconstruction and detection of particles, resolution on the production angle and presence of background processes, ambiguity in the charge and pairing of the W bosons, etc. These have all been estimated in previous sections.
The kinematic information Ω entering into the fit is the production angle of the W^-. The probability, Q, to observe an event takes into account the probability to observe a signal event (consisting of the good paired (GP) and the badly paired (BP) events) and a background (BKG) event:

$$Q(\alpha,\Omega) = Q_{SIG}(\alpha,\Omega) + Q_{BKG}(\alpha,\Omega), \tag{4.14}$$
$$Q_{SIG}(\alpha,\Omega) = Q_{GP}(\alpha,\Omega) + Q_{BP}(\alpha,\Omega). \tag{4.15}$$

The expected density of observed good paired WW event, Q_{GP}, with a measured production angle $\cos\theta_R$ given a true production angle $\cos\theta_T$, is given for an integrated luminosity $\mathcal{L}$ by:

$$\begin{aligned}
&Q_{GP}(\alpha,\cos\theta_R) = \\
&\quad \mathcal{L}\epsilon_S\epsilon_P C \times \\
&\quad \Big[P^-(\Delta Q)\int_{\cos\theta_R-3\sigma'}^{\cos\theta_R+3\sigma'} R(\cos\theta_T,\cos\theta_R)C_{ISR}(\cos\theta_T)\frac{d\sigma^{BIL}}{d\cos\theta_T}(\alpha,\cos\theta_T)d\cos\theta_T \\
&\quad +(1-P^-(\Delta Q))\int_{-\cos\theta_R-3\sigma'}^{-\cos\theta_R+3\sigma'} R(\cos\theta_T,-\cos\theta_R)C_{ISR}(\cos\theta_T)\frac{d\sigma^{BIL}}{d\cos\theta_T}(\alpha,\cos\theta_T)d\cos\theta_T\Big],
\end{aligned} \tag{4.16}$$

with C the correction factor as defined in Equation 4.13 and corrected for ISR effects. The set of parameters to be fitted, α, is in this case just one of the four parameters as defined before. The signal selection efficiency ϵ_S was estimated to be $(82.5 \pm 0.3)\%$ (see Table 3.3). The pairing efficiency $\epsilon_P = (74.0 \pm 0.2)\%$ and the probability $P^-(\Delta Q)$ that the observed W has a negative charge were discussed in Sections 4.2 and 4.3 respectively. The differential cross-section $\frac{d\sigma^{BIL}}{d\Omega}$ is a semi-analytical expression computed by Bilenky [51] introduced in the previous section.
The resolution function R, evaluated as a sum of two Gaussian functions, is depicted in Figure 4.13. The tails in the resolution function can be described with a Gaussian distribution with width σ_2 equal to 0.12, while a more narrow Gaussian (width σ_1 equal to 0.027) describes the events with higher resolution. After normalisation the resolution function $R(\cos\theta_T,\cos\theta_R)$ can be described by a Gaussian function with a width $\sigma' \approx 0.06$ which is used in Equation 4.16.
For certain values of the measured production angle the resolution function will yield a value for $|\cos\theta_T| > 1$, which is unphysical. An example of this situation can be seen in Figure 4.14 where a resolution function R (represented by the dashed/dotted line) with width of 0.2 (the width is chosen this large to illustrate the effect we want to point out) is drawn around a measured value of $\cos\theta_{W^-} = -0.9$. At a certain point the resolution function crosses the physical limit of -1. To overcome this we define a new resolution function called the edge function by taking the mirror image of the resolution function R beyond this physical limit (dotted line in the figure) and add this to the resolution function within the physical limit. The new function is drawn in the figure as a full line.

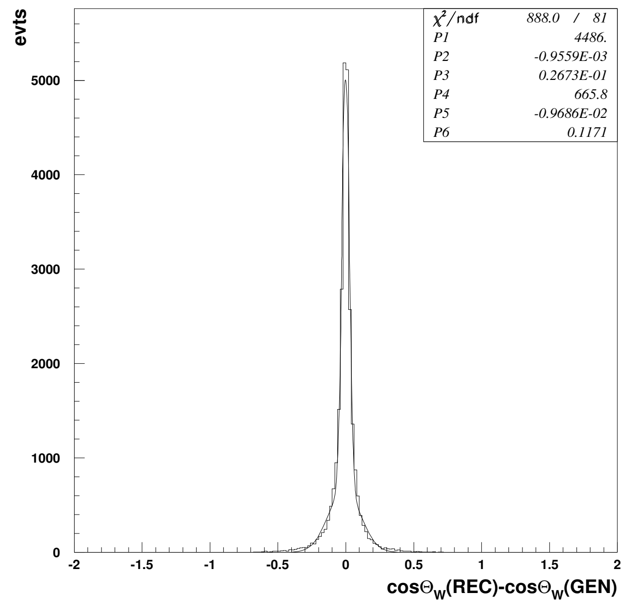

Figure 4.13: *Resolution of the cosine of the production angle at $\sqrt{s}$ = 189 GeV.*

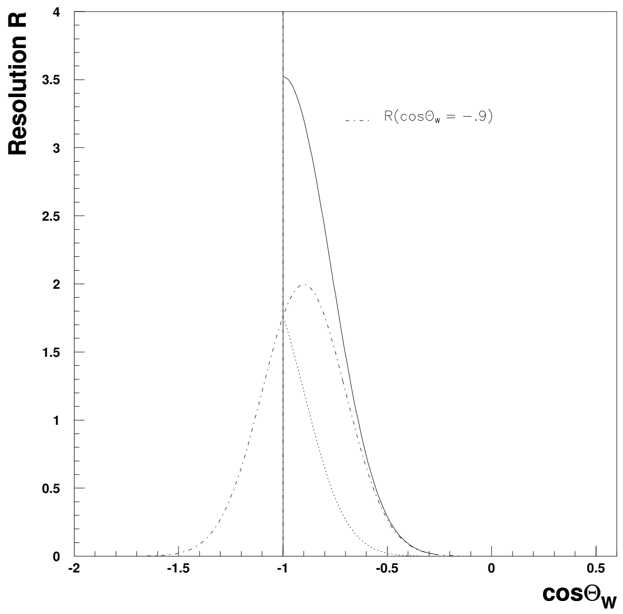

Figure 4.14: *The edge function.*

The probability to observe a badly paired event at a given angle is given by:

$$Q_{BP}(\alpha, \Omega) = \mathcal{L}\epsilon_S(1-\epsilon_P)\frac{d\sigma}{d\Omega}^{BP}(\alpha, \Omega). \tag{4.17}$$

As shown in Figure 4.5 $\frac{d\sigma}{d\Omega}^{BP}(\alpha, \Omega)$ can be taken as a flat distribution:

$$\frac{d\sigma}{d\Omega}^{BP}(\alpha, \Omega) = \frac{\sigma^{EXC}(\alpha)}{2}, \tag{4.18}$$

where the total $q\overline{q}Q\overline{Q}$ cross-section $\sigma^{EXC}(\alpha)$ is coming from an `Excalibur` parabolic parametrisation of the cross-section in α (see Section 4.5.2).
If the background is also taken into account the EML of Equation 4.6 then modifies as follows:

$$\ln L_{EML} = \sum_{i=1}^{n} \ln(Q_{SIG}(\alpha, \Omega_i) + Q_{BKG}(\Omega_i)) - \mathcal{L}(\sigma(\alpha) + \sigma_{BKG}). \tag{4.19}$$

The probability to observe a background event can be derived from:

$$Q_{BKG} = \mathcal{L}\frac{d\sigma_{BKG}}{d\Omega}(\Omega). \tag{4.20}$$

This distribution is not flat in Ω as can be seen from Figure 4.5. The dependence on $\cos\theta_R$ of the differential cross-section for the background processes (ZZ, $q\bar{q}(\gamma)$, other non fully hadronic WW and the small fraction of Zee processes) was estimated from `Pythia` MC events, as was σ_{BKG}, the total expected background cross-section.
The fit procedure has been verified at different stages in the reconstruction process for the four parameters. In the next paragraphs we will go through these different stages for one parameter: Δg_Z^1.
The distributions of the fitted values of the TGC parameter Δg_Z^1, the error on this fitted value and the pull distribution for 250 SM `Pythia` MC samples each corresponding to an integrated luminosity of 150 pb^{-1} are depicted in Figure 4.15 on each line. The first line shows the results in the case where the fit was performed to the fraction of good paired signal events only. We observe that the fitted values of Δg_Z^1 are distributed around zero, with a spread not larger than the average error on the fitted parameter, which indicates that the variance is small. Hence the estimator is efficient. All this results in a pull distribution which is nicely Gaussian distributed with $\sigma \sim 1$.
On the next line the same distributions are shown but the parameter fit is now performed to samples containing also the badly paired events. The last line shows the results obtained for a parameter fit to samples where all background processes have been included on top of the signal $q\bar{q}Q\bar{Q}$ events. The distribution of the fitted values Δg_Z^1 is also centered around zero for all these levels in the reconstruction process. No bias is observed and the average spread is not larger than the average error on the fitted parameter. We can conclude that the estimator is efficient.
The pull distributions in Figure 4.15 are all Gaussian centered around zero, so the estimator for Δg_Z^1 can be called unbiased and we can state that the expected errors are slightly overestimated. The pull distributions for the other three parameters α_W, $\alpha_{B\phi}$ and $\alpha_{W\phi}$ are depicted in Figure 4.16. All parameters are compatible with a Gaussian distribution of unit width and centered around zero. A bias is seen for $\alpha_{B\phi}$, on which is commented later.

Worth remarking as well is the loss of sensitivity for the obtained parameters when going from a fit to a sample without background processes to a fit to a sample with background processes. The effect on the average expected error for the four parameters when we include the background processes can be seen in Table 4.4. The average error increases by about 15% because the quite large $q\bar{q}(\gamma)$ contamination dilutes the precision. This background process was estimated in the previous chapter to be 2.0 pb or 23% of the total selected sample.
Comparing the expected error distributions (see Figures 4.11 and 4.15) also demonstrates the

TGC Parameter	Average error (signal)	Average error (signal + background)
$\alpha_{W\phi}$	0.096	0.116
α_W	0.174	0.199
$\alpha_{B\phi}$	0.34	0.38
Δg_Z^1	0.143	0.167

Table 4.4: *The expected average errors on the fitted parameters for a log-likelihood fit to a sample only containing signal $q\bar{q}Q\bar{Q}$ events (second column) and to a sample contaminated with the estimated fraction of background events (third column).*

reduction of precision when we go from generator level to reconstruction level. Most of this loss comes from the inclusion of the selection efficiency while we cannot account in the resolution function for this loss in precision.
A consistency test was again made using the available high luminosity MC `Pythia` and `Excalibur` experiments, the latter generated at various values of the couplings. The samples were fully simulated through `Delsim` and analysed in the same way as the data, however the different background processes were neglected in this test. The results of the fitted α values using the estimator described above are shown in Table 4.3 (last column). The fit results for the large `Pythia` samples (about 40 times the data size) might be more biased than the smaller data size samples. The `Excalibur` smaller samples reconstruct the generated α value within two standard deviations.
The right column of Figure 4.12 shows the results which were already presented in Table 4.3. The fit results to the `Excalibur` fully simulated samples for different anomalous couplings at various values were put in function of their true values (labeled as 'GEN' in the figure). The three points were then fitted with a straight line. If the offset is compatible with zero and the slope with one then the fit is unbiased. This is illustrated in the figures for the anomalous TGC parameters Δg_Z^1 and α_W where the slopes and offsets are respectively one and zero within one standard deviation. The figure for the parameter $\alpha_{B\phi}$ shows a larger offset, although still compatible with zero. The fit for this parameter is a bit more biased as is shown in Figure 4.16.

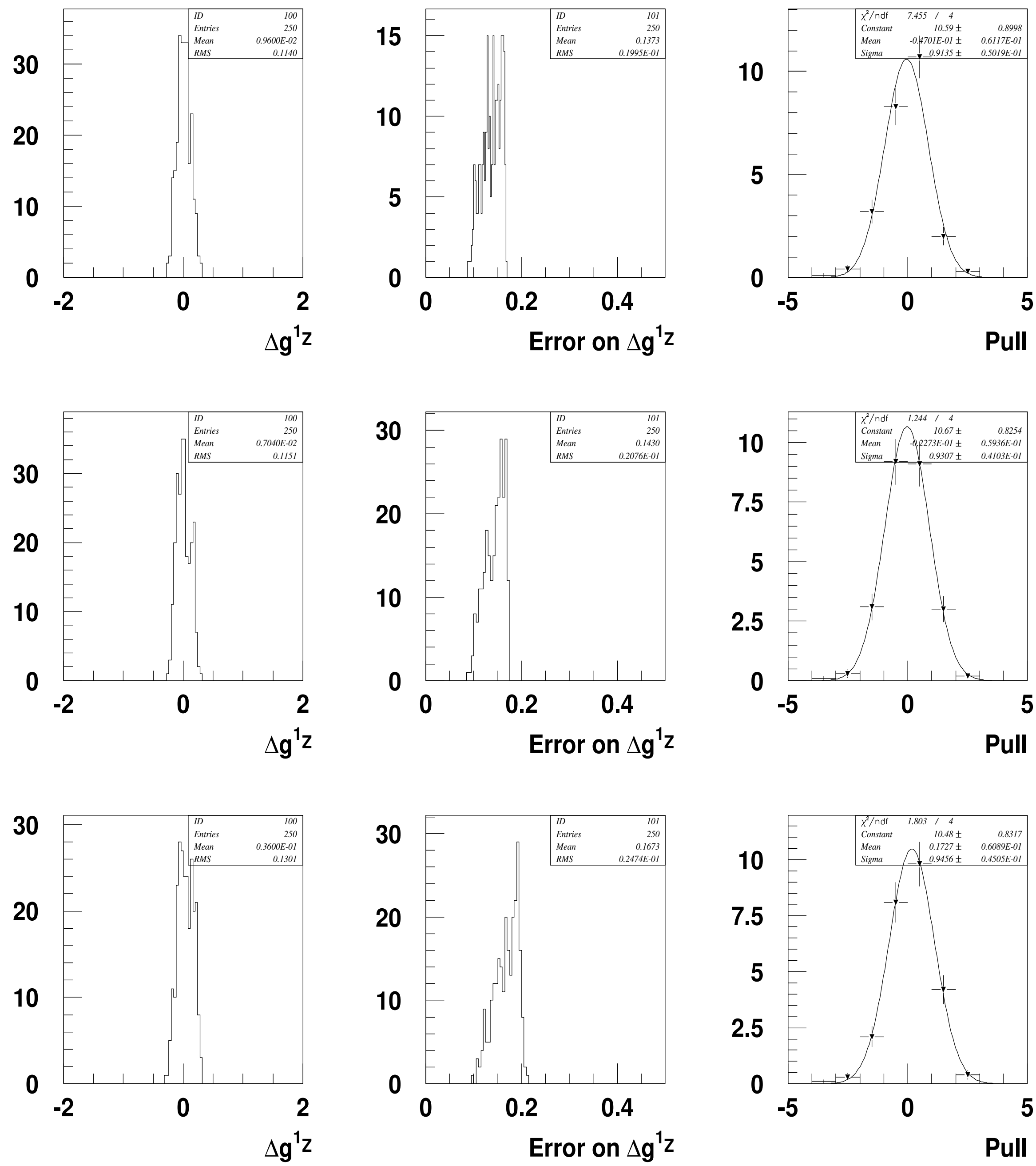

Figure 4.15: *The results of 250 SM MC experiments of 150 pb^{-1} equivalent integrated luminosity each at different levels of reconstruction for the parameter Δg_Z^1.*

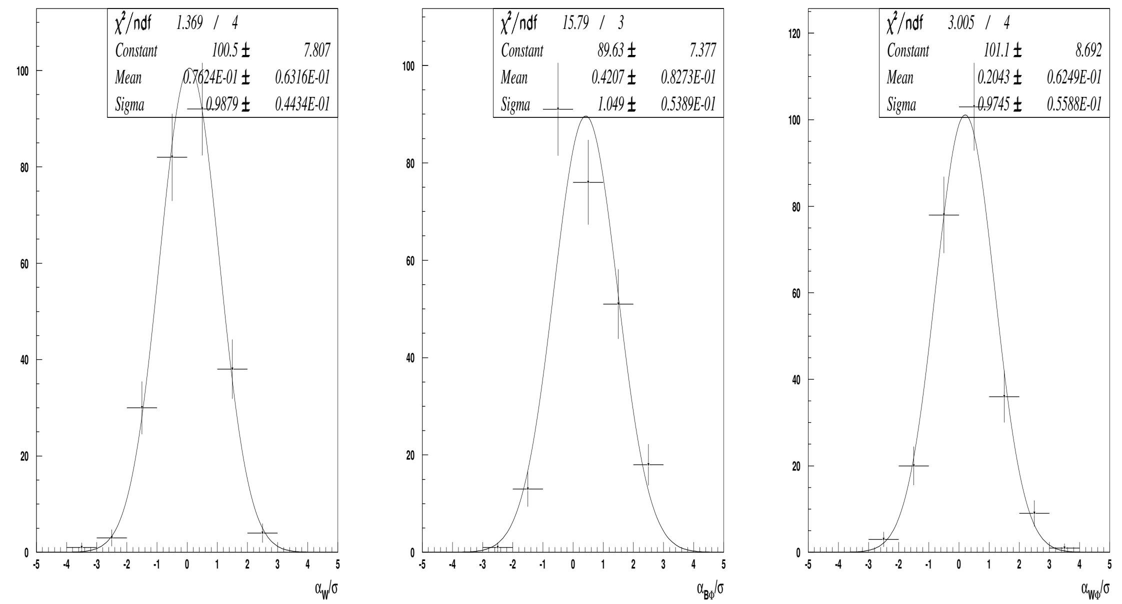

Figure 4.16: *The pull distributions for 250 MC signal experiments of 150 pb^{-1} equivalent integrated luminosity each for the parameters α_W, $\alpha_{B\phi}$ and $\alpha_{W\phi}$.*

4.7 The analysis revisited at 183 GeV

In the following section we will present the analysis as it was carried out for the data taken at 183 GeV. We go through the different steps in the construction of the Extended Maximum Likelihood function. The different verifications on MC samples at reconstruction level are made before presenting the final results.

4.7.1 The EML fit at reconstruction level

The method is exactly the same as at 189 GeV based on the EML function from Equation 4.19

$$\ln L_{EML} = \sum_{i=1}^{n} \ln(Q_{SIG}(\alpha, \Omega_i) + Q_{BKG}(\Omega_i)) - \mathcal{L}(\sigma(\alpha) + \sigma_{BKG}).$$

The probability to observe a background event is given by Equation 4.20. The background processes still have a non-flat behaviour (see Figure 4.5) in the production angle and the shape is estimated from `Pythia` simulated events. The total cross-section σ_{BKG} coming from the background processes ZZ, $q\bar{q}(\gamma)$, other non fully hadronic WW and the small fraction of Zee processes was also estimated from `Pythia` MC events. The probability Q_{SIG} to observe a signal $q\bar{q}Q\bar{Q}$ event still consists of two parts:

$$Q_{SIG}(\alpha, \Omega) = Q_{GP}(\alpha, \Omega) + Q_{BP}(\alpha, \Omega).$$

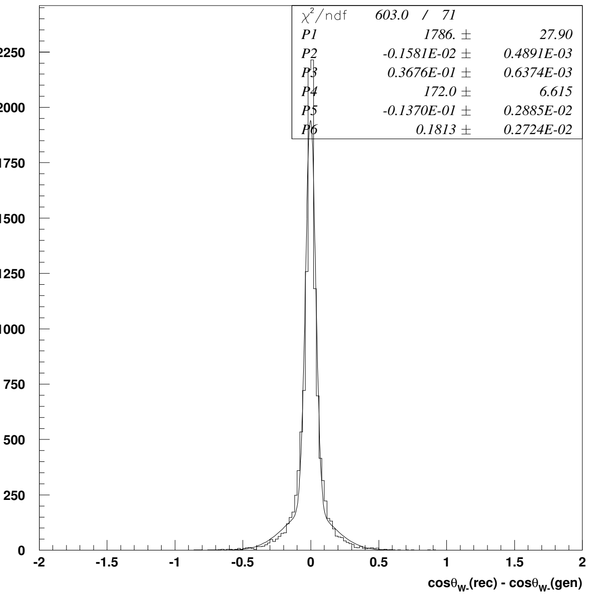

Figure 4.17: *Resolution of the cosine of the production angle at 183 GeV.*

The probability Q_{BP} to observe a badly paired $q\bar{q}Q\bar{Q}$ event is assumed to be flat in $\cos\theta_{W^-}$ as can be seen from Figure 4.5. The expression used for the dependence on α and the production angle is the same as we used for the analysis at 189 GeV and is given by Equation 4.17. The probability to observe a good paired event Q_{GP} is defined in Equation 4.16. The signal selection efficiency ϵ_S was estimated to be $(85.9 \pm 0.3)\%$ (see Table 3.3). The pairing efficiency $\epsilon_P = (72.8 \pm 0.3)\%$ and the probability $P^-(\Delta Q)$ at 183 GeV were discussed in Sections 4.2 and 4.3 respectively. The resolution function R with width $\sigma' \approx 0.064$, evaluated as a sum of two Gaussian functions, with $\sigma_1 \approx 0.037$ and $\sigma_2 \approx 0.18$ respectively, is depicted in Figure 4.17.

The properties of the estimator have been checked for the different parameters to be fitted. The goodness of fit was estimated with 250 small data size SM `Pythia` MC samples. To each of these samples the fit as described above was performed, first to a sample consisting of good paired events only, next we included the badly paired events in the sample and last we added the background processes. We will go through these different levels of the fit for the parameter $\alpha_{W\phi}$. In Figure 4.18 the distribution of the reconstructed values of $\alpha_{W\phi}$, the error on its fitted value and the pull distribution are depicted on each line. The first line shows the results in the case where the fit was performed to the fraction of good paired signal events only. On the next line the same distributions are shown but the parameter fit is now performed to samples containing also the badly paired events. The last line shows the results obtained for a parameter fit to samples where all background processes have been included on top of the signal $q\bar{q}Q\bar{Q}$ events. The distribution of the fitted values $\alpha_{W\phi}$ is centered around zero for all three levels in the reconstruction process. No bias is observed and the average spread is not larger than the average error on the fitted parameter. We can conclude that the estimator is efficient.

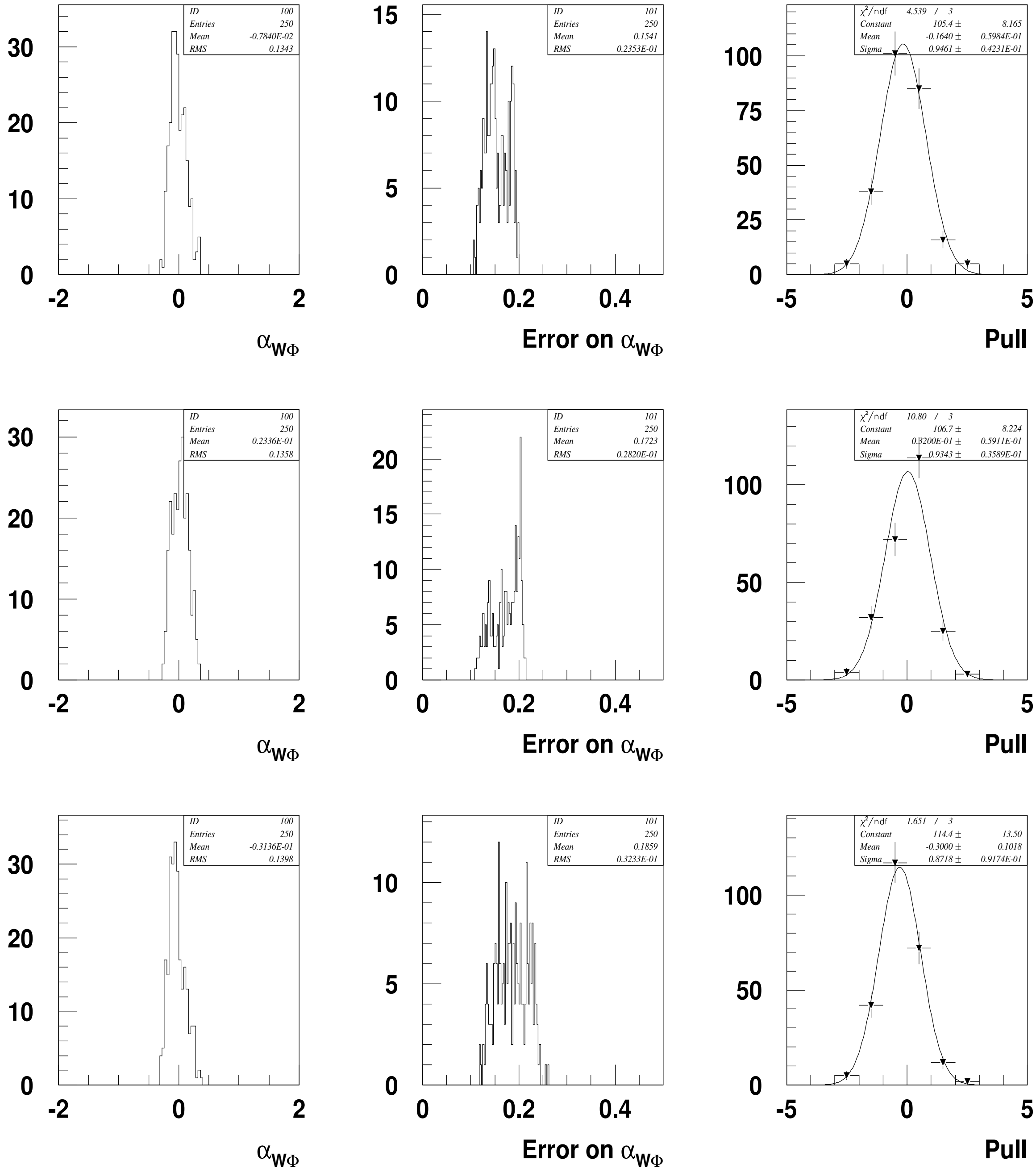

Figure 4.18: *The results of 250 SM MC experiments of 50 pb^{-1} equivalent integrated luminosity each at different levels of reconstruction for the parameter $\alpha_{W\phi}$.*

All pull distributions in Figure 4.18 are Gaussian, centered around zero with widths compatible to one. The estimator for $\alpha_{W\phi}$ can be called unbiased and the expected errors on the fitted parameter are slightly overestimated.
Going from a fit to only signal events to the global fit including background events reduces precision. From an average error on the fitted values of 0.17 we go to an average error of 0.19. This is mainly due to the inclusion of the largest background: the $q\bar{q}(\gamma)$ process.
In Figure 4.19 the pull distributions for the other two parameters α_W and Δg_Z^1 are displayed. These pull distributions are for fits to the signal events MC only, and resemble quite well a Gaussian distribution centered around zero and with width compatible with one.
The fit method was not applied for the TGC parameter $\alpha_{B\phi}$ as both differential and total cross-

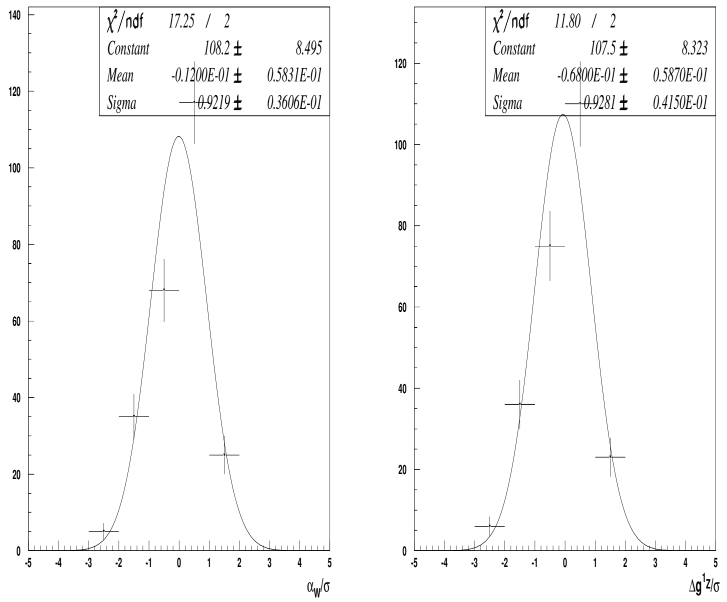

Figure 4.19: *The pull distributions for 250 SM MC signal experiments of 50 pb^{-1} equivalent integrated luminosity each for the parameters α_W and Δg_Z^1.*

section are not very sensitive to this TGC parameter (see Figures 4.6 and 4.7) and hence no efficient and unbiased estimator was found for this method. This is illustrated in Figure 4.20. This figure shows the distributions of the fitted parameter $\alpha_{B\phi}$, the error on $\alpha_{B\phi}$ and the pulls for 250 MC samples consisting of signal events each 50 pb^{-1} equivalent integrated luminosity. The distribution of the fitted parameter shows a two peak structure as the probability density function has a non-Gaussian behaviour in $\alpha_{B\phi}$. This stems from the fact that the total cross-section and hence the total number of events used is quadratic in α. For some parameters, especially for $\alpha_{B\phi}$, this quadratic behaviour is much less pronounced than for others. This is clearly demonstrated in Figure 4.7. On top of that the dependence of the shape on $\alpha_{B\phi}$ is worse for this anomalous coupling than for the others. It has the worst expected sensitivity, as already demonstrated, and in some cases there can be confusion and multiple minima leading to a biased estimation of $\alpha_{B\phi}$. These problems have been pointed out in references [52, 112, 113]. The information coming from

the $\cos\theta$ distribution in a fit to the differential cross-section helps in making the right decision but as can be seen from Figure 4.6 for $\alpha_{B\phi}$ the sensitivity does not really improve. This effect was already observed at $\sqrt{s}$ = 189 GeV but is more pronounced here as the sample is three times smaller and the total cross-section has a bigger impact in the likelihood fit at this lower centre-of-mass energy.
In Figure 4.21 the results of the fit for Δg_Z^1 to the 250 signal MC samples are plotted as a function

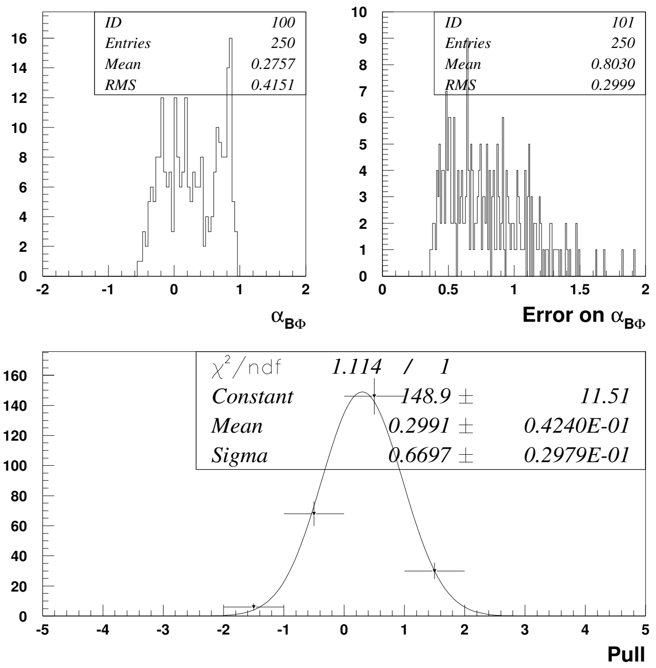

Figure 4.20: *Distibutions of the fitted parameter $\alpha_{B\phi}$, the error on this parameter and the pulls for 250 MC signal samples of 50 pb^{-1} equivalent integrated luminosity.*

of the error on this fitted value. The distribution is asymmetric extending from Δg_Z^1 of -0.5 to 0.4 but with the highest probabilities at negative values for which the error values are minimum. The error grows with α but shows a turning point at $\Delta g_Z^1 \approx 0.1$. This effect is induced by the inclusion of the total cross-section in the fit of the TGC parameters and the use of reduced kinematic information (only the production angle). As the cross-section is quadratic in α a better precision is obtained for high $|\alpha|$. The figure illustrates this effect for the parameter Δg_Z^1 but the explanation is valid for all anomalous coupling parameters.
To verify the consistency and bias of the estimator, the fit at reconstruction level but without background was applied to a `Pythia` MC sample with all TGC parameters at their SM value and of a size much larger than the size of the data sample (about a factor 55). An overview of the results can be found in Table 4.5. In all cases no bias could be observed as the SM values were found back within one standard deviation.
To verify whether the fit was consistent at non-SM values the fit was repeated with `Excalibur` MC samples which had their TGC parameter values set to values far away from the SM. The

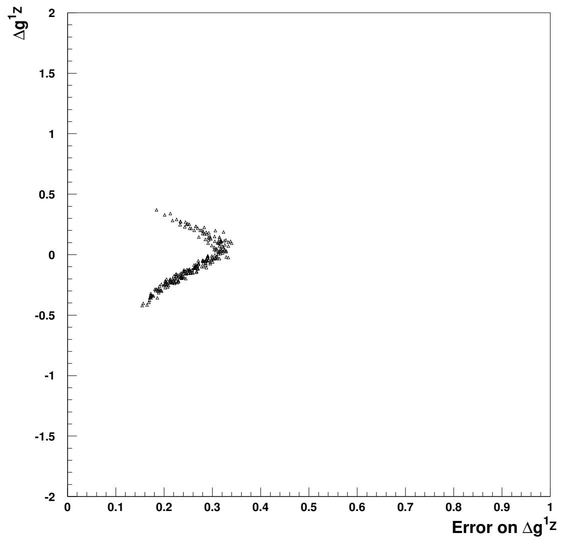

Figure 4.21: *The results of the fit versus the error on the fitted parameter for 250 signal SM MC experiments of each 50 pb^{-1} equivalent integrated luminosity.*

results can also be found in Table 4.5. This proves that the estimators are consistent as all values are retrieved within three standard deviations at most.
The obtained fitted values were studied as a function of the true values and are shown in Figure 4.22. A linear fit was then performed to these points. We can conclude that no bias was observed and all slopes are compatible with one. The offsets on the vertical axes are compatible with zero within one or two standard deviations.

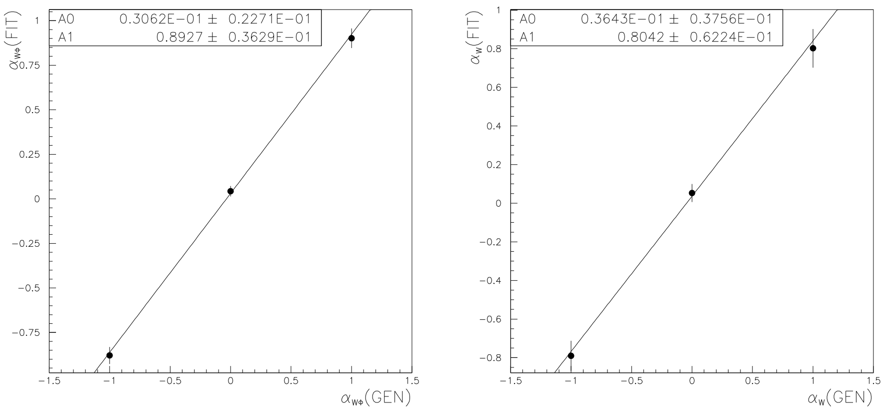

Figure 4.22: *Bias of the estimator for signal events at 183 GeV for reconstructed level kinematic information. The reconstructed parameters are labeled 'FIT' and the true parameter values labeled 'GEN'.*

Generator	Coupling	gen. value	$\mathcal{L}(\mathrm{pb}^{-1})$	fit. value (from rec. level)
Pythia	$\alpha_{W\phi}$	0.	2751.	$0.021^{+.024}_{-.023}$
Excalibur		0.	1612.	$0.042^{+.029}_{-.028}$
		$-1.$	95.	$-0.87^{+.05}_{-.05}$
		+1.	107.	$0.90^{+.05}_{-.06}$
Pythia	α_W	0.	2751.	$0.027^{+.042}_{-.040}$
Excalibur		0.	1612.	$0.053^{+.047}_{-.046}$
		$-1.$	119.	$-0.79^{+.08}_{-.08}$
		+1.	125.	$0.802^{+.095}_{-.110}$
Pythia	Δg_Z^1	0.	2751.	$0.009^{+.035}_{-.034}$
Excalibur		0.	1612.	$0.024^{+.039}_{-.038}$

Table 4.5: *Results of the EML fits at reconstruction level for MC events at a centre-of-mass energy of 183 GeV. Reconstruction level refers to fits performed using reconstructed four-momenta.*

Chapter 5

Results and discussion

5.1 Introduction

In the previous chapter the applied Extended Maximum Likelihood method was explained and tested. It was found to give an unbiased, efficient and consistent estimator for the extraction of the anomalous TGC couplings from the present data set. In this chapter we apply this fit method to the data taken with the DELPHI detector at the centre-of-mass energies of 189 and 183 GeV. We perform one dimensional fits for each of the four TGC parameters Δg_Z^1, $\alpha_{W\phi}$, α_W and $\alpha_{B\phi}$, allowing only one TGC parameter to vary while the others are held at their SM model values. Only three parameters are extracted in the analysis at $\sqrt{s}$ = 183 GeV as the insensitivity to $\alpha_{B\phi}$ is rather high due to low statistics and an important contribution of the total production cross-section to the likelihood fit (see Section 4.7). The results of the fits can be found in Sections 5.2 and 5.3 respectively.
Experimental measurements are usually influenced by two types of errors, statistical and systematic. While the former arise from fluctuations in the finite dataset, the systematic errors are due to such effects as background contamination, incorrect calibrated instruments and inadequate theories. The systematic errors will be discussed in Section 5.4.
In Section 5.5 the results from the two data sets are combined with inclusion of all evaluated systematic effects. In a following section these final results are discussed.
The TGC parameters are not only measured as presented here, but also other results exist from the DELPHI experiment, the other LEP collaborations and a few other experiments. An overview of these measurements is given in Section 5.7. In the final section we discuss what can be expected from future experiments on TGC parameter measurements.

5.2 Fits to the data collected at $\sqrt{s}$ = 189 GeV

In Chapter 3 the selection criteria were presented in order to obtain in an efficient way a pure $q\bar{q}Q\bar{Q}$ sample. A total of 1326 hadronic WW events was selected from the data sample corresponding to an integrated luminosity of 154.39 pb^{-1} with an efficiency of (82.5±0.3)%. The purity of the data sample was estimated from MC to be (71.0±2.0)%. The summary of the selection criteria and corresponding efficiencies and purities can be found in Tables 3.4 and 3.3 respectively.

The analysis to obtain the TGC parameters at this centre-of-mass energy is described in the presentation of the fit procedure in Section 4.6. The form of the likelihood function used is as described in formula 4.19. The parameters obtained from the fits to these 1326 selected $q\bar{q}Q\bar{Q}$ events are shown in Table 5.1. The corresponding log-likelihood curves are depicted in

TGC Parameter	Fit results at 189 GeV	95% CL interval at 189 GeV	Expected errors Upper	Lower
Δg_Z^1	-0.117$^{+.141}_{-.117}$	[-0.334,0.194]	+0.175±0.026	-0.154±0.023
$\alpha_{W\phi}$	-0.071$^{+.096}_{-.083}$	[-0.227,0.139]	+0.125±0.018	-0.107±0.017
$\alpha_W \equiv \lambda_\gamma$	-0.119$^{+.169}_{-.131}$	[-0.359,0.289]	+0.212±0.049	-0.179±0.041
$\alpha_{B\phi} \equiv \Delta\kappa_\gamma$	-0.029$^{+.486}_{-.302}$	[-0.569,1.308]	+0.41±0.05	-0.327±0.058

Table 5.1: *The results for the four TGC parameters obtained from fits to data taken at a centre-of-mass energy of 189 GeV, corresponding to a total integrated luminosity of 154.39 pb^{-1}. The quoted errors on the results are one standard deviation statistical errors. The 95% Confidence Level intervals are written between square brackets in the second column. The expected upper and lower errors are given in the third column.*

Figure 5.1. The arrows indicate the global minimum and hence the result of the fits. The dotted and dashed-dotted horizontal lines correspond to the 68% and 95% Confidence Levels of the fitted results respectively. The 95% Confidence Level intervals can also be found in Table 5.1 between the square brackets. The errors on the fitted parameters are purely statistical; the systematic errors will be discussed in a later section.
All results agree with the SM expectations, no significant deviations are observed. In the last column of Table 5.1 the expected upper and lower errors are shown as they were estimated from 250 MC samples of 150 pb^{-1} each. The errors on the fitted values are well within expectation of these predicted MC values. The parameters that could be extracted with the best statistical precision are $\alpha_{W\phi}$, Δg_Z^1 and α_W; $\alpha_{B\phi}$ is extracted with least precision.

5.3 Fits to the data collected at $\sqrt{s}$ = 183 GeV

The selection criteria developed to select a pure $q\bar{q}Q\bar{Q}$ sample at a centre-of-mass energy of 183 GeV are slightly different from those developed for the analysis at 189 GeV. These criteria are also described in Chapter 3. We could select 476 fully hadronic WW events from the data taken by the DELPHI detector at $\sqrt{s}$ = 183 GeV corresponding to an integrated luminosity of 52.6 pb^{-1}. The selection efficiency and the sample purity were estimated from Monte Carlo samples to be (85.9±0.3)% and (67.0±2.0)% respectively. All these facts are summarised in Table 3.3.

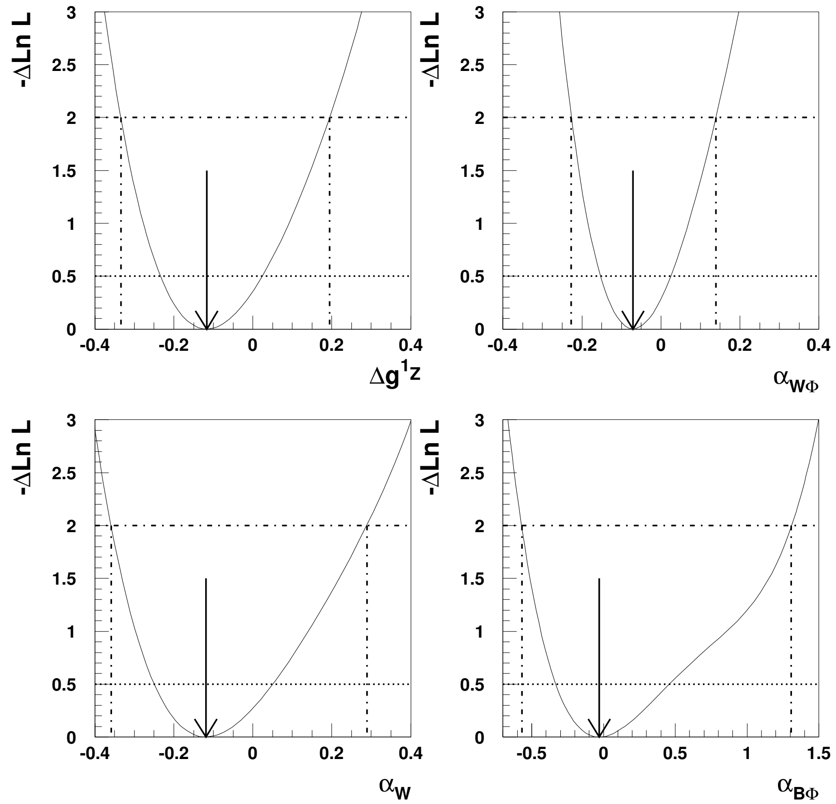

Figure 5.1: *The negative log-likelihood curves for fits to the data taken at 189 GeV for the four parameters. The dotted lines indicate the 68% Confidence Levels, the dashed-dotted lines indicate the 95% CL intervals. The arrows indicate the result of the fit.*

In Section 4.7 we presented the fit procedure for the data taken at a centre-of-mass energy of 183 GeV. The form of the likelihood function applied to extract the TGC parameters from the data sample is given by Equation 4.19.
The parameters obtained from the fits to the 476 selected $q\bar{q}Q\bar{Q}$ events selected at a centre-of-mass energy of 183 GeV can be found in Table 5.2. The corresponding log-likelihood curves are depicted in Figure 5.2. The arrows indicate the global minimum and hence the most likely value of the estimated quantity. The dotted and dashed-dotted horizontal lines indicate the 68% and 95% Confidence Levels of the fit results respectively. The 95% Confidence Level intervals can also be found in Table 5.2. These results include only statistical errors as the systematic errors will be evaluated in a later section.
All values agree with the SM, no deviation could be observed. The errors obtained are of the order of the expected errors as can be seen from Table 5.2. In the last column of this table the average upper and lower errors are given as they were estimated from 250 MC samples of 50 pb^{-1} each. As expected (see Section 4.7), the precision on $\alpha_{W\phi}$ is better than for the other TGC parameters as it has the best sensitivity to the shape and expected number of events. Moreover the use of only one kinematic variable and a fit to rather low statistics at this lower centre-of-mass energy degrades the sensitivity with respect to the analysis at $\sqrt{s} = 189$ GeV.

TGC Parameter	Fit results at 183 GeV	95% CL interval at 183 GeV	Expected errors Upper	Expected errors Lower
Δg_Z^1	+0.111$^{+.288}_{-.288}$	[-0.391,0.611]	+0.28±0.04	-0.23±0.04
$\alpha_{W\phi}$	+0.098$^{+.237}_{-.205}$	[-0.265,0.529]	+0.20±0.03	-0.17±0.03
$\alpha_W \equiv \lambda_\gamma$	+0.139$^{+.349}_{-.329}$	[-0.423,0.730]	+0.33±0.06	-0.25±0.05

Table 5.2: *The results for the four TGC parameters obtained from fits to data taken at a centre-of-mass energy of 183 GeV, corresponding to an integrated luminosity of 52.6 pb^{-1}. The quoted errors on the results are one standard deviation statistical errors. The 95% Confidence Level intervals are written between square brackets in the second column. The third column gives the expected upper and lower errors.*

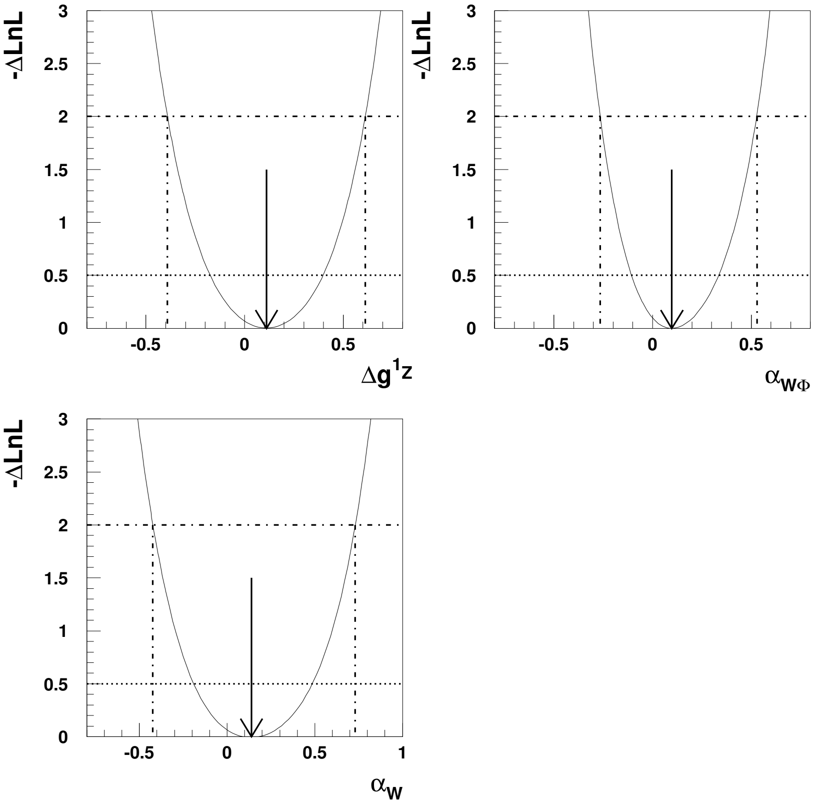

Figure 5.2: *The negative log-likelihood curves for the fits to the data taken at 183 GeV for the three parameters. The dotted lines indicate the 68% Confidence Levels, the dashed-dotted lines indicate the 95% CL intervals. The arrows indicate the result of the fit.*

As we have already observed in the previous chapter and section and given by Equation 1.30, the precision for all parameters improves when we perform the analysis at higher centre-of-mass energies with more data.

5.4 Systematic effects

Various sources of systematic errors were considered for each of the TGC parameters for the analyses at each of the centre-of-mass energies. A description is given in this section. The resulting errors on the measured values are shown in Table 5.3.
Unless mentioned otherwise, the systematic errors on the fitted TGC parameters were estimated

Source	$\sqrt{s} = 189$ GeV				$\sqrt{s} = 183$ GeV		
	Δg_Z^1	$\alpha_{W\phi}$	α_W	$\alpha_{B\phi}$	Δg_Z^1	$\alpha_{W\phi}$	α_W
σ_{WW}	0.03	0.02	0.03	0.12	0.04	0.009	0.04
σ_{BKG}	0.03	0.02	0.04	0.14	0.02	0.009	0.02
W mass	0.01	0.006	0.01	0.04	0.01	0.008	0.01
Beam Energy	0.002	0.001	0.003	0.006	0.005	0.002	0.008
Luminosity	0.02	0.01	0.02	0.09	0.02	0.003	0.02
Detector Effects	0.07	0.05	0.08	0.15	0.09	0.09	0.09
Fragmentation	0.04	0.05	0.04	0.07	0.04	0.05	0.04
ΔQ	0.001	0.001	0.001	0.001	0.003	0.003	0.004
ISR	0.002	0.002	0.001	0.001	0.008	0.007	0.009
CR	0.001	0.01	0.005	0.03	0.001	0.01	0.005
Total Syst. Error	0.10	0.08	0.10	0.27	0.11	0.10	0.12

Table 5.3: *Overview of all systematic errors evaluated for the TGC parameters at both centre-of-mass energies (189 GeV in the left column and 183 GeV in the right column).*

by studying the shift of the minimum of the likelihood function when imposing the considered effect in the EML expression.

Theoretical uncertainty on the W^+W^- production cross-section σ_{WW}
The differential cross-section calculated by Bilenky and the total cross-section σ^{EXC} computed with `Excalibur` used in the EML formula have a theoretical uncertainty of $\pm$ 2% [48]. Each TGC parameter fit to the data sample was repeated with the value of the cross-sections varied in both directions by this amount. The magnitude of the resulting shifts in the TGC parameters were taken as the systematic error arising from this source. As the shifts were not symmetric, a conservative approach was followed and the largest shift was quoted as the systematic error.

Uncertainty on the cross-section σ_{BKG} of the background processes
In Chapter 3 we estimated the cross-sections for the different background processes from Monte Carlo samples with an uncertainty of 5%. The expected cross-section for the background processes used in the EML expression was varied by $\pm$ 5% and the fit to the data sample was repeated. Again the largest shifts in TGC parameters were taken as systematic errors.

Uncertainty on the mass of the W boson

The W mass enters in the different WW cross-sections calculations used in the likelihood expression. Therefore its influence on the TGC determination was studied. The uncertainty on the measurement of the mass of the W boson was taken to be $\pm$ 100 MeV/c^2 [114]. The signal cross-sections were recalculated accordingly with the Bilenky expression and the `Excalibur` generator. The fits with the recomputed signal cross-sections in the likelihood expression were then repeated to the data sample. The largest observed shifts in the TGC parameters were taken as systematic errors.

Uncertainty on the beam energy

The errors on the LEP beam energy (see also Section 3.6) for the 1997 run (183 GeV) and 1998 run (189 GeV) were estimated to be 25 MeV and 20 MeV respectively. The systematic contribution resulting from this uncertainty was estimated in the same way as the contribution from the W mass. All signal cross-sections were recomputed for the new centre-of-mass energies, the fits with the new likelihood expression were repeated to the data sample and the largest shifts in TGC parameters were taken as systematic errors.

Uncertainty on the luminosity $\mathcal{L}$

The error on the integrated luminosity taken by DELPHI at $\sqrt{s}$ = 183 GeV and 189 GeV is around $\pm$ 1% (see also Section 3.5). The fits were repeated after scaling the expected number of signal and background events accordingly. The largest shifts in the minimum of the likelihood function were quoted as systematic errors.

Uncertainties coming from detector effects

The detector simulation does not always give a good description of the detector response and

Source of systematic uncertainty	$\sqrt{s}$ = 189 GeV				$\sqrt{s}$ = 183 GeV		
	Δg_Z^1	$\alpha_{W\phi}$	α_W	$\alpha_{B\phi}$	Δg_Z^1	$\alpha_{W\phi}$	α_W
E_{jet} smearing	0.04	0.03	0.05	0.14	0.04	0.03	0.06
Direction smearing	0.01	0.009	0.01	0.02	0.02	0.02	0.02
Corr. fac. to E_{jet} as function of:							
$\cos\theta_{jet}$	0.06	0.04	0.06	0.06	0.08	0.08	0.07
E_{jet}	0.002	0.002	0.003	0.01	0.01	0.01	0.02
Total Syst error	0.07	0.05	0.08	0.15	0.09	0.09	0.09

Table 5.4: *Overview of the different detector effects which contribute to the systematic error in the TGC determination and resulting systematic errors.*

as a consequence differences between data and Monte Carlo are observed for certain kinematic variables. Studies to evaluate the detector effects have been described in reference [115] and the same approach is followed here. Difference in detector effects between data and Monte Carlo that have been studied are the uncertainty on the jet angular direction (5 mrad) and the uncertainty on the jet energy (4%). Two functions describing the difference in jet energy between data and MC as a function of the polar jet angle and as a function of the true energy of the jet were calculated

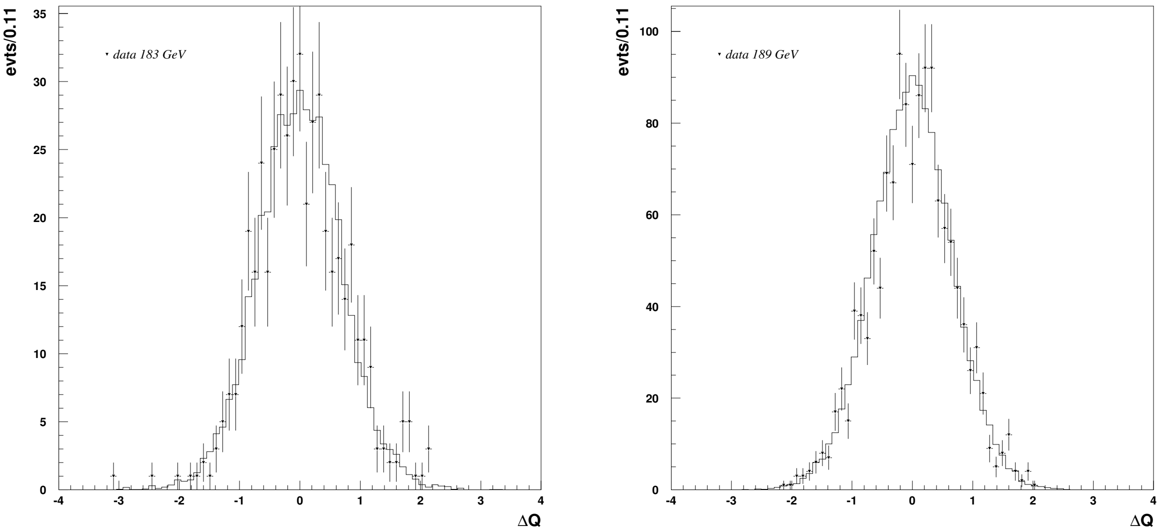

Figure 5.3: *The distributions of ΔQ for data (points) and MC (histogram) for centre-of-mass energies of 183 GeV (left) and 189 GeV (right).*

from a study of $Z \rightarrow q\bar{q}$ events [116]. These detector effects were applied to the data sample by smearing the jet angular direction and energy and by scaling the jet energies in function of their true jet energy or in function of their polar angle. The fits were repeated to these four affected samples. The shift in the TGC parameter gives the systematic error. The systematic errors from these four contributions together with the total systematic uncertainty from detector effects are given in Table 5.4.

Uncertainty coming from fragmentation

Two simulated data sets were compared in order to estimate the systematic uncertainty resulting from the uncertainty in the jet hadronisation modeling. A set of 100,000 events was generated with `KoralW` [117][1], at a centre-of-mass energy of 189 GeV, and the two fragmentation models `Jetset` [93] and `Herwig` [118] were applied resulting in two MC samples. The TGC parameter fits to each of these samples were then performed and the difference in TGC parameter value was quoted as the systematic error induced by fragmentation uncertainties. As no such sample was available for data taken at 183 GeV, the same systematic error was quoted in this case.

Uncertainty on ΔQ

In Figure 5.3 the ΔQ distributions for data and MC events are plotted. For both centre-of-mass energies an average shift between the data and MC histograms of 0.02 is observed, while the widths of distributions for data and MC are compatible. The ΔQ variable was shifted for each event in the data sample by this amount in both directions. The TGC fits were then repeated to these samples and the largest resulting shift in the TGC parameters were the quoted systematic errors coming from this uncertainty.

[1]This `KoralW` sample was generated in the framework of the common sample study by the four LEP experiments.

Uncertainty coming from Initial State Radiation
A comparison of two independent models of ISR was performed [115]. Hadronic events generated with `Excalibur` were reweighted as a function of the total ISR energy in the event. The weights were obtained from a generator level study of the `Koralw` [117] ISR treatment (based on the YFS exponentiation approach) and that of the standard algorithm used in DELPHI: `Qedps` [70] (based on a parton shower approach, see also Section 1.5.4). The TGC parameter fit to this reweighted sample was compared to the result of the TGC fit to the non-reweighted sample and this difference was quoted as a systematic error.

Uncertainty on Colour Reconnection
Effects of Colour Reconnection (CR) have been studied by comparing the results of the fits to two large Monte Carlo samples generated at a centre-of-mass energy of 189 GeV. The `Jetset` reference sample is the same as the one used in the study of the uncertainty coming from fragmentation (see above) containing no reconnected events. The hadronic events in the CR sample have a maximal reconnection probability following the SKI model [73]. The TGC parameter fits to each of these samples were then performed and the difference in TGC parameter value was quoted as the systematic error induced by Colour Reconnection uncertainties. The systematic error quoted for the 183 GeV analysis is the same as no samples were available at this centre-of-mass energy.

Conclusion
Large systematic error contributions come from the uncertainties on the signal and background cross-sections, from the uncertainties coming from fragmentation and from detector effects. In Table 5.5 the statistical and systematic errors for each of the TGC parameters for both analyses are compared. In all cases the statistical error is still larger or comparable to the total systematic error.

TGC Parameter	189 GeV analysis		183 GeV analysis	
	Stat. Error	Syst. Error	Stat. Error	Syst. Error
Δg_Z^1	0.13	0.10	0.31	0.11
$\alpha_{W\phi}$	0.09	0.08	0.23	0.10
$\alpha_W \equiv \lambda_\gamma$	0.15	0.10	0.38	0.12
$\alpha_{B\phi} \equiv \Delta\kappa_\gamma$	0.36	0.27		

Table 5.5: *Comparison of the (symmetrised with* `Minuit`*) statistical and systematic error for each TGC parameter for both analyses.*

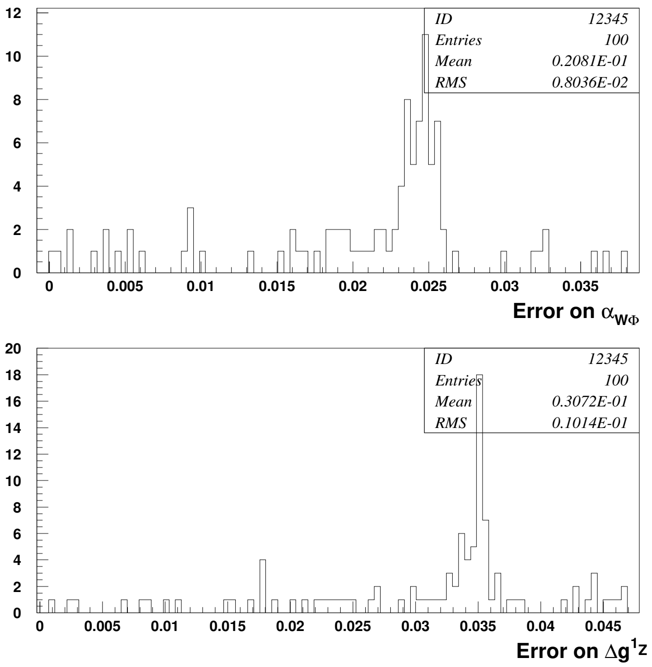

Figure 5.4: *The expected systematic errors on $\alpha_{W\phi}$ (upper plot) and Δg_Z^1 (lower plot) arising from uncertainties on the signal cross-section computed for 100 MC samples equivalent to 50 pb^{-1} at $\sqrt{s} = 183$ GeV.*

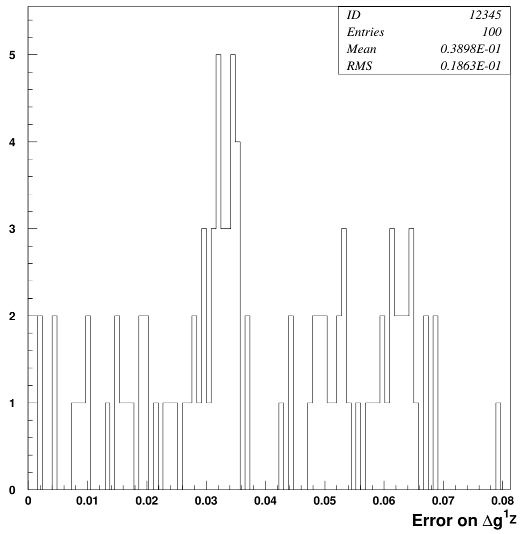

Figure 5.5: *The expected systematic errors on Δg_Z^1 arising from uncertainties on the signal cross-section computed for 100 MC samples equivalent to 150 pb^{-1} at $\sqrt{s} = 189$ GeV.*

In Figures 5.4 and 5.5 the expected systematic errors on $\alpha_{W\phi}$ and Δg_Z^1 arising from the uncertainties on the signal cross-section are displayed for samples simulated at $\sqrt{s}$ = 183 GeV and $\sqrt{s}$ = 189 GeV respectively. This cross check was done for 100 data size Monte Carlo samples at both centre-of-mass energies. The systematic uncertainties were computed in the same way as it was done for the data sample. One sees that the systematic uncertainties coming from this source quoted for the data sample (see Table 5.3) agree with the expected errors. The mean expected error on Δg_Z^1 at $\sqrt{s} = 189$ GeV is 0.04, while we quote 0.03 for the data sample collected at this centre-of-mass energy. For the analysis performed at $\sqrt{s} = 183$ GeV, the quoted errors on $\alpha_{W\phi}$ and Δg_Z^1 lie within the range of the expected errors. The systematic uncertainty for $\alpha_{W\phi}$ is lower than the average while the uncertainty for Δg_Z^1 is higher.

5.5 Combination of the two data sets

The combination of the TGC parameter fit results for the analyses at 183 GeV and 189 GeV is given in Table 5.6. This combined result is obtained by adding the individual likelihood curves. For the TGC parameter $\alpha_{B\phi}$ only the result obtained at $\sqrt{s} = 189$ GeV is given. The results presented in the first column of this table are quoted with two errors: the statistical error and the total systematic error. We considered all systematic uncertainties as correlated systematic contributions between years. For the calculation of the 95% Confidence Level interval the total systematic error was included in the likelihood curve L and a "new" likelihood curve L' was obtained in the following way

$$L' = \frac{\sigma_{\rm stat}^2}{\sigma_{\rm stat}^2 + \sigma_{\rm syst}^2} L, \tag{5.1}$$

with $\sigma_{\rm stat}$ the total statistical error on the measurement and $\sigma_{\rm syst}$ the total systematic error.
The results presented as log-likelihood curves can be found in Figure 5.6. In each of the figures

TGC Parameter	Combined result	95% CL interval
Δg_Z^1	-0.077$^{+.134}_{-.113}$ $\pm$ 0.098	[-0.336,0.298]
$\alpha_{W\phi}$	-0.042$^{+.090}_{-.079}$ $\pm$ 0.081	[-0.241,0.246]
$\alpha_W \equiv \lambda_\gamma$	-0.073$^{+.165}_{-.128}$ $\pm$ 0.106	[-0.335,0.406]
$\alpha_{B\phi} \equiv \Delta\kappa_\gamma$	-0.029$^{+.486}_{-.302}$ $\pm$ 0.27	[-0.679,1.518]

Table 5.6: *Values of the Triple Gauge Boson Couplings combining the analyses at the centre-of-mass energies 189 GeV and 183 GeV. The second column gives the combination result with one standard deviation statistical error and the common systematic error. The third column gives the 95% CL interval with all errors included.*

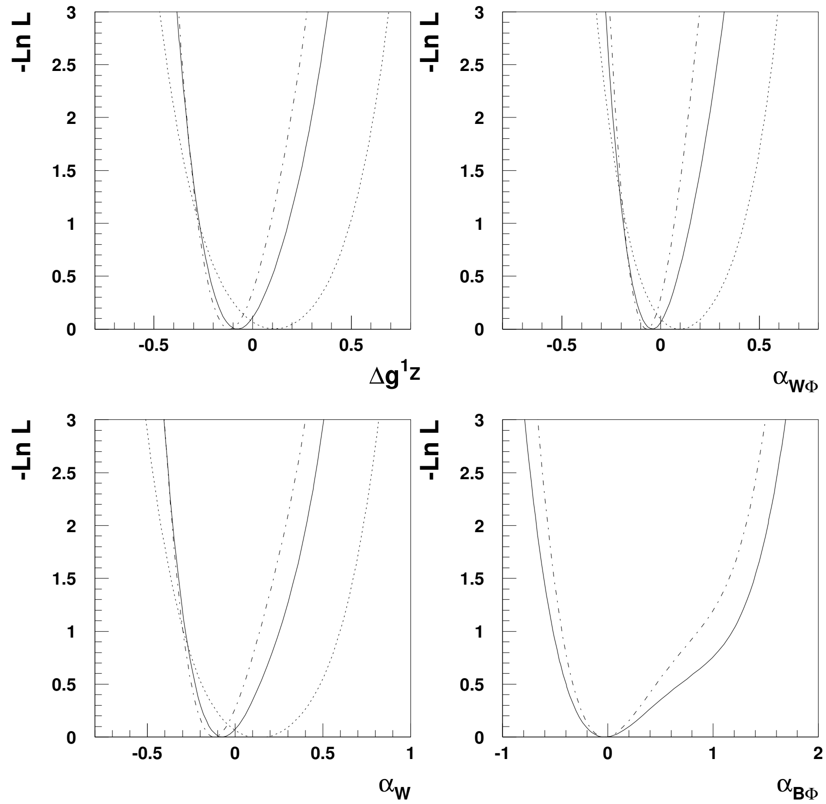

Figure 5.6: *Negative log-likelihood curves for the one parameter fits of the combined result including all uncertainties for each of the TGC parameters (full line). The dashed-dotted (dashed) curve gives the likelihood curve of the result for the 189 GeV (183 GeV) analysis separately.*

the results obtained at 189 GeV and 183 GeV are presented by dashed-dotted and dashed lines respectively. The full line represents the combined result including the total systematic error. In the case of $\alpha_{B\phi}$ the full line represents the result obtained at $\sqrt{s}$ = 189 GeV including the total systematic error on this parameter. From this figure it appears that the weight of the likelihood curves obtained for the analysis at 189 GeV is by far the largest. This is expected as we have three times more data and increased sensitivity to the TGC parameters at this higher centre-of-mass energy.

5.6 Discussion of the results

In the previous section we presented the combined results for both analyses at the two centre-of-mass energies of 183 and 189 GeV. The results including both statistical and systematic errors for the one parameter fits, with one standard deviation errors are given below:

$$\begin{aligned}\Delta g_Z^1 &= -0.077^{+.176}_{-.141},\\ \alpha_{W\phi} &= -0.042^{+.129}_{-.107},\\ \alpha_W \equiv \lambda_\gamma &= -0.073^{+.214}_{-.156},\\ \alpha_{B\phi} \equiv \Delta\kappa_\gamma &= -0.029^{+.713}_{-.368}.\end{aligned}$$

All four parameters agree within one standard deviation of their Standard Model value. Hence no indication of new physics is observed. As we already demonstrated in the previous chapter the measurement of $\alpha_{W\phi}$ and Δg_Z^1 are the most precise while the fitted value of $\alpha_{B\phi}$ is least precise. The lack of statistics and the use of little kinematic information is the cause why $\alpha_{B\phi}$ could not be measured in an unambiguous way in the 183 GeV analysis[2]; we remarked an improvement of these ambiguities with the 189 GeV analysis.
The analysis at 189 GeV has smaller statistical errors as it contains about three times more data, therefore it also has a greater weight in the combination of the two analyses. The systematic error on the combined values is still smaller than the statistical error for all parameters, but $\alpha_{W\phi}$. The total systematic error on this parameter is of the order of the statistical error for the combined result. In spite of the higher degree of ambiguity in the hadronic channel, this channel can considerably improve the sensitivity to the charged anomalous couplings.

5.7 Other TGC measurements

DELPHI results
Not only the $q\bar{q}Q\bar{Q}$ channel is used for the measurements of TGC parameters, but DELPHI has also obtained results for the semi-leptonic channels. As this signal has a clean charge signature the analysis is a bit more straightforward and more precise than the hadronic channel. The DELPHI published analyses [114, 119, 39], for the hadronic and semi-leptonic channels, are based on an Optimal Variable method [120]. This technique relies on the fact that the differential cross-section is quadratic in the TGC parameters α. This expression can also be seen as a Taylor expansion around the SM cross-section. Out of the coefficients, two optimal variables containing all available kinematic information (W^- production angle and decay angles of both W's) of the event can be constructed. The direction which is most sensitive to the couplings is picked out by the optimal observables in the five dimensional angular space, so optimal use of the available angular information is made.
The combined results for the one parameter fits to the data sets consisting of the hadronic and semi-leptonic WW channels and of the single W channel (see paragraph on LEP results) taken by DELPHI [39] at centre-of-mass energies between 172 GeV and 202 GeV are:

$$\begin{aligned}\Delta g_Z^1 &= -0.03 \pm .04,\\ \lambda_\gamma &= 0.06 \pm .05,\\ \Delta\kappa_\gamma &= 0.06^{+.12}_{-.11}.\end{aligned}$$

The DELPHI results are quoted in terms of Δg_Z^1, λ_γ and $\Delta\kappa_\gamma$ and not in terms of the α parameters. But relations between the two sets exist (c.f. Equation 1.19), and determining α_W is the same as determining λ_γ and analogous $\alpha_{B\phi}$ = $\Delta\kappa_\gamma$ for single parameter fits. The quoted results contain both statistical and systematic errors.

Other LEP results
The other three LEP collaborations ALEPH [121, 36], L3 [122, 42] and OPAL [123, 45] also have published results either based on Optimal Observable methods or information coming from

[2]No result on this parameter at $\sqrt{s} = 183$ GeV is given for these reasons.

TGC Parameter	Fit results	95% CL
$\Delta\kappa_\gamma$	$-0.002^{+.067}_{-.065}$	[-0.13,0.13]
Δg_Z^1	$-0.025^{+.026}_{-.026}$	[-0.074,0.028]
λ_γ	$-0.036^{+.028}_{-.027}$	[-0.089,0.020]

Table 5.7: *The combined LEP results of the one parameter fits (in the first column) with one standard deviation errors (including all systematic errors) and the 95% CL intervals for these results (in the second column).*

event shape and cross-section. Another channel taken into consideration is the production of single W events. The Feynman diagram of the process is shown in Figure 1.7(a). This channel accesses independently the anomalous parameters λ_γ and $\Delta\kappa_\gamma$.

The results of the four LEP collaborations have been combined by the LEP electroweak working group [124]. In Figure 5.7 the negative log-likelihood curves for the combination of all channels for each of the individual experiments and for the combination of the four LEP experiments together are shown. This combination uses the data taken at LEP-2 up to a centre-of-mass energy of 202 GeV corresponding to about 475 pb^{-1} per experiment. An overview of these combined LEP results with one standard deviation errors (systematic effects included) is shown in Table 5.7. The third column of this table gives the 95% Confidence Level intervals for this combination.

As there exist correlations between the parameters, it is better to perform a three parameter fit. This technique is quite complicated and with the limited statistics taken until now not very accurate. Therefore two parameter fits are performed, where two parameters are varied simultaneously while the third one is left at its SM value. In Figure 5.8 the 68% and 95% Confidence Level contour plots are shown for the combined results of the four LEP collaborations. All these results give no indication of deviations from the SM.

TGC measurements at Tevatron

The experiments D0 and CDF at the Tevatron $p\bar{p}$ collider also limit the anomalous couplings [125]. These can be probed in $W\gamma$ production [126, 127] primarily, but as well in WW and WZ production [128, 31]. The vertex is present in the s-channel where a Z or γ is exchanged to form two W bosons for W pair production, or a W boson is exchanged in the case of WZ or Wγ production. The couplings are sensitive to the transverse momentum distribution of the photon in the case of Wγ production and to the transverse momentum distribution of the weak boson in the case of WW or WZ production. The present limits on the anomalous couplings set by the D0 experiment [34] are at 95% CL, for a scale factor Λ = 2 TeV:

$$-0.34 < \lambda_\gamma < 0.36,$$
$$-0.43 < \Delta\kappa_\gamma < 0.59.$$

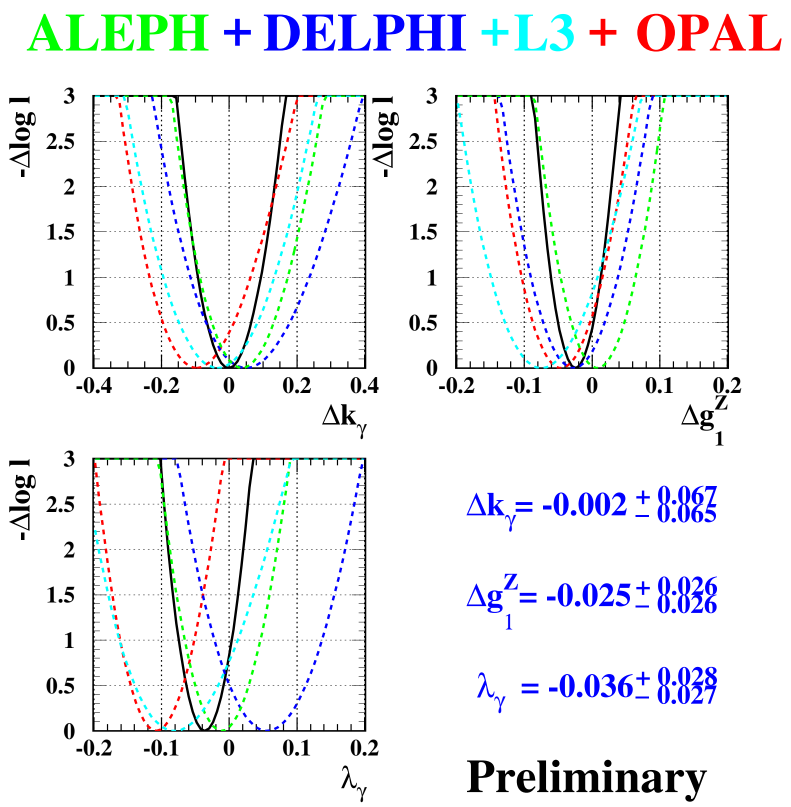

Figure 5.7: *The negative log-likelihood curves combined and for each of the individual* LEP *experiments indicating the fit result to the corresponding TGC parameter.*

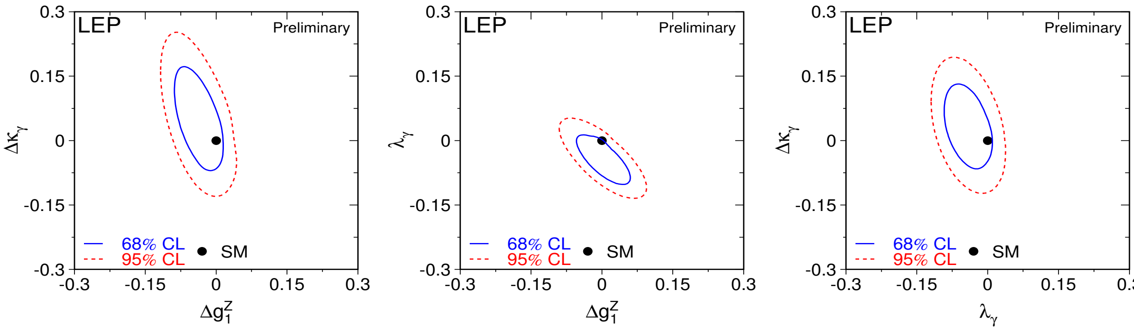

Figure 5.8: *The results of the fits in a two parameter plane. The 68% CL and 95% CL contours are indicated in continuous and dashed lines respectively. The dot indicates the SM value of the TGC parameters.*

These limits are under the assumption that $WW\gamma$ and WWZ couple equally, and each result is under the assumption that the other parameter is at its SM zero value. The Tevatron measurements are complementary to the limits set at LEP as they are measured in different processes, and have different sources of systematic errors.

TGC measurements at HERA
Limits on Triple Gauge Boson Couplings are also set by the experiments at the HERA collider. The $WW\gamma$ vertex can be probed in single W production in ep collisions [129]: $e^+p \rightarrow e^+ W^\pm X$. This measurement gives in an independent way information on the couplings, as only the $WW\gamma$ vertex is measured and the vertex is probed at higher centre-of-mass energies ($\sqrt{s}$ = 300 GeV) than at LEP. Results on the TGC parameters have been published by the ZEUS [130] experiment. The results on the couplings have been interpreted in terms of 95% Confidence Level intervals:

$$-4.7 < \Delta\kappa_\gamma < 1.5,$$
$$-3.2 < \lambda_\gamma < 3.2.$$

5.8 The future

The Tevatron collider and detectors have been upgraded recently. The Tevatron RunII will start in March 2001 with increased integrated luminosities. The cross-section at high boson transverse momentum will increase and as a consequence the sensitivity to the anomalous couplings will increase by a factor five [131]. Also more stringent limits from the HERA experiments can be expected with the luminosity upgrade.
In 2005 data taking will start at the Large Hadron Collider (LHC) [132]. Here, it will also be possible to set limits on the anomalous couplings in pp reactions. The measurements will benefit from the large statistics available (about 1000 times the present data set obtained at Tevatron) and the high centre-of-mass energy (14 TeV). The trilinear couplings will be studied in the same final states as the ones studied at Tevatron: $W\gamma$, WW and WZ production. An improvement of two orders of magnitude with respect to the current Tevatron limits is expected.
In the more distant future the most precise measurements on TGC parameters will come from e^+e^- linear colliders. Bounds on the parameters of the order of 10^{-3} up to 10^{-4} can be reached with W pair events produced in e^+e^- collisions at centre-of-mass energies from 500 GeV and beyond [133].
The limits set by the LEP collaborations are currently most precise. The analyses from the data taken this year (about 200 pb^{-1} per experiment) at centre-of-mass energies ranging from 202 to 209 GeV still have to be included. The final LEP result on TGC measurements will be presented on a total data set of about 700 pb^{-1} per experiment. The final statistical precision of ± 0.02 (for Δg_Z^1 and λ_γ) predicted in [48] for a total integrated luminosity of 500 pb^{-1} is already reached. The systematic errors are becoming of the same order as the statistical precision, hence more effort will have to be dedicated to the reduction of the systematic uncertainties.

Conclusions

This thesis presents the measurement of the Triple Gauge Boson Coupling (TGC) parameters Δg_Z^1, $\alpha_{W\phi}$, α_W and $\alpha_{B\phi}$ with W^+W^- events produced at LEP centre-of-mass energies of 183 GeV and 189 GeV. The data sample corresponds to 52.6 pb^{-1} and 154.39 pb^{-1} of integrated luminosity at the respective centre-of-mass energies. These events are produced in $\mathrm{e}^+\mathrm{e}^-$ annihilation by three Feynman diagrams at tree level: two in the s-channel with the exchange of a Z boson or a photon and one in the t-channel where a ν_e is exchanged. The W boson is short lived, hence one observes only its decay products in the detector. Three final states of the WW events exist. When both W's decay to a $\mathrm{q}\bar{\mathrm{q}}'$ pair we call it the fully hadronic channel. If one W decays to a lepton-neutrino pair ($l\nu$) and the other one decays to a quark pair the final state is called the semi-leptonic channel. The last case is produced when both W bosons decay to a lepton-neutrino pair: the fully leptonic channel. The branching ratios of these channels are 46%, 44% and 10% respectively. The tri-linear vertices $WW\gamma$ and WWZ can be accessed in these WW events through the s-channel of the WW production process where a Z boson or photon will couple to the W pair. LEP offers currently the best possibility to measure the TGC parameters. As the values of these parameters are fixed in the Standard Model it is important to measure them with highest precision possible in order to provide a unique window on possible new physics processes beyond the Standard Model.

This analysis was dedicated to the WW events decaying hadronically as this class represents a large fraction of the total data sample with about 46% of all WW decays. The challenges for the TGC measurement in this channel are twofold. First, it is not straightforward to retrieve the kinematic information necessary for the TGC parameter fit. Second, we have to fight the main background coming from the QCD process $\mathrm{e}^+\mathrm{e}^- \rightarrow Z/\gamma \rightarrow q\bar{q}(+ng)(\gamma)$, with $n \geq 0$.
This process has a high cross section (about 100 pb which is 12 times the signal cross section) at the centre-of-mass energies envisaged and the events can mimic the typical four jet topology of the hadronically decaying WW events when gluon radiation is involved. In Chapter 3 special variables were developed to reduce strongly this background while selecting the desired $q\bar{q}Q\bar{Q}$ events arising from W^+W^- decay. A Monte Carlo study demonstrated that the designed selection criteria gave an efficiency of (85.9 $\pm$ 0.3)% at $\sqrt{s}$ = 183 GeV and of (82.5 $\pm$ 0.3)% at $\sqrt{s}$ = 189 GeV for selection of the $q\bar{q}Q\bar{Q}$ signal events. The background processes were reduced as much as possible and the purity of the selected sample was estimated to be (67 $\pm$ 2)% and (71 $\pm$ 2)% respectively. However the class of the QCD events still represents 86% and 80% of the total remaining background of the selected samples at $\sqrt{s}$ = 183 GeV and $\sqrt{s}$ = 189 GeV respectively.
The selection criteria developed were used to select a sample of $q\bar{q}Q\bar{Q}$ events from the data taken at 183 GeV and 189 GeV corresponding to an integrated luminosity of 52.6 pb^{-1} and 154.39 pb^{-1} respectively. A total of 476 candidate $q\bar{q}Q\bar{Q}$ events were selected at $\sqrt{s}$ = 183 GeV and 1326 at

$\sqrt{s}$ = 189 GeV. This is well within expectation of the number of events predicted by the Monte Carlo study for these integrated luminosities.

It was shown in Chapter 1 that the Triple Gauge Boson Couplings determine the total number of expected events as well as the shape of the distribution of the production angle of the W^-. It was therefore decided to apply an Extended Maximum Likelihood (EML) fit to the data which depends on these two experimental informations in order to measure the TGC parameters. We performed one dimensional TGC parameter fits, allowing one parameter to vary while the other two were held at their Standard Model values.
The kinematic information entering in the TGC fit is the production angle of the W^- boson. The difficulty is to measure the direction of the W^- in four jet events, as we do not have a clean charge signature nor do we know which reconstructed jets belong to which W boson. On the basis of the χ^2 of a 6C kinematic fit, imposing on top of energy-momentum conservation the equality of the two reconstructed invariant jet-jet masses with a reference mass for the W boson, we selected the best jet pair combination. In (72.8 $\pm$ 0.3)% (183 GeV) and (74.0 $\pm$ 0.2)% (189 GeV) of the cases we could retrieve the correct combination, as demonstrated with a Monte Carlo study in Chapter 4. A probability P^- as a function of the charge difference ΔQ between the two W objects was constructed to take the charge ambiguity into account. The charge of the W object was calculated from jet charges, measured with a dedicated algorithm. The efficiency for correct W charge assignment was computed to be $\epsilon = (76.0 \pm 0.5)\%$ and $\epsilon = (77.0 \pm 0.3)\%$ for correctly paired hadronic W^+W^- events at centre-of-mass energies of 183 GeV and 189 GeV respectively. In the TGC parameter fit both charge solutions were considered with corresponding weights, as we did not ascribe a definite charge to each di-jet with a ΔQ cut dependent efficiency for the final analysis.
In the EML formula we used the Bilenky theoretical model to compute the shape of the W^- production angle distribution. Only the correctly paired WW events have this TGC dependent shape, while the badly paired events are uniformly distributed in the production angle $\cos\theta_{W^-}$. For the latter sample the only dependence on the TGC parameters α is found in the total production cross section. The number of expected WW events entering in the EML formula depends quadratically on the parameter α. This dependence was obtained from the `Excalibur` generator. The shape of the $\cos\theta_{W^-}$ distribution and total number of background events were estimated from events simulated with the `Pythia` Monte Carlo program. The expression for the EML formula can be found in Chapter 4. The analysis also accounts for the effects of Initial State Radiation on the angular distribution. In this chapter the fitting technique was tested thoroughly and was checked for bias, consistency and efficiency. For all TGC parameters, but $\alpha_{B\phi}$ at $\sqrt{s}$ =183 GeV, the EML method provided an efficient, unbiased and consistent estimator. It was found that the TGC parameters Δg_Z^1 and $\alpha_{W\phi}$ were most accurately measured while less stringent limits for $\alpha_{B\phi}$ were obtained.

Separate fits were performed for each TGC parameter on each of the $q\bar{q}Q\bar{Q}$ data sets obtained at $\sqrt{s}$ = 183 GeV and $\sqrt{s}$ = 189 GeV. The results are given in Chapter 5 where also a full study of possible systematic error contributions is given. The latter are small, but not negligible, in comparison with the quoted statistical errors. The systematic uncertainty on $\alpha_{W\phi}$ is comparable to the statistical uncertainty on this parameter. Important contributions come from uncertainties on signal and background cross-sections and uncertainties in the fragmentation models and uncertainties coming from detector effects. After including the systematic errors in the likelihood functions the results of both data sets were combined by adding the likelihood curves. The analysis at $\sqrt{s}$ = 189 GeV has smaller statistical errors as it contains about three times more data, therefore it also has a greater weight in the combination of the two analyses. The combined results for the four TGC parameters of the fit to the two data sets taken at 183 and 189 GeV are:

$$
\begin{aligned}
\Delta g_Z^1 &= -0.077^{+.176}_{-.141}, \\
\alpha_{W\phi} &= -0.042^{+.129}_{-.107}, \\
\alpha_W \equiv \lambda_\gamma &= -0.073^{+.214}_{-.156}, \\
\alpha_{B\phi} \equiv \Delta\kappa_\gamma &= -0.029^{+.713}_{-.368}.
\end{aligned}
$$

where the one standard deviation errors include all systematic errors. The result quoted for $\alpha_{B\phi}$ only includes the result obtained for the analysis at $\sqrt{s}$ = 189 GeV. All results are in good agreement with the predictions of the Standard Model. It has been shown that despite all the difficulties related to the fully hadronic channel, this channel gives a significant improvement to the precision with which the TGC parameters are determined at LEP.

CONCLUSIONS

Bibliography

[1] P. Renton. Electroweak interactions: An introduction to the physics of quark and leptons. C.U.P, 1990.

[2] F. Halzen and A.D. Martin. Quarks & Leptons. John Wiley & Sons, 1984.

[3] I.J. R. Aitchison and A.J.G. Hey. Gauge theories in particle physics. Adam Hilger, Bristol and Philadelphia, 1989.

[4] F. Mandl and G. Shaw. Quantum Field Theory. J. Wiley & Sons, 1984.

[5] S. L. Glashow. Partial-Symmetries of Weak Interactions, *Nucl. Phys.*, 22B:579, 1961;
A. Salam & J.C. Ward. Electromagnetic and Weak Interaction, *Phys. Lett.*, 13:168, 1964;
S. Weinberg. A model of Leptons, *Phys. Rev. Lett.*, 19:1264, 1967.

[6] S. L. Glashow. Towards a unified theory: Threads in a tapestry. *Rev. Mod. Phys.*, 52:539, 1980.

[7] A. Salam. Gauge unification of fundamental forces. *Rev. Mod. Phys.*, 52:525, 1980.

[8] S. Weinberg. Conceptual foundations of the unified theory of weak and electromagnetic interactions. *Rev. Mod. Phys.*, 52:515, 1980.

[9] F.J. Hasert. Search for elastic muon neutrino scattering. *Phys. Lett.*, B46:121, 1973;
F.J. Hasert. Observation of neutrino like interactions without muons or electrons in the Gargamelle neutrino experiment. *Phys. Lett.*, B46: 138, 1973.

[10] G. 't Hooft. Renormalization of Massless Yang-Mills Fields. *Nucl. Phys.*, B33:173, 1971.

[11] G. 't Hooft. Renormalizable Lagrangians for Massive Yang-Mills Fields. *Nucl. Phys.*, B35:167, 1971.

[12] G. 't Hooft and M. Veltman. Regularization and renormalization of gauge fields. *Nucl. Phys.*, B44:189–213, 1972.

[13] P. Aarnio et al. Measurement of the mass and width of the Z^0 particle from multi-hadronic final states produced in e^+e^- annihilations. *Phys. Lett.*, B231(4):539, 1989.

[14] F. Abe et al. Observation of top quark production in anti-p p collisions. *Phys. Rev. Lett.*, 74:2626–2631, 1995.

[15] S. Abachi et al. Observation of the top quark. *Phys. Rev. Lett.*, 74:2632–2637, 1995.

[16] The LEP collaborations: ALEPH, DELPHI, L3, OPAL and the LEP Electroweak Working Group. A combination of Preliminary LEP Electroweak Measurements and Constraints on the Standard Model, 1995. CERN-PPE/95-172.

[17] G. Arnison et al. Experimental observation of isolated large transverse energy electrons with associated missing energy at $\sqrt{s}$ = 540 GeV. *Phys. Lett.*, B122:103, 1983.

[18] G. Arnison et al. Experimental observations of lepton pairs of invariant mass around 95 GeV/c^2 at the CERN SPS collider. *Phys. Lett.*, B126:398, 1983.

[19] M. Banner et al. Observation of single isolated electrons of high transverse momentum in events with missing transverse energy at the CERN $p\bar{p}$ collider. *Phys. Lett.*, B122:476, 1983.

[20] P. Bagnaia et al. Evidence for $Z^0 \rightarrow e^+ e^-$ at the CERN $p\bar{p}$ collider. *Phys. Lett.*, B129:130, 1983.

[21] The LEP Electroweak Working Group, the SLD Heavy Flavour, and Electroweak Groups. A combination of Preliminary Electroweak Measurements and Constraints on the Standard Model, 2000. CERN-EP/2000-016.

[22] P. W. Higgs. *Phys. Lett.*, 12:132, 1964.

[23] R. Brout & F. Englert. *Phys. Rev. Lett.*, 13:321, 1964.

[24] P. W. Higgs. Broken symmetries and the masses of gauge bosons. *Phys. Rev. Lett.*, 13:508, 1964.

[25] P. W. Higgs. Spontaneous symmetry breakdown without massless bosons. *Phys. Rev.*, 145:1156, 1966.

[26] M. Veltman. Reflections on the Higgs system, 1997. CERN 97-05.

[27] H. Yukawa. On the interaction of elementary particles. *Proc. Phys. Math. Soc. Japan*, 17:48–57, 1935.

[28] E. Fermi. An attempt of a theory of beta radiation. *Z. Phys.*, 88:161–177, 1934.

[29] T. Affolder et al. Measurement of the W boson mass with the Collider Detector at Fermilab. *Subm to Phys. Rev. D*, 2000. hep-ex/0007044.

[30] T. Affolder. Direct measurement of the W boson width in $\mathrm{p\bar{p}}$ collisions at $\sqrt{s}$ = 1.8 TeV. *Phys. Rev. Lett.*, 85:3347, 2000. hep-ex/0004017.

[31] F. Abe et al. Evidence of W^+W^- production in $p\bar{p}$ collisions at $\sqrt{s}$ = 1.8 TeV. *Phys. Rev. Lett.*, 78:4547, 1997.

[32] B. Abbott et al. A measurement of the W boson mass using electrons at large rapidities. *Phys. Rev. Lett.*, 84:222, 2000. hep-ex/9909030.

[33] B. Abbott et al. *Phys. Rev.*, D61:072001, 2000. hep-ex/9906025.

[34] B. Abbott et al. Limits on anomalous $WW\gamma$ and WWZ Couplings from $WW/WZ \rightarrow$ eνjj production. *Phys. Rev.*, D62, 2000. hep-ph/9912033.

[35] R. Barate et al. *Measurement of the W pair production and W branching ratios in e^+e^- collisions at $\sqrt{s}$ = 192 - 202 GeV*, 2000. ALEPH 2000-005 CONF 002.

[36] R. Barate et al. Measurement of Trilinear Gauge Boson Couplings at 192 - 202 GeV, 2000. ALEPH 2000-055 CONF 037.

[37] R. Barate et al. Measurement of the W mass and width in e^+ e^- collisions at $\sqrt{s}$ = 192 - 202 GeV, 2000. ALEPH 2000-018 CONF 015.

[38] P. Bushmann et al. Measurement of the W pair production cross-section and W branching ratios at $\sqrt{s}$ = 192 - 202 GeV, 2000. DELPHI 2000-140 CONF 439.

[39] T.J.V. Bowcock et al. Measurement of Trilinear Gauge Boson Couplings in e^+ e^- collisions at 192 - 202 GeV, 2000. DELPHI 2000-146 CONF 445.

[40] D. Bloch et al. Measurement of the mass and width of the W boson in e^+e^- Collisions at $\sqrt{s}$ = 192 - 202 GeV, 2000. DELPHI 2000-149 CONF 446.

[41] M. Acciari et al. Preliminary results on the measurement of the W pair cross-section and W decay branching fractions in e^+ e^- collisions at $\sqrt{s}$ = 192 - 202 GeV, 2000. L3 NOTE 2514.

[42] M. Acciari et al. Preliminary results on the measurement of Triple Gauge Boson Couplings of the W boson in e^+ e^- collisions at $\sqrt{s}$ = 192 - 202 GeV, 2000. L3 NOTE 2567.

[43] M. Acciari et al. Preliminary results on the measurement of the mass and width of the W boson in e^+ e^- collisions at $\sqrt{s}$ up to 202 GeV, 2000. L3 NOTE 2575.

[44] G. Abbiendi et al. Measurement of the Standard Model Processes in e^+e^- Collisions at $\sqrt{s} > 190$ GeV, 2000. OPAL PHYS NOTE PN 420.

[45] G. Abbiendi et al. Triple Gauge Boson Couplings in W^+W^- production at LEP energies up to 202 GeV, 2000. OPAL PHYS NOTE PN 441.

[46] G. Abbiendi et al. Measurement of the mass of the W boson in e^+e^- annihilations at 192 - 202 GeV, 2000. OPAL PHYS NOTE PN 422.

[47] W.J. Stirling and A. Werthenbach. Anomalous quartic couplings in $\nu\bar{\nu}\gamma\gamma$ production via WW fusion at LEP2. *Phys. Lett.*, B466:369, 1999. hep-ph/9907235;
W.J. Stirling and A. Werthenbach. Anomalous quartic couplings in $W^+W^-\gamma\gamma$, $ZZ\gamma$ and $Z\gamma\gamma$. *Eur. Phys. J.*, C14:103, 2000. hep-ph/9903315.

[48] G. Gounaris J.-L. Kneur and D. Zeppenfeld. Triple Gauge Boson Couplings. *Physics at LEP2*, page 525, 1996. CERN 96-02.

[49] A. De Rújula, M. B. Gavela, O. Pene, and F. J. Vegas. Signets of CP violation. *Nucl. Phys.*, B357:311–356, 1991.

[50] A. De Rújula, M. B. Gavela, P. Hernandez, and E. Masso. The selfcouplings of vector bosons: Does LEP-1 obviate LEP-2? *Nucl. Phys.*, B384:3–58, 1992.

[51] M. Bilenky, J. L. Kneur, F. M. Renard, and D. Schildknecht. Trilinear couplings among the electroweak vector bosons and their determination at LEP200. *Nucl. Phys.*, B409:22, 1993.

[52] R.L. Sekulin. Ambiguities in the determination of the vector boson couplings at LEP200. *Phys. Lett.*, B338:369, 1994.

[53] G. Gounaris, J. Layssac, G. Moultaka, and F. M. Renard. Analytic expressions of cross-sections, asymmetries and W density matrices for $e^+ e^- \to W^+W^-$ with general three boson couplings. *Int. J. Mod. Phys.*, A8:3285–3320, 1993.

[54] J. Ellis. Beyond the Standard Model for Hillwalkers, 1998. hep-ph/9812235.

[55] J. M. Frère, J. M. Moreno, M. Tytgat, and J. Orloff. LEP-1 vs. future colliders: Effective operators and extended gauge group. *Phys. Lett.*, B292:348–352, 1992.

[56] J. M. Frère, M. Tytgat, J. M. Moreno, and J. Orloff. Effective operators and extended symmetry. *Nucl. Phys.*, B429:3–18, 1994.

[57] A.B. Lahanas and V.C. Spanos. Static quantities of the W boson in the MSSM. *Phys. Lett.,* B334:378, 1994;
E.N. Argyres, A.B. Lahanas, C. G. Papadopoulos and V.C. Spanos. Trilinear Gauge Boson Coupling in the MSSM. *Phys. Lett.,* B383:64, 1996;
A. Arhrib, J.-L. Kneur and G. Moultaka. MSSM radiative contributions to the $WW\gamma$ and WWZ form factors. *Phys. Lett.,* B376:127, 1996.

[58] K. Hagiwara, R. D. Peccei, D. Zeppenfeld, and K. Hikasa. Probing the weak boson sector in $e^+ e^- \to W^+W^-$. *Nucl. Phys.*, B282:253, 1987.

[59] R.M. Barnett et al. Review of particle physics. *Phys. Rev.*, D54:172, 1996.

[60] M. Bilenky, J. L. Kneur, F. M. Renard, and D. Schildknecht. The potential of a new linear collider for the measurement of the trilinear couplings among the electroweak vector bosons. *Nucl. Phys.*, B419:240–253, 1994.

[61] T. Muta, R. Najima, and S. Wakaizumi. Effects of the W boson width in $e^+e^- \to W^+W^-$ reactions. *Mod. Phys. Lett.*, A1:203, 1986.

[62] R. Kleiss F.A. Berends and R. Pittau. All electroweak four-fermion processes in electron-positron collisions. *Nucl. Phys.*, B424:308–342, 1994.

[63] C.J. Parkes P.B. Renton and H.T. Phillips. A study of four-fermion final state interference relevant to the measurement of the W^+W^- cross-section and the W mass, 1997. DELPHI 97-96 PHYS 718.

[64] *Nucl. Phys.* (Proc. Suppl.), B37:163, 1994;
R. Pittau, *Phys. Lett.*, B335:490, 1994;
F.A. Berends, R. Pittau and R. Kleiss, `Excalibur`, *Comp. Phys. Comm.*, 85:437, 1995.

[65] H.T. Phillips. `Exff`: The DELPHI-customised version of `Excalibur` (UPDATE), 1997.

[66] S. Jadach et al. *Phys. Lett.*, B417:326, 1998.

[67] W. Beenakker and F.A. Berends. WW cross-sections and distributions. *Physics at LEP2*, Volume 1:79, 1996. CERN 96-01.

[68] W. Beenakker and A. Denner. Standard model predictions for W pair production in electron - positron collisions. *Int. J. Mod. Phys.*, A9:4837–4920, 1994.

[69] R. Kleiss F.A. Berends and R. Pittau. Initial state QED corrections to four-fermion production in e^+e^- collisions at LEP200 and beyond. *Nucl. Phys.*, B426:344, 1994.

[70] Y. Kurihara et al., 1995. KEK CP-035, KEK 95-126.

[71] Z. Kunst and W.J. Stirling. Determination of the mass of the W boson. *Physics at LEP2*, Vol. 1:141, 1996. CERN 96-01.

[72] B.R. Webber. Colour Reconnection and Bose Einstein effects. *J. Phys.*, G24:287–296, 1998.

[73] T. Sjöstrand and V.A. Khoze, *Zeit. Phys.,* C62:281, 1994;
Phys. Rev. Lett., 72:28, 1994.

[74] P. Abreu et al. Bose Einstein Correlations in the hadronic decays of the Z. *Phys. Lett.*, B281:383, 1992.

[75] P. Abreu et al. Correlations between particles from different W's in $e^+e^- \to W^+W^-$ events. 1999. DELPHI 99-159 CONF 330.

[76] L. Lönblad and T. Sjöstrand. Modelling Bose Einstein Correlations at LEP2. *Eur. Phys. J.*, C2:165, 1998. hep-ph/9711460.

[77] P. Aarnio et al. The DELPHI detector at LEP. *Nucl. Instr. Meth.*, A303:233–276, 1991.

[78] P. Abreu et al. Performance of the DELPHI detector. *Nucl. Instr. Meth.*, A378:57–100, 1996.

[79] *LEP design report: Vol. 1., The LEP injector chain*, 1983. CERN-LEP/TH/83-29.

[80] *LEP design report: Vol. 2., The LEP main ring*, 1984. CERN-LEP/84-01.

[81] *LEP design report: Vol. 3., LEP 2*, 1996. CERN-AC/96-01.

[82] S. Meyers. The LEP collider, from Design to Approval and Commissioning, 1991. CERN/91-08.

[83] DELPHI collaboration. DELPHI Data Analysis Program `Delana`, User's guide, 1989. DELPHI 89-46 PROG 137.

[84] P. Chochula et al. The DELPHI silicon strip microvertex detector with double sided readout. *Nucl. Instr. Meth.*, A412:304, 1998.

[85] E. Barrelet. Optical fibre calorimetry. In C. Vander Velde J. Lemonne and F. Verbeure, editors, *Proceeding of the International Europhysics Conference on High Energy Physics*, 1995.

[86] S.J. Alvsvaag et al. Performance of the new high precision luminosity monitor of DELPHI at LEP, 1995. DELPHI 95-68/PHYS 503.

[87] T.J. Adye et al. *Nucl. Instr. Meth.*, A349:160, 1994.

[88] R. Brun and J. Zoll. `Zebra`: Data structure management system. CERN Program Library Long Writeups Q100.

[89] V. Perevozchikov and N. Smirnov. `Phdst` Package Description V.3 VZD - Viewer of `Zebra` Data for DELPHI , User's Manual, 1992. DELPHI 92-118 PROG 189.

[90] Tz. Spassof and N. Smirnov. `Skelana` - Skeleton Analysis Program, 1995.

[91] DELPHI Coll. `Delsim`, DELPHI event generator and detector simulation - Reference Manual, 1989. DELPHI 89-68 PROG 143.

[92] P. Abreu et al. W pair production cross-section and W branching fractions in e^+e^- interactions at 183 GeV. *Phys. Lett.*, B456:310–321, 1999.

[93] T. Sjöstrand. `Pythia` 5.7 and `Jetset` 7.4 Physics and Manual, 1993. CERN-TH 7112.

[94] B. Söderberg B. Andersson, G. Gustafson. A general model for jet fragmentation. *Z. Phys.*, C20:317–329, 1983.

[95] D. Bardin et al. `Zfitter`: An Analytical Program for Fermion Pair Production in e^+e^- Annihilation, 1999. hep-ph/9908433.

[96] J. Wickens. Detector status flags in `Delana`, 1995. DELPHI 95-38 PROG 213.

[97] P. Abreu et al. W pair production cross-section and W braching fractions in e^+e^- interactions at 189 GeV. *Phys. Lett.*, B479:89, 2000. CERN-EP-035.

[98] The LEP Energy Working Group. A. Blondel et al. Evaluation of the LEP centre-of-mass energy above the W pair production threshold. *Eur. Phys. J.*, C11 (4):573–585, 1999. CERN-EP/98-191.

[99] LEP Energy Working Group. Evaluation of the LEP centre-of-mass energy for data taken in 1998, 1999. LEP Energy Group 99-01.

[100] S. Moretti, L. Lönblad, and T. Sjöstrand. New and old Jet Clustering Algorithms for Electron-Positron Events, 1998. hep-ph/9804296.

[101] S. Catani et al. New clustering algorithm for multijet cross-sections in e^+e^- annihilation. *Phys. Lett.*, B269:432–438, 1991.

[102] N. Brown and W.J. Stirling. Finding jets and summing soft gluons: a new algorithm. *Z. Phys.*, C53:629–636, 1992.

[103] N.J. Kjær and R. Møller. Reconstruction of invariant masses in multi-jet events, 1991. DELPHI 91-17 PHYS 88.

[104] P. Abreu et al. Measurement of the W pair cross-section and of the W mass in e^+e^- interactions at 172 GeV. *Eur. Phys. J.*, C2:581–595, 1998.

[105] P. Abreu et al. *Nucl. Instr. Meth.*, A427:487, 1999.

[106] L. Lyons. Statistics for nuclear and particle physicists. C.U.P, 1986.

[107] R. Barlow. Statistics; A guide of the use of statistical methods in physical sciences. J. Wiley & Sons Ltd., 1989.

[108] A.G. Frodesen O. Skeggestad and H. Tøfte. Probability and statistics in particle physics. Universitetsforlaget Bergen-Olso-Tromsø.

[109] W.T. Eadie et al. Statistical Methods in experimental physics. Elsevier, 1971.

[110] G. D'Agostini. Bayesian Reasoning in High Energy Physics - Principles and Apllications-. 1998.

[111] F. James. `Minuit`, Reference Manual - Version 92.1. March 1992.

[112] F. Terranova. Non linearities in TGC estimators that use the total event rate, 1999. DELPHI 99-48 PHYS 822.

[113] U. Parzefal. A measurement of Trilinear Gauge Couplings using the DELPHI detector. PhD thesis, University of Liverpool, 1999.

[114] P. Abreu et al. Measurement of the trilinear Gauge Boson Couplings WWV ($V \equiv \gamma$,Z) in e^+ e^- collisions at 183 GeV. *Phys. Lett.*, B459:382, 1999.

[115] D. Bloch et al. Measurement of the mass and width of the W boson in e^+ e^- collisions at $\sqrt{s}$ = 189 GeV, 2000. DELPHI 2000-144 CONF 443.

[116] M. Mulders, *Private Communication*.

[117] S. Jadach et al. Monte Carlo program `koralw` 1.42 for all four-fermion final states in e^+e^- collisions. *Comp. Phys. Comm.*, 119:272, 1999.

[118] G. Abbiendi et al. *Comp. Phys. Comm.*, 67:465, 1992.

[119] T.J.V. Bowcock et al. Measurement of Trilinear Gauge Boson Couplings WWV ($V \equiv \gamma$,Z) in e^+ e^- collisions at 189 GeV, 2000. DELPHI 2000-139 CONF 438.

[120] M. Diehl and O. Nachtman, *Z. Phys.,* C62:397, 1994;
G.K. Fanourakis, D. Fassouliotis and S.E. Tzamarias, *Nucl. Inst. Meth.,* A414:399, 1998;
G.K. Fanourakis et al., *Nucl. Inst. Meth.,* A430:474, 1999.

[121] R. Barate et al. Measurement of Trilinear Gauge Boson Couplings at LEP energies up to 189 GeV, 2000. ALEPH 2000-015 CONF 012.

[122] M. Acciari et al. Preliminary results on the measurement of Triple Gauge Boson Couplings of the W boson in e^+ e^- collisions at LEP, 1999. L3 NOTE 2378.

[123] G. Abbiendi et al. Measurement of Triple Gauge Boson Couplings from W^+W^- production at LEP energies up to 189 GeV. *Subm to Eur. Phys. J.*, C, 2000. CERN-EP/2000-114.

[124] http://lepewwg.web.cern.ch/LEPEWWG/tgc.

[125] J. Ellison and J. Wudka. Study of Trilinear Gauge Boson Couplings at the Tevatron Collider. *Ann. Rev. Nucl. Part. Sci.*, 48:33, 1998. hep-ph/9804322.

[126] S. Abachi et al. Limits on anomalous $WW\gamma$ couplings from $p\bar{p}$ →W$\gamma + X$ events at $\sqrt{s}$ = 1.8 TeV. *Phys. Rev. Lett.*, 78:3634, 1997.

[127] F. Abe et al. Measurement of $W - \gamma$ couplings in $p\bar{p}$ collisions at $\sqrt{s}$ = 1.8 TeV. *Phys. Rev. Lett.*, 74:1936, 1995.

[128] B. Abbott et al. Study of WW and WZ production and limits on anomalous $WW\gamma$ and WWZ couplings. *Phys. Rev.*, D60:072002, 1999.

[129] U. Baur and D. Zeppenfeld. Measuring the $WW\gamma$ vertex in single W production at ep colliders. *Nucl. Phys.*, B325:253, 1989.

[130] J. Breitweg et al. W production and the search for events with an isolated high-energy lepton and missing transverse momentum at HERA. *Phys. Lett.*, B471:411, 2000.

[131] A.V. Kotwal, *presentation at ICHEP2000*, 27 July-3 August 2000, Osaka, Japan.

[132] G. Azuelos et al. Electroweak physics. In *Proceedings of the workshop on Standard Model Physics (and more) at the LHC*, page 169, 2000. CERN 2000-004.

[133] E. Accomando et al. Particle physics. In *Proceedings of the Conceptual Design of a 500 GeV e^+e^- Linear Collider with integrated X-ray Laser Facility*, page 1, 1997. ECFA 1997-182.

Dankwoord

Deze pagina is het einde van een lange maar leerrijke reis, die gepaard ging met de nodige bergen en dalen. Het aangename van deze reis was dat ik een boel interessante en leuke mensen tegenkwam, en sommigen beter leerde kennen, die allen op hun manier een steentje aan dit werk bijgedragen hebben. Dit maakte dat de reisweg voor mij een stuk prettiger verliep. Het is echter onmogelijk iedereen hier te vermelden, daarom wil ik me alvast verontschuldigen bij degenen die ik mocht "vergeten" zijn.
Het vuur voor hoge energie fysika werd ontstoken door de colleges van Prof. Dr. J. Lemonne en laaide helemaal op tijdens de CERN studiereis en mijn zomerstudent stage te CERN in 1995. Mijn hartelijke dank gaat dan ook uit naar Prof. Dr. J. Lemonne om me een doctoraatsplaats op het DELPHI experiment aan te bieden op zijn dienst in de herfst van 1995. Tevens wil ik hem danken voor de vele discusies en kritieken die dit werk ten stelligst hebben verbeterd en het mogelijk maken van de nuttige verblijven op CERN.
Niet minder belangrijk was de steun en hulp die ik kreeg van mijn promotor Dr. C. De Clercq. Haar deur stond altijd open om de eindeloos lijkende lijst van vragen op te vangen. Cathérine, heel erg bedankt voor de prettige samenwerking.
I would like to thank all the members of the thesis examination committee for their participation. Particular thanks are due to Dr. Robert Sekulin for a very useful introduction to the subject of trilinear couplings and for the many discussions we have had over the past five years. Mijn meer dan oprechte dank gaat eveneens uit naar Dr. Jan Timmermans voor de zeer nuttige op- en aanmerkingen die dit manuscript ten goede zijn gekomen en voor de waardevolle discussies die telkens zeer leerrijk waren. Par la présente, je tiens également à remercier le Prof. Dr. Jean-Marie Frère pour m'expliquer patiemment les petits et grands secrets de la théorie des couplages trilinéaires et de la physique théorique en général. Tevens dank aan Prof. Dr. Stefaan Tavernier voor de vele discussies omtrent de bijstelling.
I would also like to thank Dr. Duncan Reid for the useful remarks he provided on some physics and English grammar issues and for the many tips and trics in Latex. Thanks to all who have enlighted my many stays at CERN.
Op CERN raakte ik helemaal ingeburgerd in de Nederlandse kliek. Daniel, Ivo, Martijn, Tasja en Frank, Simon, Rutger, Henric, Bert en Tanja, Michiel, Koen: ik genoot van de vele film bezoeken, het lekkere eten, de leuke feestjes, raften, bergwandelen, de goeie gesprekken,.... en jullie "rare accent"! Sandra ook heel erg bedankt voor de steun, de roddelthee en de gezellige tijd die we hadden in ons heksenhuis.
Ook collega's op het IIHE waren belangrijk: An, Annie, Barbara, Bob, Chantal, Francesca, Jacqueline, Jorgen, Pascal, Peter, Redouane, Roel, Rosine, Wim, Yves,... dank je wel!
Maar ook het thuisfront liet zich niet onbetuigd in de steun. Bijzondere dank aan Jo die me uit een computer crisis redde, zonder jou was er bijna geen proefschrift geweest! Maar ook Katja (voor de vele "jatjes" koffie en babbeltjes), Marleen, Evert en Wim hartelijk dank om er telkens weer te zijn als ik weer eens opdook.
Als laatsten maar zeker niet het minst belangrijk wil ik mijn ouders, Sara en André bedanken. Zonder jullie continue steun, motivatie en gekke invallen was dit allemaal niet mogelijk geweest.